HYBRID INDUCTION HEATING AND LINEAR FRICTION WELDING

A Dissertation

Submitted to the Graduate School

of the University of Notre Dame

in Partial Fulfillment of the Requirements

for the Degree of

Doctor of Philosophy

by

Matthew R. Kelly

Steven R. Schmid, Director

Graduate Program in Aerospace and Mechanical Engineering

Notre Dame, Indiana

April 2019

HYBRID INDUCTION HEATING AND LINEAR FRICTION WELDING

Abstract

by

Matthew R. Kelly

Linear Friction Welding (LFW) is a robust joining process with many potential applications, the most successful being the attachment of turbine blades to disks. Given the large scale of such operations, and the large amount of energy that must be stored, the equipment is prohibitively expensive for most industries. Heating the workpieces prior to LFW may reduce energy requirements and therefore allow for cost savings on the equipment, but the ancillary effect on weld quality is unknown. A design of experiments (DOE) approach is used to study the effect of four process parameters (average rubbing velocity, weld pressure, upset distance, and preheat temperature) on three response variables (weld strength, heat affected zone (HAZ) width/peak hardness, and energy usage) for the Induction Heating (IH) and Linear Friction Welding (LFW) of AISI 1020 steel. Numerical models for both IH and LFW were developed in DEFORM to replace the need for costly LFW experimentation with less expensive modeling.

Weld strength and HAZ were insensitive to all four of the process parameters. Energy usage was most significantly affected by pressure, followed by velocity and upset. Pressure had an inverse effect on energy used, whereas velocity and upset had linear effects. Preheating the workpieces prior to LFW showed no adverse effects on weld quality, and therefore represents a viable strategy to reduce the cost of LFW equipment in the future.

A novel method for approximating the IH process with an IH coil in two dimensions (2D) generated close approximations of temperature growth with time. The results from the IH numerical model were passed to the LFW numerical model, which incorporated a novel user subroutine for calculating friction factors that account for asperity flattening and real contact area growth. Contact loss issues in DEFORM while modeling the initial phase of LFW thermo-mechanically led to the conclusion that the initial phase of LFW must be modeled purely thermally, before the latter phases are modeled thermo-mechanically.

DEDICATION

In gratitude to my family.

To Kimberly Renee Kelly, my wife, best friend, and source of motivation, whose unending support sustained me through graduate school. Nothing brings me more joy than coming home to you and Nyx after a long day of work. I cannot wait to navigate life with you by my side.

To Robert J. Kelly and Susan O. Kelly, who raised me in the Notre Dame tradition, and are responsible for my education. Your commitment to God, family, and friends is a shining example of how to be children, parents, and companions in life.

To Erin P. Kelly and Daniel J. Kelly, whose dedication to hard work inspires me to do the same. I could not have asked to grow up alongside better siblings.

Words cannot express how much I love you all.

CONTENTS

FIGURES

TABLES

NOTATION AND ACRONYMS

FRW	friction welding
RFW	rotational friction welding
LFW	linear friction welding
HAZ	heat affected zone
FEA	finite element analysis
FEM	finite element method
HAB	hydraulic accumulator bank
IH	induction heating
MTI	Manufacturing Technologies, Inc.
SFTC	Scientific Forming Technologies Corporation
2D	two dimensional
3D	three dimensional
DOE	design of experiments
DAQ	data acquisition
BEM	boundary element method
BC	boundary condition
MUMPS	multifrontal massively parallel sparse direct solver
PSE	pseudo standard error
VHN	Vickers hardness number
OM	optical microscopy
SEM	scanning electron microscopy
TMAZ	thermo-mechanically affected zone

DRX	dynamic recrystallization
J	current density
μ	magnetic permeability, also coefficient of friction
t	time, also thickness
ω	angular frequency
J_s	surface current density
δ	penetration depth
ρ	electrical resistivity, also material density
ρ_m	material density
C_p	specific heat
k	thermal conductivity
T	temperature
$\dot{q}$	heat generation due to plastic deformation
P	surface power density, also indentation force, and power
α	thermal diffusivity
P_{model}	model power
$P_{\text{experiment}}$	experimental power
SA_{model}	model surface area
$SA_{\text{experiment}}$	experimental surface area
HI	heat input
f	oscillation frequency
a	oscillation amplitude
F_f	friction force
E	energy
u	instantaneous velocity
v	average rubbing velocity
$\dot{Q}$	energy input rate

N normal force

A weld cross sectional area, also fractional contact area

m friction factor

τ shear stress

τ_0 shear yield stress

$\dot{S}$ heat generation due to plastic deformation

α thermal efficiency of plastic deformation

$\bar{\sigma}$ effective stress

$\dot{\bar{\epsilon}}$ effective strain rate

f_s friction stress

p interface pressure

θ initial asperity slope

f_1 function

f_1 function

m_{avg} average friction factor

m_a asperity friction factor

m_o oxide friction factor

r radius

C span between supports of a three point bend test

w width

D deflection

d_v mean diagonal of impression

F_t total force

F_I inertial force

ACKNOWLEDGMENTS

First, I would like to recognize and thank my advisor, Dr. Steven R. Schmid for providing me the opportunity to conduct manufacturing research in his lab. His unique teaching style for his undergraduate course on Engineering Analysis of Manufacturing Processes inspired me to pursue a PhD and future career in manufacturing. I would also like to thank my committee members, Dr. Ryan Roeder, Dr. Paul McGinn and Dr. Bill Goodwine for their time and effort, as well as their inspiring dedication to instruction at Our Lady's University.

Also deserving of recognition in this project are Daniel Adams and Jeffrey Fletcher of Manufacturing Technologies Inc. (MTI). Dan was instrumental in formulating the motivation behind this dissertation, and Jeff consistently challenged me and my engineering assumptions. MTI provided the funding for this project, and without them, this work would not have been possible.

Thank you to Chris Fischer of Scientific Forming Technologies, whose expertise in DEFORM assisted in building the friction user routines. Thank you to Kevin Peters for assisting me in repairing a broken tension testing system and a polishing wheel (twice). Thank you to Leon Hluchota who graciously cut microhardness test pieces, and circular molds from tubing. Thank you to Nancy Davis, whose endless support for graduate students at the University is invaluable.

Thank you to my lab members Kirsten Kozlovsky, Jessica Schiltz, and Tyler Jaramillo for listening to my ideas and providing valuable feedback. Thank you to the entire MRB family, who made my time at ND enjoyable and unforgettable. I am proud to have worked alongside such amazing students, faculty, and staff.

CHAPTER 1

INTRODUCTION AND MOTIVATION

1.1 History and Overview of Friction Welding

In welding, the energy required to join materials is supplied from external sources, typically chemical, electrical, or mechanical [29]. In friction welding (FRW), the mechanical energy required for welding is generated through interfacial friction between two components [29]. This solid-state joining technique has many advantages over fusion welding methods such as arc welding, including very small heat-affected zones, short processing times, improved surface chemistry, no solidification defects (porosity, thermal cracking, segregation), improved strength at the interface, and the ability to weld dissimilar materials. FRW can be used to join a wide variety of ductile materials, especially those used in fatigue applications.

1.1.1 Rotary Friction Welding

Developed in the 1940s, rotary friction welding (RFW) is a process where one of the workpieces remains stationary while the other is placed in a chuck or collet and rotated at a constant angular speed, resulting in surface speeds of around 15 m/s (3000 ft/min) [29]. Figure 1.1 depicts the RFW process. First, a stationary part begins rotating at high speed. Second, an axial force is established by the non-rotating part. Third, the axial force is increased and flash begins to form. Finally, the rotating workpiece is brought to a quick stop, the axial force is increased, and as a result, the two workpieces develop a strong welded joint [29]. The upset distance is the distance the two pieces move inward during welding after their initial loaded contact; thus, the total length after welding is less than the sum of the lengths of the two pieces. Oxides and other contaminants at the interface are usually removed by the radial outward movement of the hot interface metal, resulting in flash that subsequently can be removed by machining or grinding [29]. Solid steel bars up to 100 mm (4 in.) in diameter and pipes up to 500 mm (10 in.) in outside diameter have been friction welded successfully [29].

"The weld zone is usually confined to a narrow region, and its size and shape depend on the (a) amount of heat generated, (b) thermal properties of the materials, (c) mechanical properties of the materials being joined at elevated temperatures, (d) relative speed, and (e) axial pressure applied" [29]. RFW is a well-established and valuable manufacturing process for shafts, pipes, and other round (axisymmetric) parts, but it is not suitable for more challenging geometries.

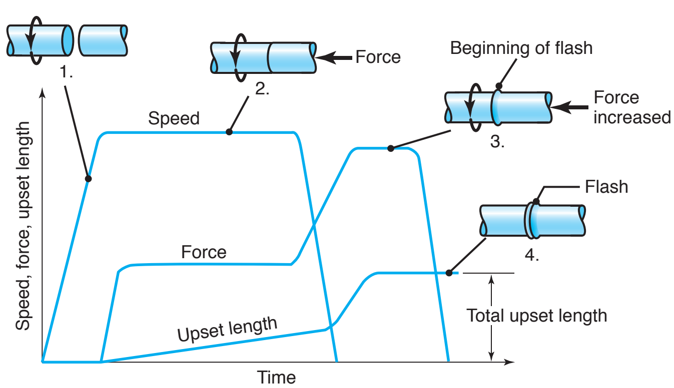

Figure 1.1. Sequence of operations in the RFW process [29].

1.1.2 Linear Friction Welding

First patented in 1929 [56], linear friction welding (LFW) was thought to be unviable as a manufacturing process because of the immense cost, however it became a commercially accepted technique for joining metals in the 1990s for high-value-added applications [76]. Modern LFW development began at The Welding Institute (TWI) in the 1980s due to demand from the aerospace industry to repair severely damaged blades on turbine fans, also known as "blisks" (short for bladed disks) (Fig. 1.2). The economic and mechanical benefits of RFW further contributed to the pursuit of the technology.

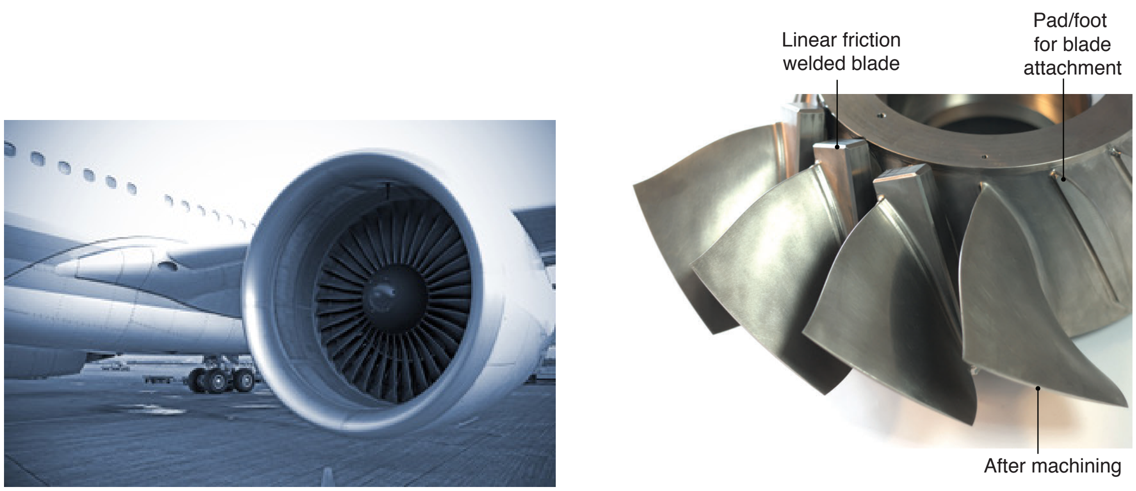

Figure 1.2. (a) Jet engine with an LFW turbine fan blisk [28] (b) Enlarged view of a compressor blisk [28].

As in RFW, LFW takes place in four phases, partially described by Vairis and Frost [73] and Maalekian [42], and subsequently standardized by the American Welding Society [5]:

1. *The contact phase*: The forging workpiece is brought into contact with its counterpart, and the load is increased up to the forge load specified for that weld. At that load the forge position is recorded and set as the reference zero position for calculating upset distance.

2. *The first friction phase*: One part begins to oscillate linearly while pressure is applied at the interface. The friction coefficient increases throughout this phase along with the true contact area (accounting for surface roughness and micro-contact of asperities) between the members due to flattening of asperities on the surface of both parts. First friction ends after a predetermined amount of time or upset, as set by the user of the machine.

3. *The second friction phase*: It is recognized that metal asperities are in plastic contact even under light loads [23], and the superposition of a friction stress causes rapid junction growth and fully saturated contact surfaces. Thus, at this stage of the process, the true contact area is essentially the same as the apparent contact area, even though the metal has not softened due to bulk plastic straining [79]. The plasticized layer between the two parts cannot support the applied load, causing plastic flow of material. The heat affected zone (HAZ, the area of material that undergoes recrystallization) expands into both parts in the direction of the applied load (Fig. 1.3). Axial shortening (upsetting) begins. Material is extruded from the weld interface in the form of flash, until the desired upset distance is achieved. The peak temperature is reached just before the onset of the final phase.

4. *The forge phase*: When the desired upset is reached, the oscillations stop and the forge force is either maintained or increased to consolidate the weld.

FRW has been successfully applied to all metals, but particular interest has been in the joining of aluminum [33], [44], titanium [7], [73], magnesium [54], chromium, nickel, carbon steel [49], stainless and other advanced steels [80], [60], [61], and alloys/combinations of these materials [6], [8], [55], [21]. LFW of these expensive materials is essential for their wider application, but the high cost of the equipment and tooling limits LFW to certain high-value-added applications, primarily, the production of titanium-bladed disks (blisks) in turbine engines [50]. Although LFW is an established process for joining titanium and nickel alloys [20], the cost of equipment prohibits its use for non high-value-added applications with less expensive materials [77]. Existing methods to reduce equipment cost include the use of more efficient power sources and stored energy methods [58], neither of which impact the LFW process. In addition to the reduction in setup costs, considerable time and money are spent fine-tuning weld parameters through trial and error for each new part formed.

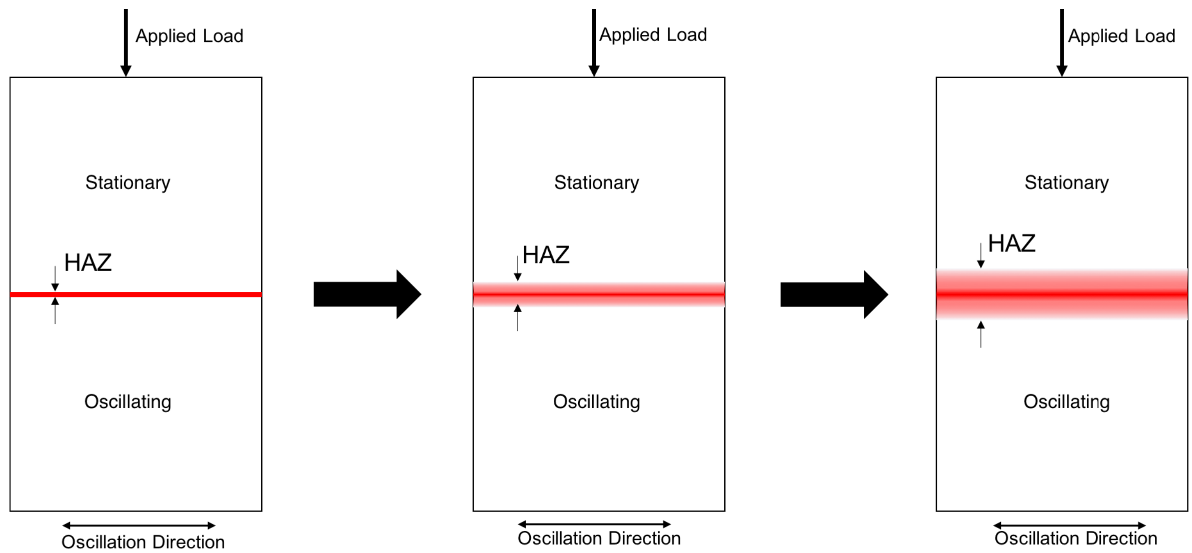

Figure 1.3. HAZ growth during LFW. Frictional energy at the weld surface results in heat generation that expands into both workpieces via conduction. At high enough temperatures, the metal undergoes recrystallization. This recrystallized area is referred to as the HAZ.

1.2 Motivation

The goals of this research are to improve understanding of LFW, incorporate external heating, and reduce motor and energy storage requirements, thereby reducing energy requirements, leading to improved quality and economics for the production of LFW machines. This goal will be accomplished in two ways: first by hybridizing induction heating (IH) and LFW, and second through finite element analysis (FEA) modeling improvements.

1.2.1 Hybridized Induction Heating and Linear Friction Welding

In order to successfully hybridize IH and LFW, the results must be both economically superior and at least functionally equivalent to LFW. In a recent cost analysis of a constructed LFW machine, Manufacturing Technologies Inc. (MTI) determined that almost 60% of the machine cost stemmed from the base frame and isolation (Figs. 1.4, 1.5). Within the base frame, almost 50% of the cost is associated with the main frame assembly, and within the main frame assembly, the accumulator bank accounted for nearly 40% of the cost. It is expected that introducing IH into an LFW machine will reduce the energy required for welding and therefore decrease the size and cost of the hydraulic accumulator bank (HAB) and machine. Furthermore, the substitution of IH in the initial phase of LFW may reduce the cost per weld, depending on energy usage.

1.2.2 IH & LFW Modeling: Finite Element Analysis

Originally coined by Boeing as the Direct Stiffness Method in the 1950s, the Finite Element Method (FEM) gained popularity in the decades to follow because it provided accurate solutions to problems involving structural analysis and heat transfer, without the need for expensive testing. As computing power increased, solution time decreased, and FEM software became a necessary investment for companies looking to eliminate costs associated with experimental, trial and error testing of complex geometries. Today, there are many commercial FEM software packages available. In order to be suitable for IH & LFW, the software should have the following characteristics [73]:

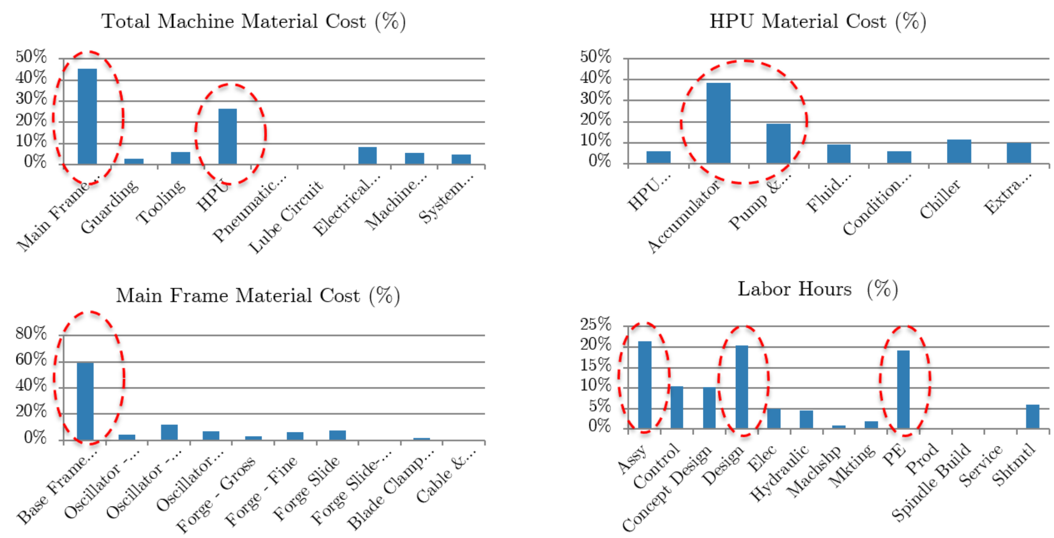

Figure 1.4. Cost Analysis of an MTI 75 ton LFW machine

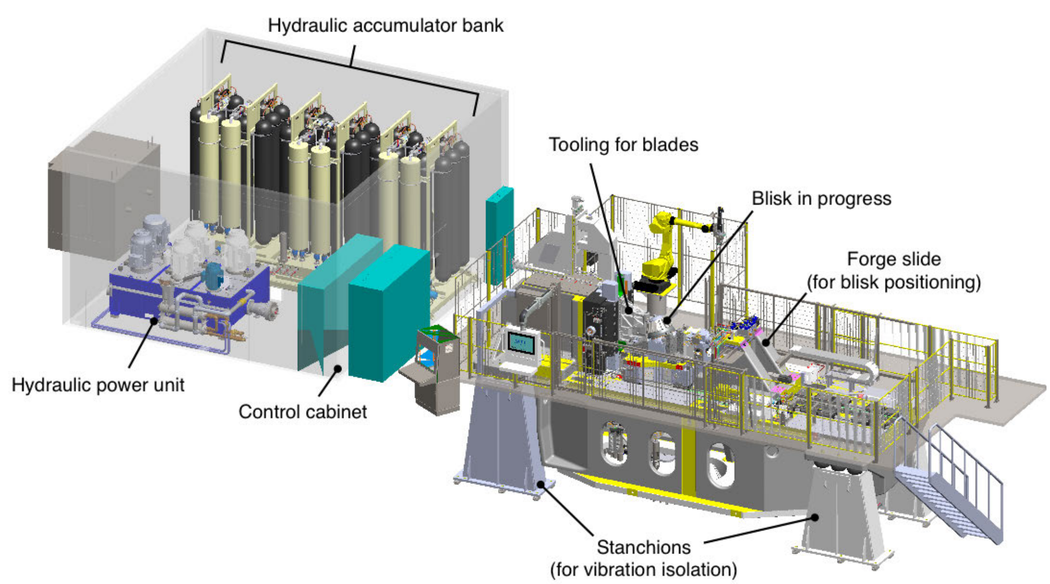

Figure 1.5. Schematic of a 75 ton LFW machine (MTI)

1. *Induction Heating Capability.* The software must have the ability to model induction heating.

2. *Thermal and Mechanical Simulations.* The software must be able to predict, illustrate, animate, and store mechanical stress and temperature over time.

3. *Material non-linearity.* Material properties can affect the accuracy of the prediction. Temperature and strain rate dependent material properties, and validated constitutive laws are essential to obtain an accurate prediction and therefore must be available in the software.

4. *Complex thermal boundary conditions.* The software must contain the ability to model the conduction of heat between surfaces in contact, convection from open surfaces to the surrounding air, radiation losses due to the high temperatures reached, and heat generated by eddy currents through electromagnetic induction.

5. *Complex mechanical boundary conditions.* The software must be able to account for the time-dependent nature of contact area and friction coefficient.

6. *Remeshing.* Due to large deformations in metal forming, elements may stretch to a degree that renders the prediction inaccurate. Remeshing allows the elements to reset when the deformation of an element becomes too large.

7. *User Routines.* In order to incorporate unique methods for calculating the frictional boundary condition between the two workpieces, user routines must be supported.

DEFORM, an FEM software developed by Scientific Forming Technologies Corporation (SFTC) [2], is a powerful simulation system designed to analyze three-dimensional flow of complex metal forming processes. It was created to predict the material flow in industrial forming operations in order to eliminate the cost of shop trials. The simulation engine is capable of predicting large deformation material flow as well as thermal behavior. The software supports user routines and user defined variables. DEFORM has an automatic mesh generator that is efficient and fast. Furthermore, the software contains an automatic remeshing feature, which is very useful in modeling LFW, where the large strains often associated with near melting temperatures can make a mesh unstable. DEFORM has an induction heating module fully capable of modeling coils, air, and workpieces in two dimension (2D) and three dimensions (3D). The software also has multiple deforming body capabilities with multiple contact, and in the case of LFW, sticking conditions. In addition to its suitability for modeling IH & LFW, DEFORM is widely used by research groups on the forefront of LFW modeling [46, 62]. As such, it was chosen as the FEM software for this project.

CHAPTER 2

IH AND LFW EXPERIMENTAL SETUP

2.1 Design of Experiments (DOE)

An unreplicated, two-level factorial DOE (Table 2.1) was used to study the effect of four process parameters (or, in the nomenclature of design of experiments, factors):

1. Average rubbing velocity
2. Weld pressure
3. Upset distance
4. Preheat temperature

The factors were evaluated for their influence on three response variables for the IH and LFW of AISI 1020 steel (a low hardenability carbon steel that has high strength, high ductility, and good weldability):

1. Weld strength (flexural yield strength)
2. Heat affected zone (HAZ) width and peak hardness
3. Energy usage

Average rubbing velocity is equal to four times the amplitude and oscillation frequency, accounting for the distance traveled (4 times the amplitude) in one complete oscillation. Weld pressure is equal to the forge force per unit area of the weld interface. Upset distance is the total distance traveled by the workpiece applying pressure. Preheat temperature was defined as the maximum temperature reached on the weld surfaces due to induction heating. Due to cost restrictions, the factorial experiment was unreplicated, meaning that for each of the sixteen test conditions there was only a single weld. MTI provided their 350 kN (35-ton) LFW machine (Fig. 2.1), and purchased a 25 kW induction heating unit from EFD Induction (Fig. 2.2) for the testing. MTI indicates size of their LFW machines by the maximum forge force capability in tons, and EFD Induction rates their induction heating units by their maximum power output.

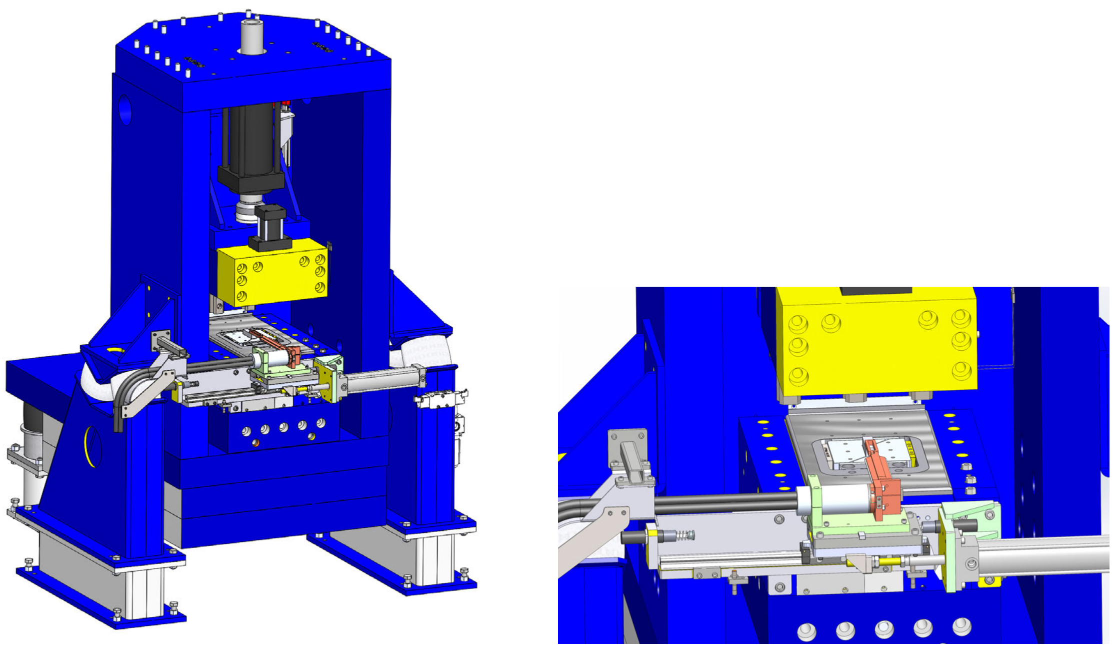

Figure 2.1. 3D model of the MTI 350 kN (35 ton) LFW machine and induction coil shuttle (a) Wide-view (b) Enlarged view of the IH and LFW area.

High and low values for surface velocity (2 mm constant amplitude) and weld

TABLE 2.1

TWO-LEVEL (+/-) FACTORIAL DOE

Weld Number	Pattern	Velocity [mm/s]	Weld Pressure [MPa]	Upset Distance [mm]	Preheat Temp [°C]
1	$--+-$	240	40	4	650
2	$+---$	480	40	2.5	650
3	$---+$	240	40	2.5	850
*4	$+-+-$	480	40	4	650
5	$-++-$	240	100	4	650
6	$+--+$	480	40	2.5	850
7	$++--$	480	100	2.5	650
8	$-+--$	240	100	2.5	650
9	$+-++$	480	40	4	850
10	$++-+$	480	100	2.5	850
11	$--++$	240	40	4	850
12	$-+++$	240	100	4	850
13	$+++-$	480	100	4	650
*14	$-+-+$	240	100	2.5	850
*15	$++++$	480	100	4	850
*16	$----$	240	40	2.5	650

Note: * indicates temperature recorded.

Figure 2.2. EFD Induction 25kW inductive mobile heat generator

pressure were selected in accordance with machine capability (Figs. 2.3a and 2.3b, respectively) and industry experience. Upset distance was chosen according to industry practice at MTI as well as published values for similar tests [39, 46, 62, 83]. Preheat temperature was selected within a 300 °C range of the steady state temperature reached during a mild steel to mild steel linear friction weld [39]. The experiment matrix is documented in Table 2.1. Weld strength and HAZ width / peak hardness were characterized by tension testing and microhardness testing, respectively. Energy usage was measured with pressure sensors located on the oscillator.

2.2 Material Selection and Geometry

For this experiment, the size of the weld interface was 101.6 mm × 25.4 mm and the coupons were 152.4 mm in length (Fig. 2.4). Cold rolled AISI 1020 steel (a low hardenability carbon steel that has high strength, high ductility, and good weldability) was chosen for two reasons: First, the large size of the coupons called for an inexpensive material; low carbon steels are relatively inexpensive metals and easy to obtain. As discussed earlier, the goal of the research was to develop a low cost LFW capability to expand the applications of the technology beyond the aerospace industry. A prime sector that stands to benefit from LFW is the automotive industry,

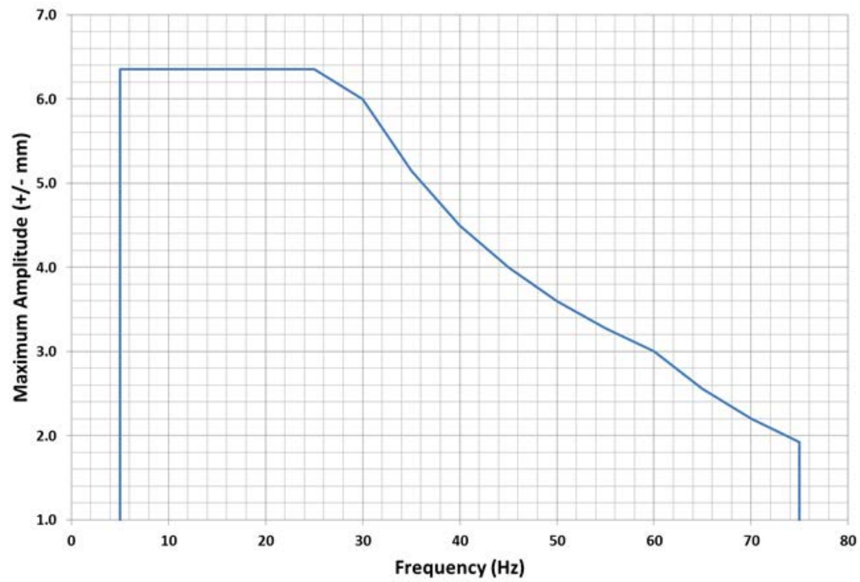

(a)

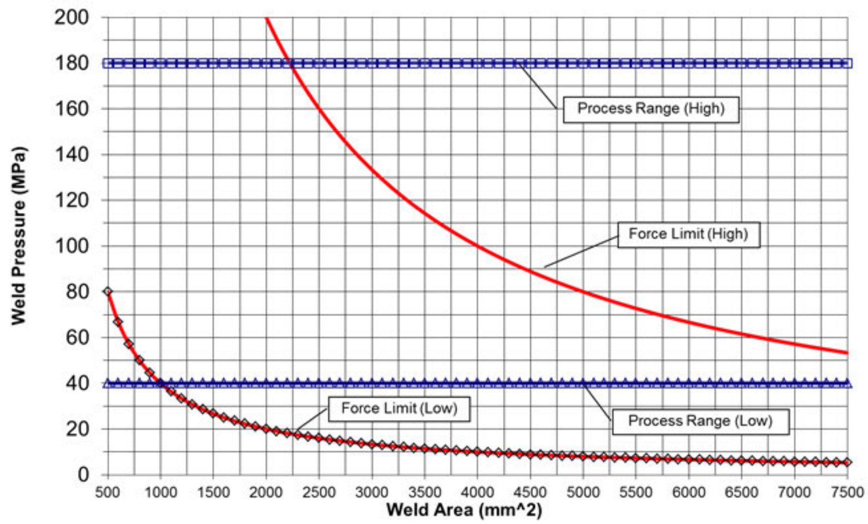

(b)

Figure 2.3. Operating window of the 350 kN (35-ton) LFW machine at MTI. When combined, the values for (a) amplitude, frequency and (b) pressure, can not exceed the envelope

where steel is a commonly used material in chassis fabrication. Therefore, a study using steel will be beneficial for future applications of a low-cost LFW machine.

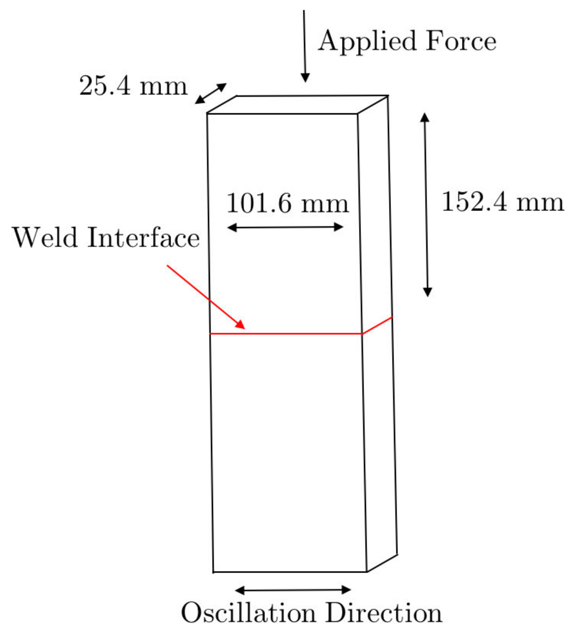

Figure 2.4. Weld coupon dimensions

2.3 IH and LFW Procedure

The following test procedure was developed and used for experiments combining IH with LFW:

1. The lower workpiece is manually secured using a wedging system, tightened by socket head cap screws.
2. The upper workpiece is lifted manually into place, and then hydraulic cylinders engage to clamp the coupon.
3. The weld surfaces are cleaned with acetone using a lint-free cloth.

4. The workpieces are brought into contact, and the load is increased until the desired welding force is reached. The computer records the position of the forge slide at this point and marks it as the "zero position."
5. The workpieces separate and the induction coil is shuttled to a location in between the two workpieces.
6. Current is applied to the induction coil for a specific amount of time associated with the expected temperature rise of both workpieces, as predicted by a set of heating trials with the temperature measurement setup described in Section 2.5.
7. The coil is retracted from the workpieces, and a traditional linear friction welding operation commences.

2.4 Coil Shuttle Mechanism

Figure 2.5 shows a geometrical representation of the induction coil used to heat the interface of the workpieces, and Fig. 2.6 illustrates the flow of current through that coil. The geometry of the 1-turn induction coil was a rectangle with dimensions of 101.6 mm x 25.4 mm x 13 mm. As can be seen in Fig. 2.6, a flux concentrator was placed in the center of the copper coil to concentrate the magnetic flux towards the workpieces so that they experience a higher power at the same current. The coil and power unit was loaned by EFD Induction. Due to cost restrictions, an optimized coil was not designed.

The coil was brazed onto an extension arm that was stiffened with stainless steel brackets to prevent coil movement caused by magnetic force. A hydraulic mechanism was designed specifically for this project to shuttle the induction coil arm into and out of position before and after the preheating stage of the IH and LFW procedure. This design was optimized to minimize the amount of time between the moment when induction heating stops, and the moment when oscillation begins. As a fail safe, LFW would not commence unless the induction arm was entirely in its inactive position as confirmed by a positioning sensor. The time duration between coil retraction and the first oscillations was consistently 0.32 seconds.

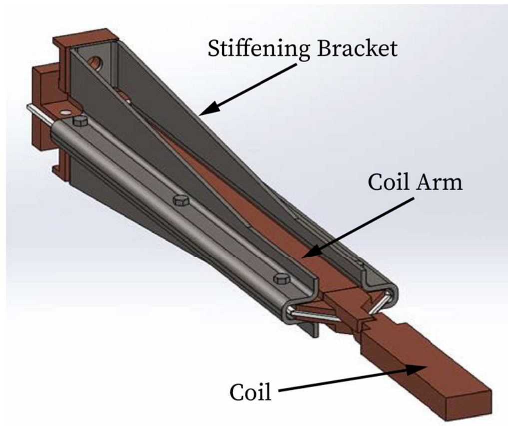

Figure 2.5. 3D computer model of the induction coil arm.

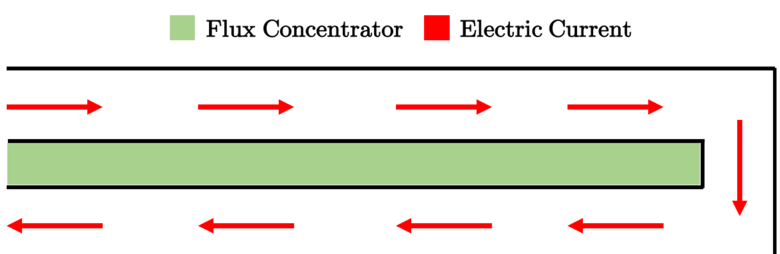

Figure 2.6. Top view of the induction coil.

2.5 Temperature Measurement

Temperature data was recorded in order to correlate the FEM model to the IH and LFW experiments. Several methods for measuring temperature exist, ranging from infrared cameras to pyrometers. Cameras would fail to capture temperature data within the coupons and were cost prohibitive. For this experiment, thermocouples were embedded in the weld coupons along the weld interface at varying depths. Temperatures were expected to exceed 900 °C, so K-type ungrounded thermocouples with nickel-chrome based sheathing were selected for high temperature performance. The thermocouple probe and wire were only 1 mm in diameter so as to maximize the amount of steel in the weld joint by minimizing the amount of space occupied by the thermocouple probe and wire. A K-type amplifier was utilized to linearize the output of the thermocouples and ensure the data was preserved and accurate.

Embedding thermocouples inside workpieces is not trivial and took several design iterations. The biggest challenge was positioning a small thermocouple inside a large coupon just millimeters from the weld interface, as it is very difficult to produce a hole 1 mm in diameter 150 mm deep. Eventually a design was created whereby the thermocouple wires were fed through the coupon from its top side (opposite the weld interface), and exited through holes on the weld interface end. The thermocouples were then silver soldered inside of plugs (Fig. 2.7) that had different preassigned-depth holes created by wire EDM.

The plugs and now-affixed thermocouples were then pressed back into the coupon, and the remaining, pre-calculated material extruding from the weld interface was removed through abrasive machining until coplanar with the coupon. Finally, a high temperature, chemical set cement was poured into the holes from the top side of the coupon to set the thermocouple wires into place in the event that the silver melted during welding. The position of the plugs within the coupon can be seen in Fig 2.8.

Due to the high cost of manufacturing for coupons that could fit thermocouples,

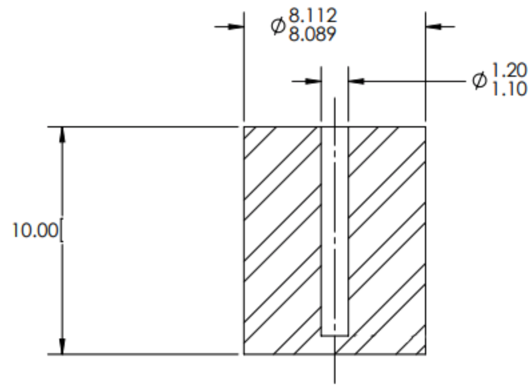

Figure 2.7. Cross sectional view of the thermocouple plugs (Dimensions are listed in millimeters

as well as the high cost for the thermocouples themselves, temperature data was only acquired in four of the 16 tests as indicated in Table 2.1.

2.6 Data Collection

Proper data acquisition (DAQ) plays an essential role in determining validity of results, specifically when comparing LFW experiments with FEA models. The MTI LFW DAQ systems are all 16-bit minimum resolution, anti-alias filtered with a monotonic (evenly time sampled) sample rate of 2048 Hz. This ensures a proper resolution without low-level noise. In addition to the monotonic sampling of each individual channel, all eight of the available DAQ channels use simultaneous sample and hold (S/H), so that all the recordings are synchronized. This allows different recordings to be overlaid on the same plot. For every test run on the lab LFW machine at MTI, there are four standard monitored signals:

1. Forge force
2. Forge position
3. Oscillation force
4. Oscillation position

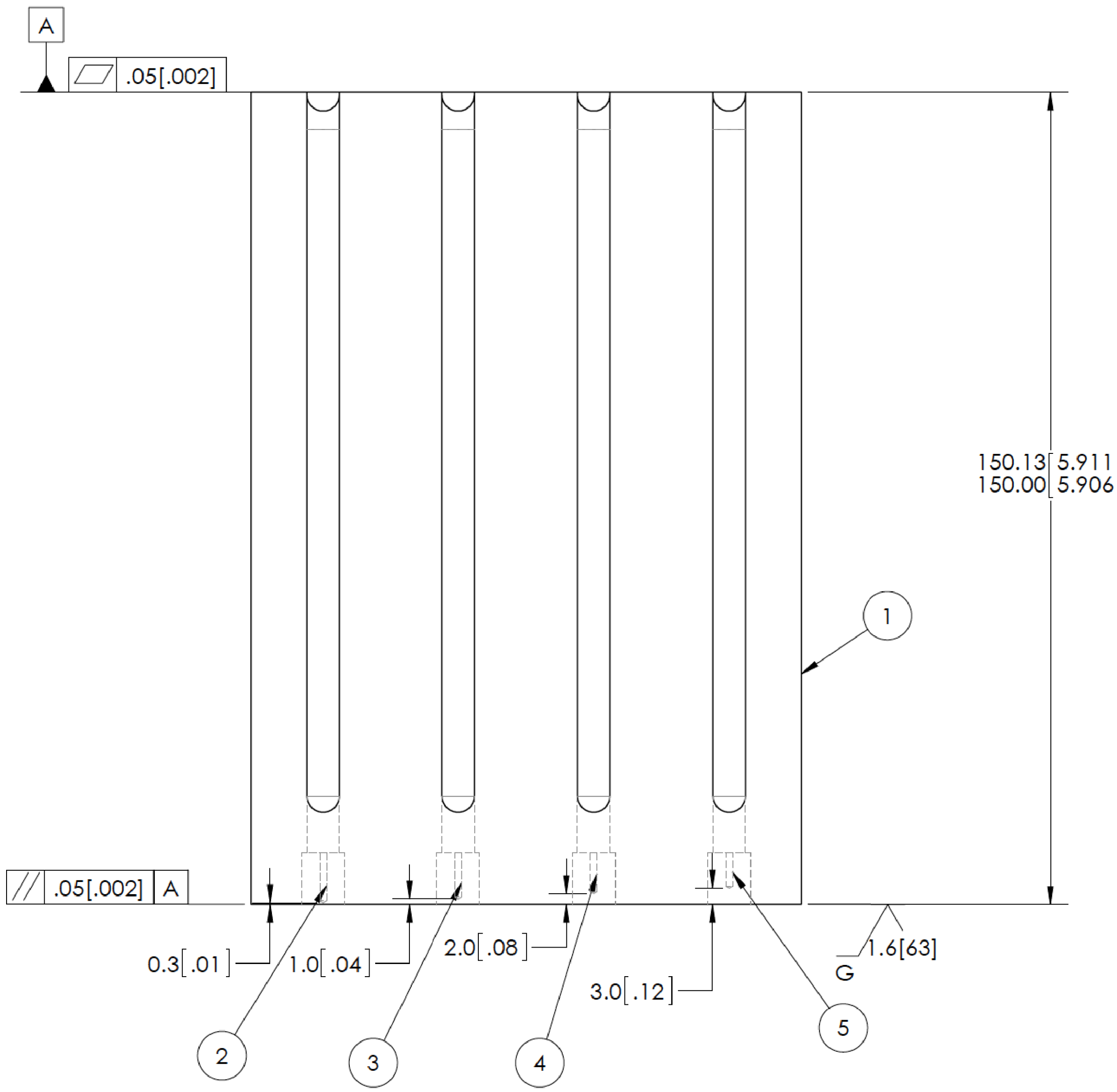

Figure 2.8. Cross sectional view of the upper coupon retrofitted for thermocouple incorporation.

Position measurements are made relative to the machine frame and located as near to the weld surface as possible, and weld forces are measured using the differential pressure across a hydraulic cylinder. In addition to the four standard signals, there are open channels available that in this case were utilized to monitor temperature in four of the 16 weld tests. The data from these channels were used in the calculation of multiple variables which can subsequently be plotted in Matlab using a plugin called sVIEW.

CHAPTER 3

NUMERICAL MODELING OF INDUCTION HEATING

During IH, alternating current in an induction coil induces electric current in a workpiece, causing heating by electric resistance. The depth of heat generation is determined by the size and shape of the electromagnetic field, which is determined by coil shape, coil power, coil frequency, the presence of flux concentrators, and electromagnetic properties of the heated material.

3.1 Previous Work

3.1.1 RFW

This is the first known attempt at externally heating LFW workpiece surfaces in order to reduce energy storage needs. Industry research and development efforts at Manufacturing Technology Inc. have focused on developing the technology for RFW, where a traditional multi-turn induction coil is placed around the outer diameter of a typically solid rod (Fig. 3.1). In this process, the current density is greatest at the surface of the workpiece, which therefore heats at a higher rate than the center of the bar (also known as the skin effect). The difficulty in this process is spreading heat to the center of the rod to obtain a uniform temperature distribution prior to welding. A uniform temperature distribution on the weld surface is desired so that the difference in frictional heating from the center of the weld to the outside is minimized. In RFW, there is already a difference in frictional heating due to the increase in translational speed further from the weld center. Preheating the workpieces with IH increases the difference in frictional heating from the center to outside of the weld joint, unless steps are taken to allow time for the heat to spread evenly to the center of the workpiece. The downside to this strategy is an increase in cycle time for producing welded parts.

3.1.2 LFW

As with RFW, no publications detail the use of IH with LFW. Besides the novelty of the idea, one possible reason for this gap in research is that a cylindrical coil will not uniformly heat a non-cylindrical part (heat will concentrate in the corners and along the edges of the workpiece). In order to overcome this geometric constraint, a pancake coil can be used to heat the weld surfaces prior to welding (Fig. 3.2) [51]. Pancake coils are used extensively in induction heating when it is necessary to heat a part from one side. Even so, uniform generation of heat on the workpiece surface remains a challenge, one that usually involves an optimized IH coil design.

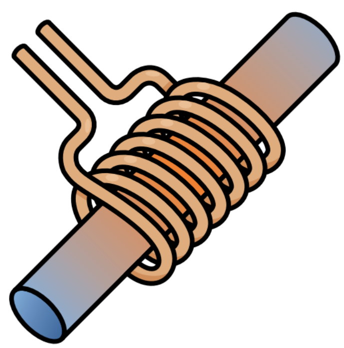

Figure 3.1. Typical induction heating style for RFW [1].

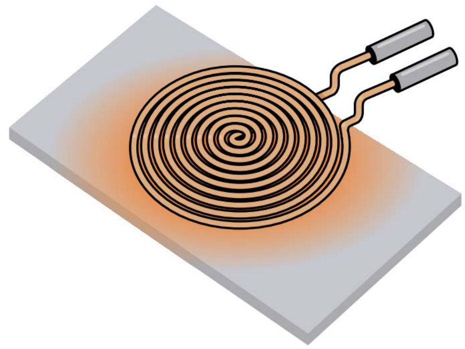

Figure 3.2. Example design for a pancake coil [1].

3.2 Analytical Model

Although IH is not frequently integrated into FRW, IH itself is a process that has been studied extensively. Induction heating has been used as a method of heat treatment and melting in furnaces [29]. There are numerous analytical and numerical formulations of the IH process for multi-turn induction coils. In these formulations, there are closed form design relationships that can be used to analytically predict the magnetic field and the resulting thermal profile of the heated part [26, 27]. Similar design relationships that can be used to analytically predict the thermal profile generated by a pancake coil have remained elusive; results obtained from this type of analysis are not worth comparing against experimental results. Instead, complex finite element simulations are required for such a comparison.

Regardless, an analytical model of the IH process is useful for understanding the fundamental relationships between the IH parameters and the resulting temperature distribution. The following publication describes a simplified analytical analysis of surface heating by induction [14]. The described problem is "a semi-infinite electrically conducting material . . . heated from the surface by induction heating." The governing equation derived from Maxwell's equations is given by

$$\Delta^2 J = \frac{\mu}{\rho}\frac{\partial J}{\partial t}, \tag{3.1}$$

where J is the current density, μ is the magnetic permeability, and t is time [14]. The current density is given by

$$J(x,t) = J(x)\cos(\omega t), \tag{3.2}$$

where x is the distance into the material from the surface and ω is the angular frequency. The two boundary conditions for Eq. (3.1) are a constant current density J_s at the heating surface ($x = 0$), and a finite number at $x = \infty$. The solution to Eq. (3.1) is given by

$$J(x) = J_s \exp\left(-\sqrt{2\mathrm{i}}\,\frac{x}{\delta}\right), \tag{3.3}$$

where δ is the penetration depth in which 86.5% of the power consumption takes place. This value is defined as

$$\delta = \sqrt{\frac{2\rho}{\mu\omega}}, \tag{3.4}$$

where ρ is the electrical resistivity [14]. The higher the frequency during IH, the smaller the penetration depth and higher the concentration of heat at the workpiece surfaces.

The governing partial differential equation for one-dimensional temperature distribution in a semi-infinite solid with heat generation at the interface is given by

$$\rho_m C_p \frac{\partial T}{\partial t} = k\left(\frac{\partial^2 T}{\partial x^2}\right) + \dot{q}, \tag{3.5}$$

where ρ_m is material density, C_p is specific heat, k is thermal conductivity, T is temperature, and $\dot{q}$ is the heat generation due to the current density. That heat generation is given by

$$\dot{q} = \rho |J(x)|^2 = 2\frac{P}{\delta}\exp\left(-2\frac{x}{\delta}\right), \tag{3.6}$$

where P is surface power density, or, the total power consumption per unit surface area.

In order to solve Eq. (3.5) and plot dimensional temperatures, an adiabatic surface boundary condition at $x = 0$ must be assumed. The other boundary condition is a finite temperature at $x = \infty$, and the initial condition is an ambient temperature of the material. With these assumptions, no steady-state solution exists, but if high frequency is assumed ($\omega \to \infty, \delta \to 0$), a solution exists where the surface temperature increases continuously with time, given by

$$T = T_\infty + 2\frac{P}{k}\left[\sqrt{\frac{at}{\pi}}\exp\left(-\frac{x^2}{4at}\right) - \frac{x}{2}\mathrm{erfc}\left(\frac{x}{2\sqrt{at}}\right)\right]. \tag{3.7}$$

where α is the thermal diffusivity, equal to the thermal conductivity divided by density and specific heat capacity. A continuously increasing surface temperature is not physically possible, furthering the need for a functional numerical model for temperature comparison.

However, for the purpose of this analytical exercise, temperature has been plotted as a function of time and distance under the aforementioned assumptions (Fig. 3.3), and under the following experimental conditions. The material was AISI 1020 steel, with conductivity, k = 51.9 W/m-K, material density, ρ_m = 7850 kg/m^3-K, and specific heat, c_p = 486 J/kg-K. The electrical resistivity was 1.59e^{-7} Ohm-m, the frequency (equal to the angular frequency times 2π) was 11000 Hz, and the magnetic permeability was 1.256e^{-4} Ohm-s/m.

In the above analysis, the surface power density can be calculated from the surface current density using Eq. (3.6), however the surface current density was not known for the experiment. Instead, the surface power density was taken as the power output from the IH unit (25.4 kW) divided by the surface area of the two heated workpiece surfaces (5.16×10^{-3} m^2).

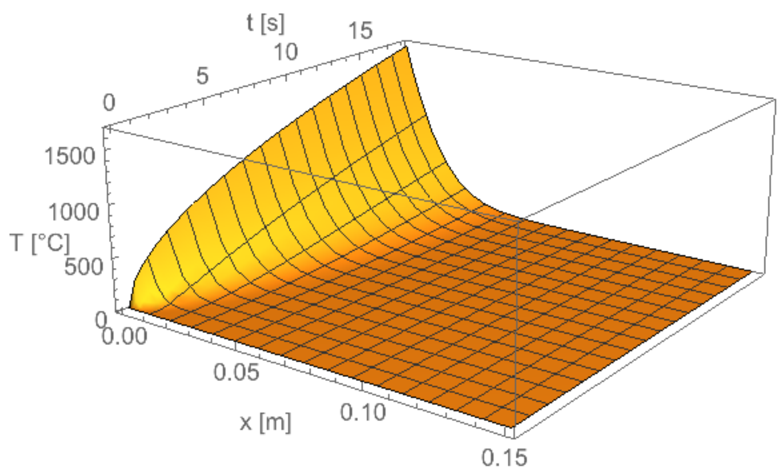

Figure 3.3. Analytical solution for the temperature distribution within a semi-infinite conducting material heated on the surface by IH.

As can be seen in Fig. 3.3, the analytical model over predicts the temperature of the material over time. This is partially due to the assumptions listed above, and partially due to the non-linearity of the magnetic and thermal properties of steel with increasing temperature, furthering the need for a numerical model.

3.3 2D Numerical Model

Within this thesis, the purpose of the IH numerical model was to accurately predict the thermal profile that exists at the moment LFW oscillations begin. In other words, the final step from the IH numerical model will become the first step in the LFW numerical model. Therefore, it is important that the temperature profile at the end of the IH numerical model closely matches the temperature profile as measured by the embedded, k-type thermocouples.

In DEFORM, there are two methods for coupling the induction coil to the workpieces: via the Finite Element Method (FEM), or via the Boundary Element Method (BEM). In FEM, the air is meshed and the magnetic field is calculated throughout the air, whereas in BEM, the air is not meshed and an analytical solution of the magnetic field is calculated on the boundaries. In DEFORM, FEM is computationally more efficient and accurate, however BEM is useful for coils in motion. For this thesis, FEM was utilized because the coil was fixed.

3.3.1 Modeling Geometry

Figure 2.5 shows a 3D representation of the induction coil and extension arm used to heat the interface of the workpieces. Figure 2.6 illustrates the flow of current through that coil. Unfortunately in DEFORM's 2D suite, the IH module is available for *axisymmetric* models only. Modeling a 1-turn induction coil inbetween two workpieces (Fig. 2.5) in an axisymmetric 2D model requires some geometric approximations. Specifically, approximating the rectangular workpieces as two rings with large radii, and approximating the 1-turn coil as a single ring in between the two workpieces.

The geometry of the 1-turn induction coil in DEFORM began as a rectangle 101.6 mm wide and 13 mm tall, 2000 mm from the axis of symmetry (Fig. 3.4). The two workpieces were positioned 2.54 mm above and below the coil workpieces, matching the gap between the coil and workpieces in the experiment. Finally, the air in between the coil and workpieces and surrounding the workpieces was geometrically defined. Figure 3.5 shows a close-up view of the air (blue) surrounding the coil (red) and workpieces (yellow) that are all meshed. When revolved around the axis of symmetry to obtain a 3D representation, the model resembles a 1-turn induction coil heating the surfaces of two tubes (Fig. 3.6).

Figure 3.4. Geometry of an axisymmetric 2D IH model in DEFORM.

3.3.2 Mesh Generation

Identical meshes with tetrahedral elements were generated for the top and bottom workpieces using mesh density windows. In DEFORM, mesh density windows can be defined so that the size of the elements are specific to each window. A window for smaller elements near the heating surface was defined in order to capture steep thermal gradients (Fig. 3.7). This window extended 2 mm into the workpiece for elements 0.75 mm in width. A second window for slightly larger elements was defined

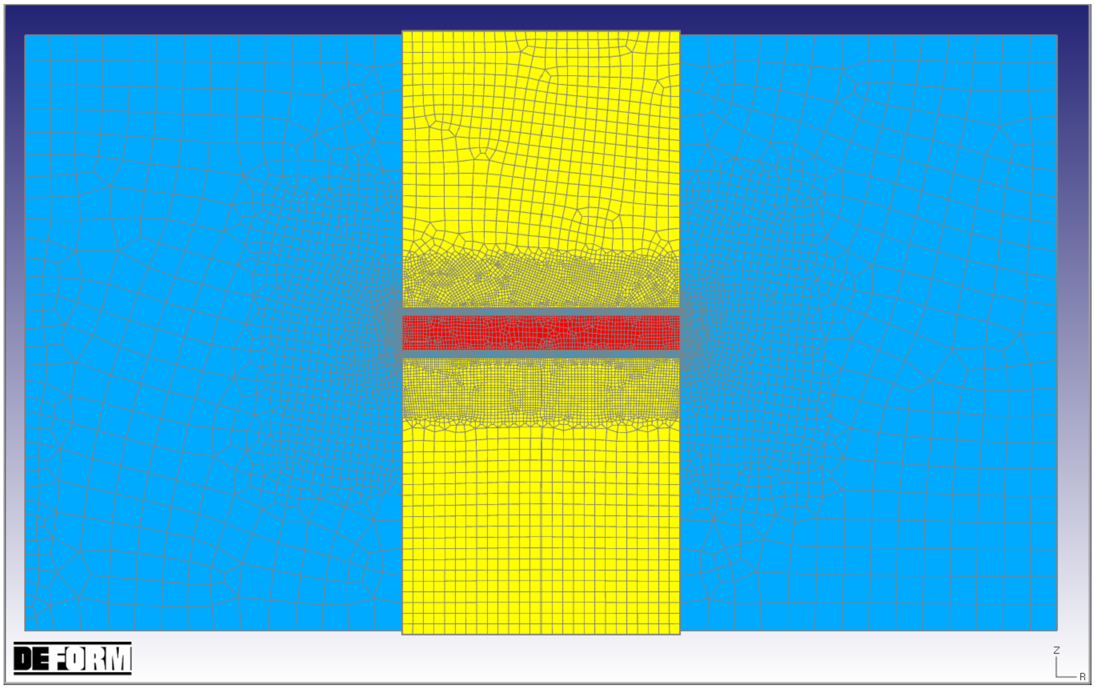

Figure 3.5. Close-up screen capture of the 2D IH model in DEFORM.

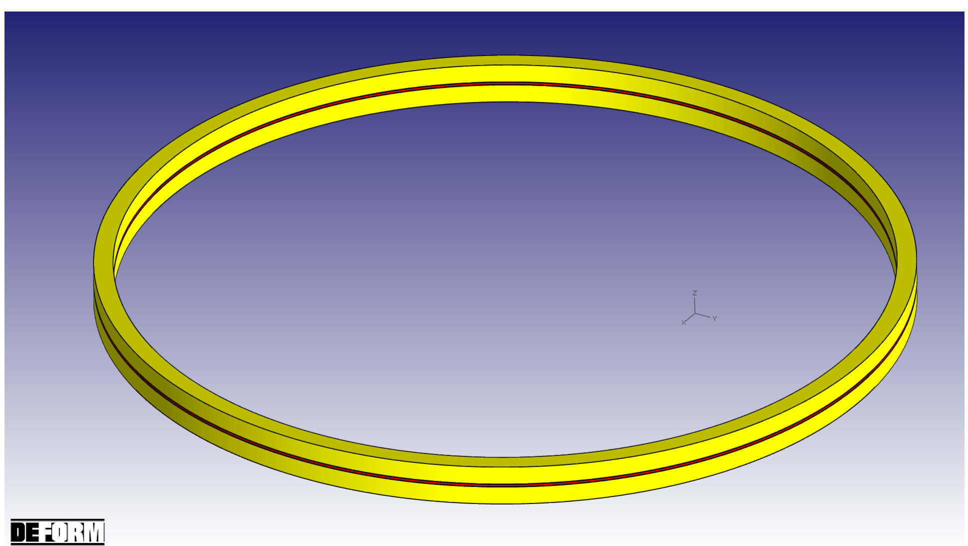

Figure 3.6. 3D representation of a 1-turn coil heating two workpieces in DEFORM. The mesh of air is omitted in order to show coil and workpieces.

that extended 20 mm into the workpiece for elements 1 mm in width. A third and final window for the largest elements extended to the remaining length of the workpiece for elements 4 mm in width.

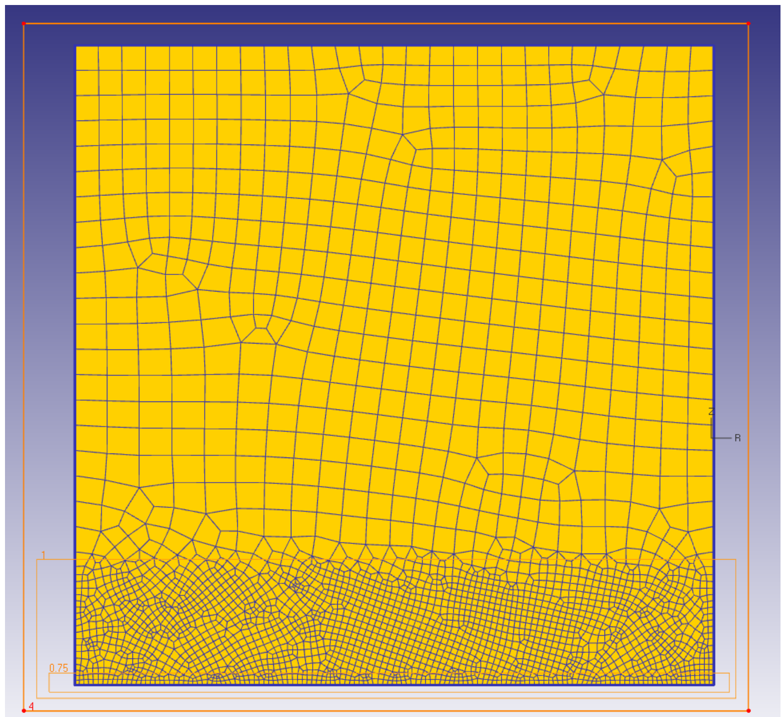

Figure 3.7. Mesh definition of the AISI 1020 steel workpieces in DEFORM for the IH numerical model.

In addition to the mesh density windows, coating layers were added to the mesh on the workpieces. In DEFORM, coating layers can be utilized to add a dissimilar coating material onto a workpiece, or they can be utilized to refine the element thickness near the workpiece surfaces. In the IH model, five coating layers were added (Fig. 3.8) to refine the element thickness and capture the steep thermal IH gradients. Two layers of elements 25 microns in thickness were defined nearest the heating surface, followed by two layers of elements 50 microns in thickness, and lastly by a single layer of elements 100 microns in thickness.

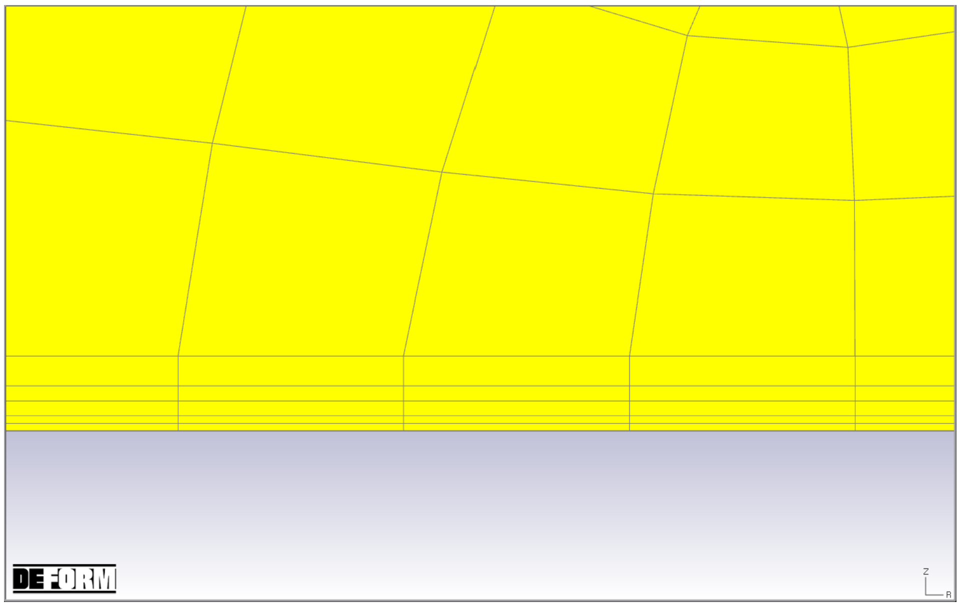

Figure 3.8. Coating elements on the workpiece surface near the IH coil.

For the coil, a mesh with a target of 800 elements was generated with a minimum of four thickness elements and a maximum size ratio of three (Fig. 3.9). In other words, all portions of the object must be spanned by at least four elements, and the edge length of the largest element in the mesh is limited to three times that of the smallest element. Furthermore, a weighting factor was applied for boundary curvature in order to apply a higher mesh density to the boundary of the object. In DEFORM, the error between the number of specified elements and the actual number of elements is usually about 10%, due to the specified geometry and the automatic mesh generation settings. In this mesh, 1,001 elements and 1,122 nodes were generated.

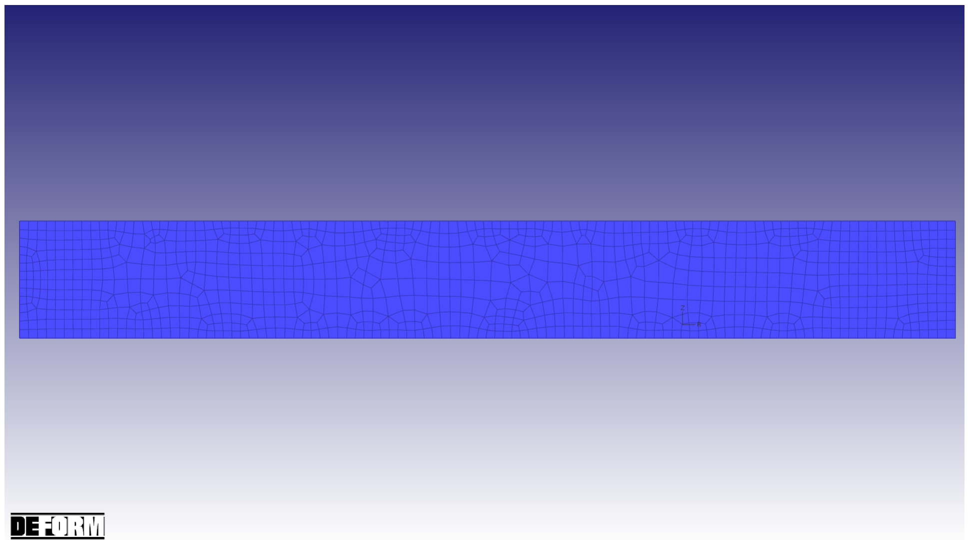

Figure 3.9. Mesh definition of the induction coil in DEFORM for the IH numerical model.

For the air, mesh density windows were again utilized in order to define smaller elements near the coil and larger elements away from the coil (Fig. 3.10). A mesh window encapsulating a thickness of 2.54 mm all all sides of the coil surface was defined for elements 0.5 mm in width. A second mesh window encapsulated approximately the next 8 mm of thickness for elements 1 mm in width. A third mesh window contained approximately the next 9 mm for elements 1.5 mm in width. A fourth contained the next 25 mm for elements 3 mm in width, and a fifth and final window contained the remaining elements that were 10 mm in width.

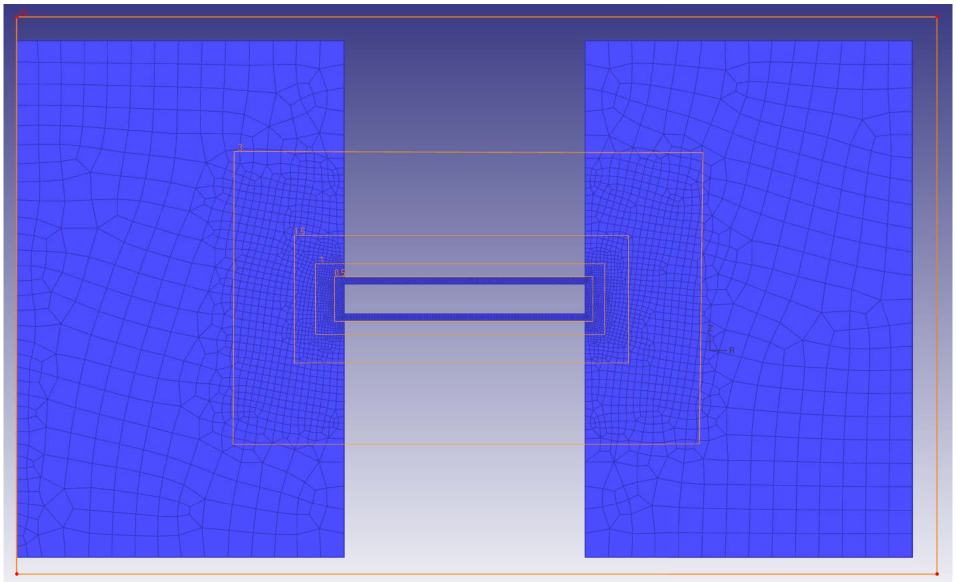

Figure 3.10. Mesh definition of the air in DEFORM for the IH numerical model.

3.3.3 Modeling Parameters

The two most significant modeling parameters for the IH numerical model were coil power and current frequency. As explained in Section 4.2, increasing coil power increases the temperatures induced in the workpieces. Conversely, it also causes a decrease in uniformity of the surface temperature facing the IH coil. Increasing current frequency decreases the penetration depth in which the majority of the power consumption takes place. In other words, it concentrates more of the heating near the weld surface of the workpieces.

In the experiment, an induction heating unit sent 25.4 kW of power into the coil for a predetermined amount of time. The power level was recorded at the IH unit; there was a 0.15 s ramp-up time to reach the maximum power level, and a 0.07 s ramp-down time to return to 0 kW. It is important to recognize that the recorded power level is not the power consumed by the workpieces. The power consumed by the workpieces is much lower than the recorded power levels due to the experimental setup, machine settings, and machine inefficiencies, among other reasons. In DEFORM, the IH module includes a "Source Energy Ratio" parameter that serves as a conversion ratio from electric energy to heat. This parameter can range from 0 to 1000, where 1000 corresponds to 100% conversion.

To approximate the maximum coil power of the machine in a 2D axisymmetric model, the ratio of power to surface area needed to be maintained. In the experiment, the combined surface area of the two workpieces undergoing heating was 5,161 mm^2. As shown in Fig. 3.6, revolving the workpieces around the axis of symmetry creates two tubes that have a combined surface area of 2.66×10^6 mm facing the coil. Multiplying this surface area by the ratio of power to surface area from the experiment gives the power level required for the 2D axisymmetric model: 13,124 kW as obtained from:

$$P_{\text{model}} = \frac{P_{\text{experiment}}}{SA_{\text{experiment}}} SA_{\text{model}}, \tag{3.8}$$

Ramp-up and ramp-down times for power level were matched in the numerical model.

In the experiment, current frequency was set to the maximum setting in an attempt to minimize the size of the HAZ during LFW. During the IH process, software enables capture of current frequency was not available, but it could be manually recorded during testing. On a video recording of the IH unit's display screen, it can be seen that from 0 to 7 s, the frequency level started at 12.25 kHz, dipped to 10.5 kHz, and ramped up to the max frequency of 14 kHz (Fig. 3.11).

3.3.4 Material Properties

Multiple categories of material properties have varying effects on the IH numerical model. For example, electromagnetic properties of AISI 1020 steel will have an effect on the depth and shape of the electromagnetic field, whereas thermal properties like

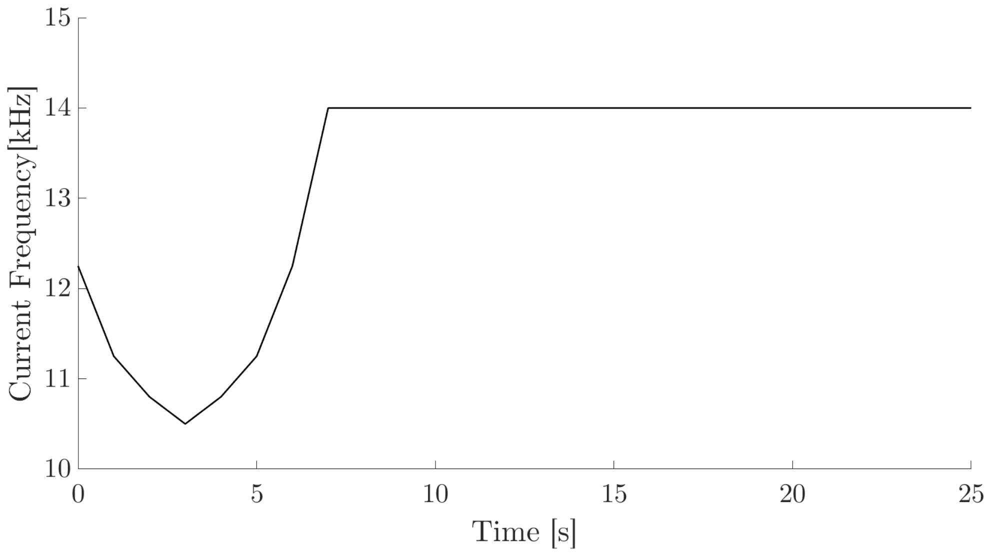

Figure 3.11. Current frequency vs. time for the 25 kW IH coil.

thermal conductivity will affect the depth and gradient of the heat. Plastic flow material properties were not required for the IH numerical model as no deformation will occur.

The three electromagnetic material properties included in the model were electrical resistivity, relative magnetic permeability, and relative magnetic permitivity. Figure 3.12 shows electrical resistivity as a function of temperature and Fig. 3.13 shows magnetic permeability as a function of temperature and magnetic field intensity [57, 64]. Electrical resistivity increases with temperature, meaning that as temperatures rise, the capability of the material to oppose the flow of electric current increases. Magnetic permeability decreases as temperature and magnetic field intensity increase; thus, as temperature and magnetic field intensity increases, the ability of the material to support the formation of a magnetic field decreases. At a high enough temperature, known as the Curie temperature, the ferromagnetic behavior of the material disappears, and the temperature gains due to magnetic hysteresis cease

[3]. Relative magnetic permitivity was constant at 0 [64].

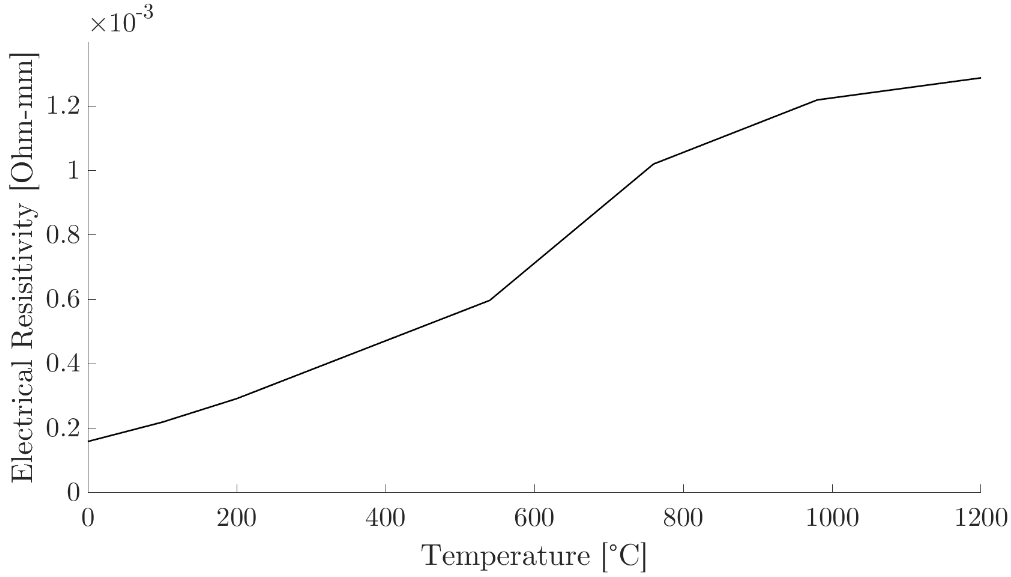

Figure 3.12. Magnetic resistivity of AISI 1020 Steel.

The thermal material properties included in the model were thermal conductivity, volumetric heat capacity, emissivity, and mass density. Figure 3.14 shows thermal conductivity as a function of temperature and Fig. 3.15 shows volumetric heat capacity as a function of temperature [64]. Thermal conductivity decreases with increasing temperature up to 800°C and subsequently levels out. Volumetric heat capacity follows the shape of a bell curve, peaking when the temperature reaches around 750°C. Emissivity and mass density were constant at 0.7 and 7.87×10^{-6} kg/mm^3, respectively [64].

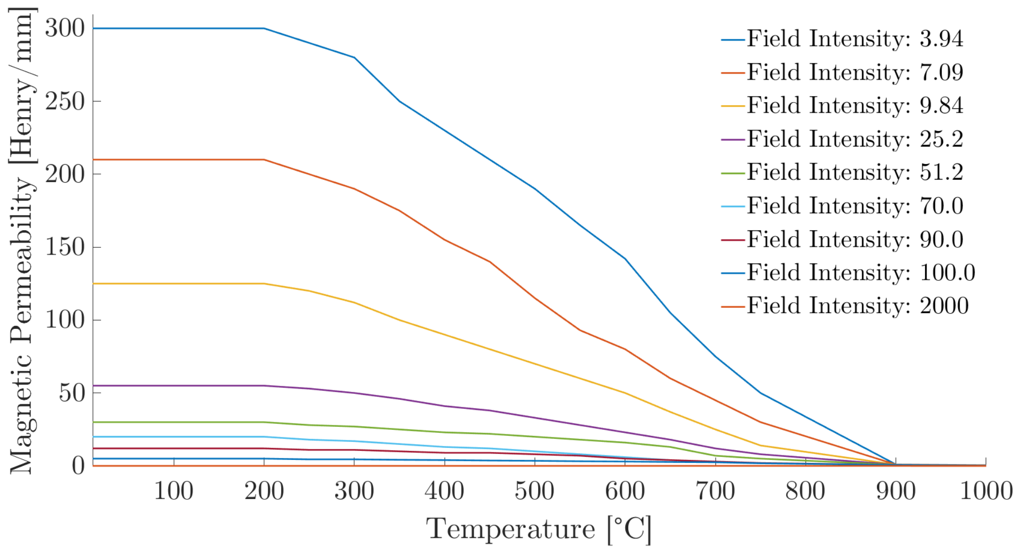

Figure 3.13. Magnetic permeability of AISI 1020 Steel (magnetic field intensity units: A/mm).

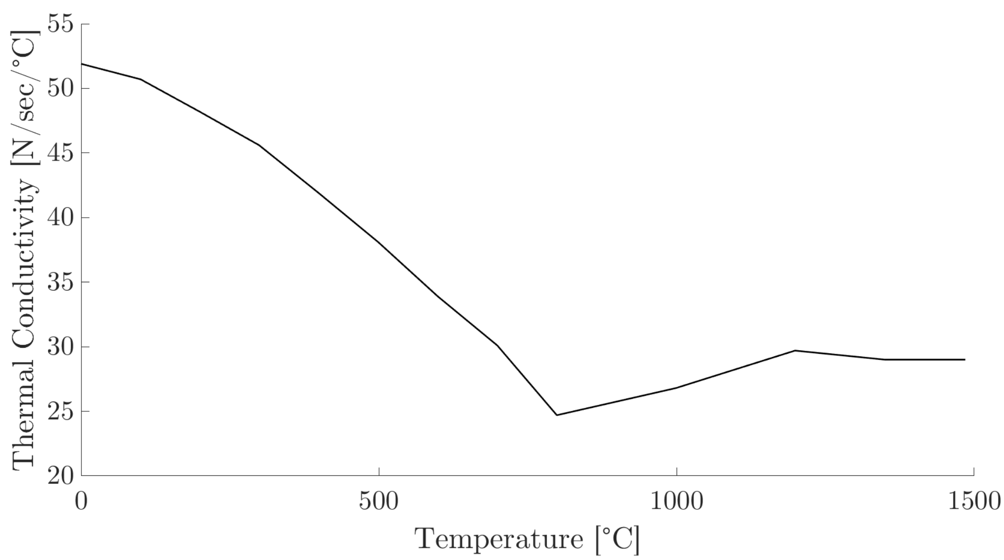

Figure 3.14. Thermal conductivity of AISI 1020 Steel.

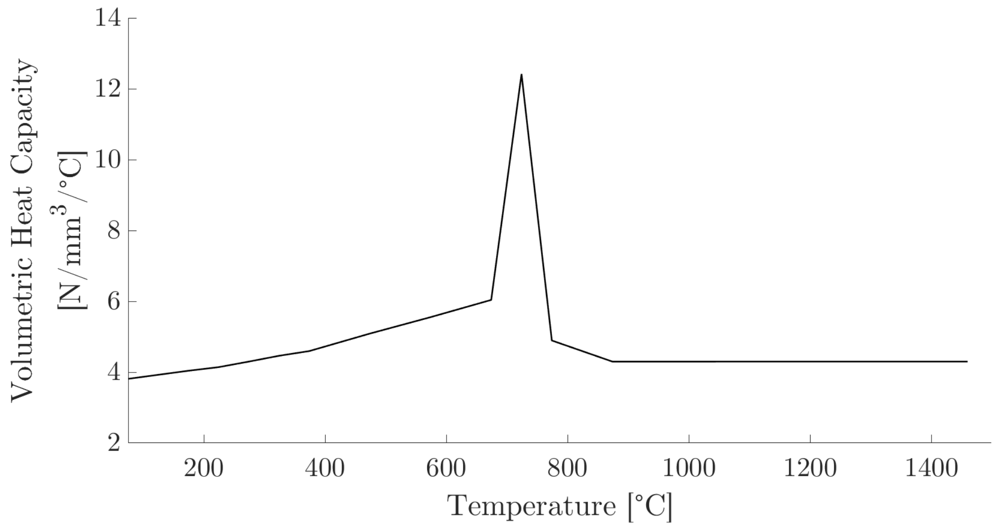

Figure 3.15. Volumetric heat capacity of AISI 1020 steel.

3.4 Model Validation

The experimental temperatures measured during weld number 14 and weld number 16 (as depicted in Fig. 2.8) were compared with corresponding IH numerical models in DEFORM through a method called "point tracking." In point tracking, specific points on objects are selected, and variables are tracked (i.e. temperature, stress, strain). Therefore, points on the mesh in the same locations as the embedded thermocouples can be tracked for temperature comparison.

One difficulty in presenting a valid 2D model of the IH process was coil design. Figure 2.5 gives a 3D representation of the experimental coil geometry, and Fig. 2.5 illustrates the experimental flow of electric current in 2D. The outer profile of the coil measured 101.6 mm $\times$ 25.4 mm, matching the size of the weld interface, and the thickness measured 12.7 mm. Due to the coil geometry, current path, high frequency, and high level of power input, the workpiece surfaces did not heat uniformly, as evidenced by still images of weld 11 during the IH process (Fig. 4.27). In all of the

IH experiments, heat concentrated along the edges of the workpiece surfaces and along the path of the current. A thermal profile like the one shown in Fig. 4.27 could not be replicated in a 2D DEFORM model (Fig. 3.17). In a 2D DEFORM IH model, the path of electrical current is into the screen. When represented in three dimensions by revolving the coil around the axis of symmetry, the current flows around the coil (ring). The circular current path in the 2D model results in a more uniform generation of heat on the workpieces surfaces than the actual current path in the experiment.

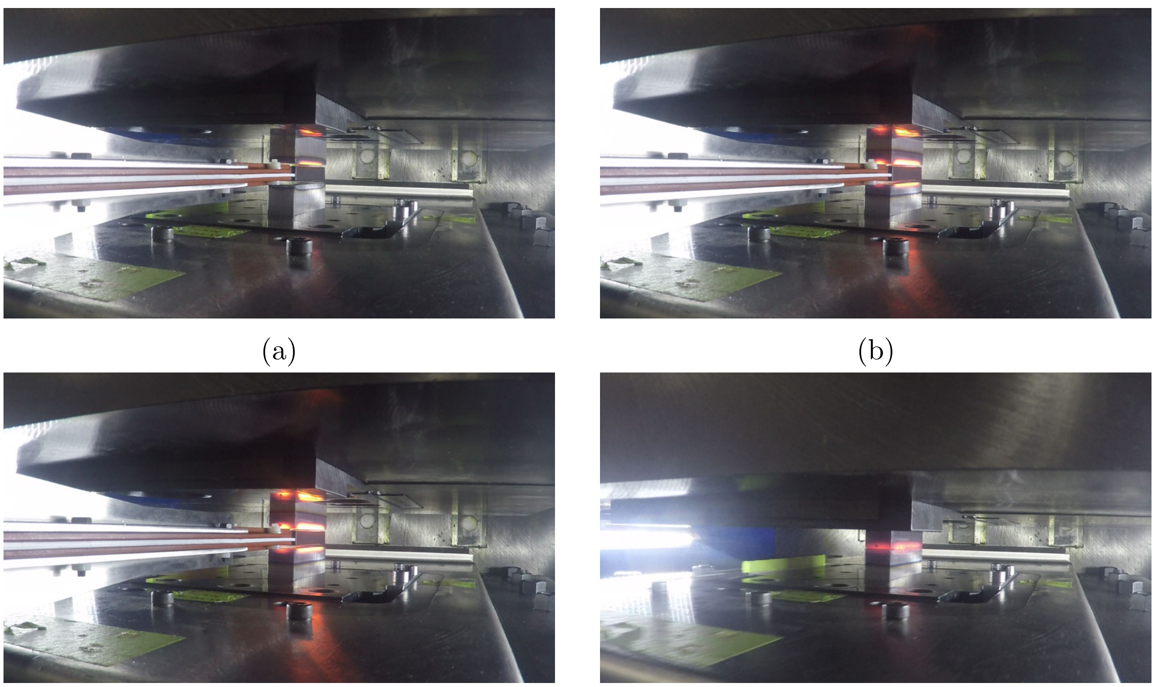

(a) (b) (c) (d)

Figure 3.16. Still images from a video of weld 11 during the IH stage. (a) After 8 seconds of IH (b) After 17 seconds of IH (c) After 25 seconds of IH (d) Workpieces making contact after the IH coil is pneumatically moved aside

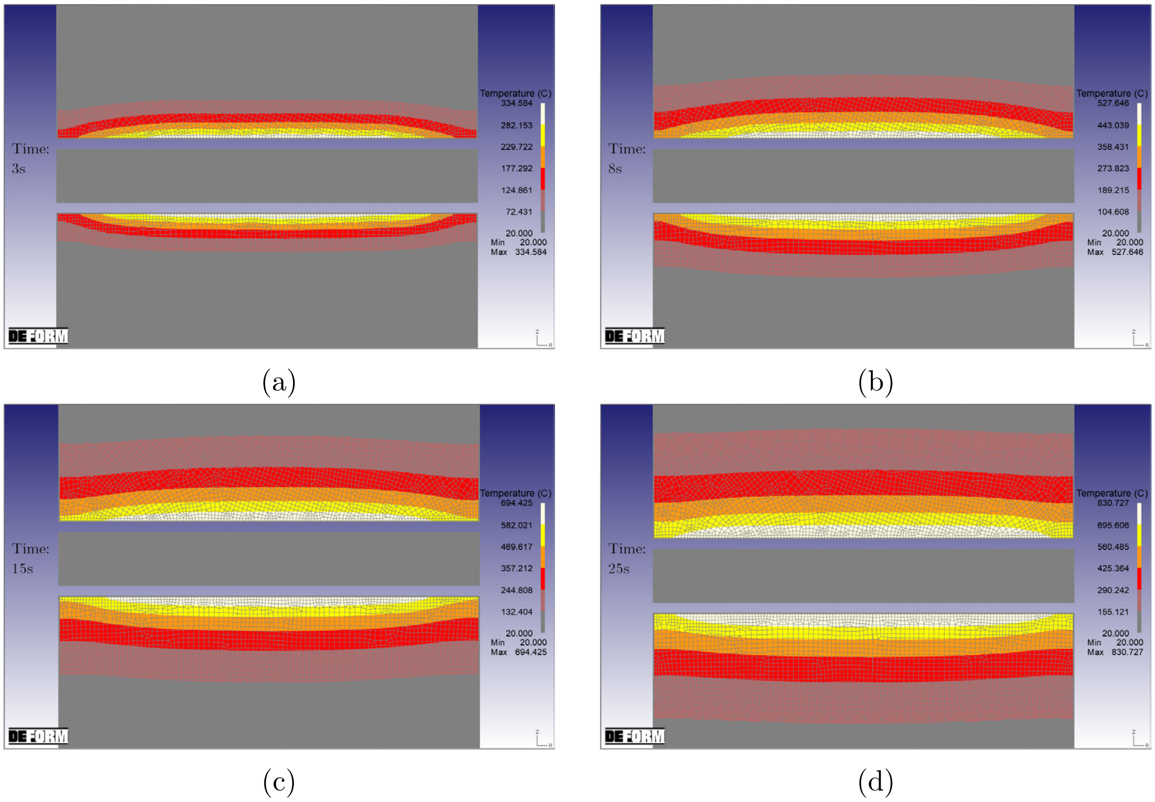

Figure 3.17. 2D model of heat growth during induction heating. (a) After 3 seconds of IH (b) After 8 seconds of IH (c) After 15 seconds of IH (d) After 25 seconds of IH

Due to these limitations, tracking points along the workpieces length (the 101.6 mm direction) produced results in DEFORM that could not be compared or optimized against the temperature measurements. Therefore, instead of tracking points in different positions along the workpieces length, the tracked points were positioned in the center of the workpiece and to the same preassigned depths of 0.3 mm, 1.0 mm, 2.0 mm, and 3.0 mm. Figure 3.18 shows how the points were tracked within the yellow workpiece (the blue object is the air, and the red object is the induction coil. This positioning of the tracked points allowed for an optimization of the thermal profile based on temperatures recorded during welds 14 and 16 for both the low and high levels of preheat, respectively.

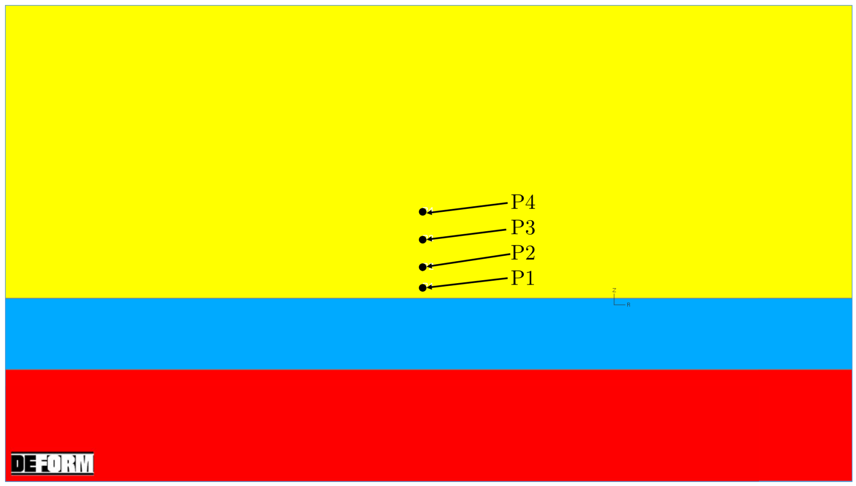

Figure 3.18. Tracking points for temperature data in DEFORM for the IH numerical model (P1 = 0.3 mm, P2 = 1.0 mm, P3 = 2.0 mm, P4 = 3.0 mm).

Therefore, multiple simulations were executed in DEFORM, adjusting the source energy ratio until a solution converged in which the error between each thermocouple measurement and its corresponding tracked point was minimized.

3.5 Results and Discussion

By adjusting the source energy ratio, it was possible to minimize the maximum amount of error between a thermocouple and its corresponding tracked location in the model at the moment the IH phase ends. As stated, the purpose of the IH numerical model was to provide the most accurate initial condition for the LFW model, that is, the closest representation of temperature profile inside of the workpieces prior to the LFW phase of the IH and LFW process. This approach led to the closest approximations of the individual thermocouple temperatures and the associated temperature profile.

For weld number 14, the workpiece surfaces were inductively heated for 25 seconds; in DEFORM, the source energy ratio was adjusted until the error was minimized. The minimum achievable level of percent error was 4.9% with a source energy ratio of 422 (Fig. 3.19). For weld number 16, the workpieces surfaces were inductively heated for 18 seconds. The percent error was minimized to 8.4% with a source energy ratio of 372 (Fig. 3.20).

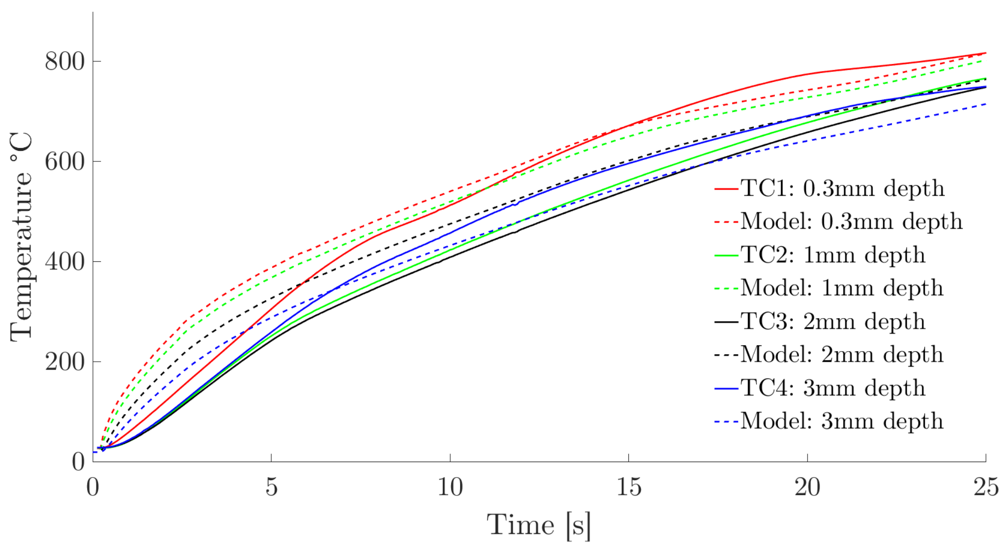

Figure 3.19. Temperature comparison of IH with the DEFORM 2D numerical model for weld 14.

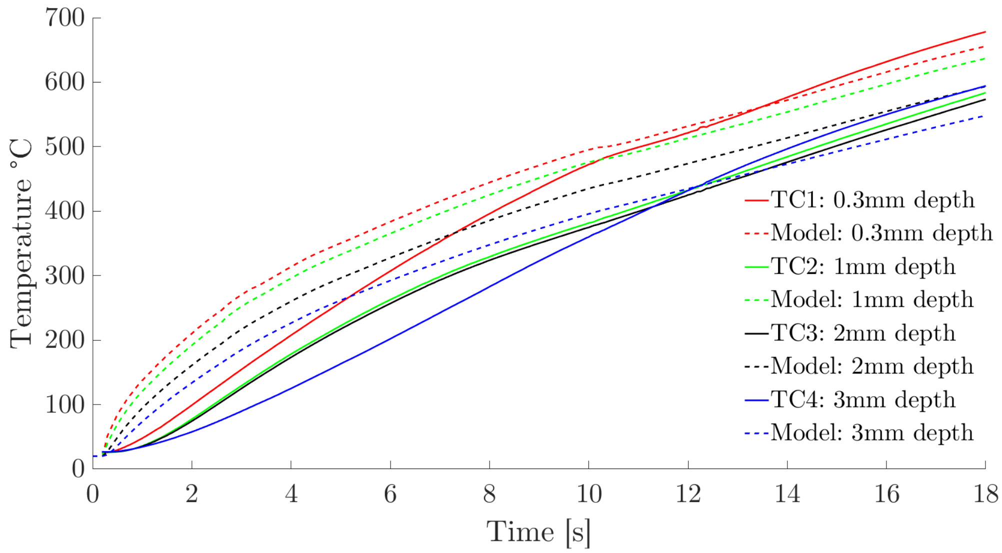

Figure 3.20. Temperature comparison of IH with the DEFORM 2D numerical model for weld 16.

Using the converged source energy ratio for weld number 16 of 372, another plot was generated for the analytical model (Fig. 3.21). This time, the surface power density ratio in Eq. (3.6) was multiplied by the source energy ratio of 372/1000. As shown in Fig. (3.21) for the thermocouple placed 3 mm from the weld surface, this results in a much closer approximation of the temperatures induced in the workpiece.

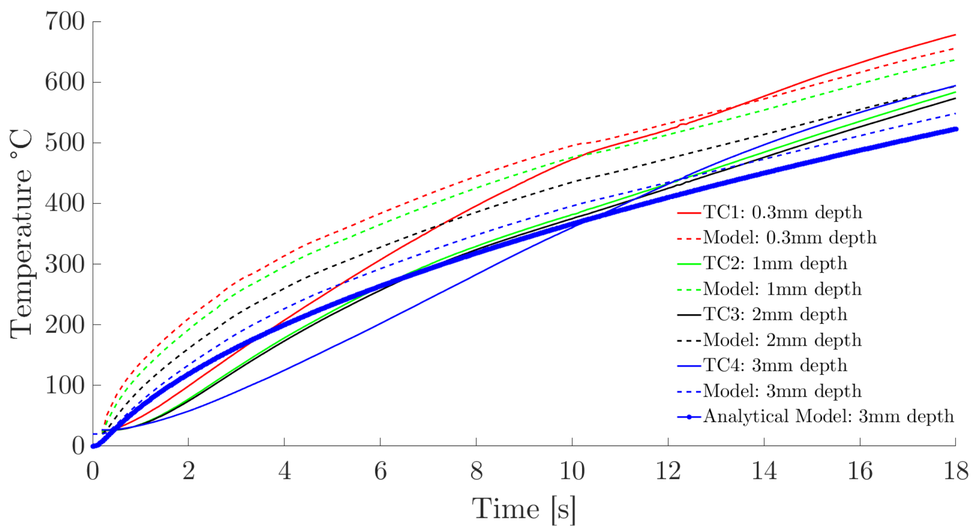

Figure 3.21. Temperature comparison of IH with the DEFORM 2D numerical model and the analytical model

CHAPTER 4

NUMERICAL MODELING OF LINEAR FRICTION WELDING

4.1 Previous Work

While there is a large absence of published hybrid IH and LFW development efforts, there is a strong research effort being directed at conventional LFW modeling. Multiple research groups have attempted to model this process with varying results. Currently, computer models use three different approaches:

1. Model the two workpieces as individual objects. [13, 18, 24, 25, 67, 68, 74, 81].
2. Model one workpiece oscillating against a non-deformable object. [10, 36–41, 69, 73].
3. Model a single body representing two workpieces. [45, 46, 62, 63, 70, 71].

There are limitations to all three model types. In the first, the coefficient of friction is difficult to incorporate during the initial phase of LFW and mechanical mixing of the workpieces is neglected. In the second, the problems are similar to the first, but computational cost is cut in half. In the third, the stages prior to sticking friction (100% contact) are not modeled. Table 4.1 summarizes LFW modeling attempts as they relate to the software used, the dimension and model type, the finest mesh size, and the material data employed to describe the materials being joined.

To date, there is no fully functional two or three-dimensional LFW model; that is, a model that can run from start to finish, accurately predicting temperature, stress, strain, and flash morphology. This is a significant technical shortcoming slowing the application of LFW to commercial joining processes. The desired software characteristics for modeling LFW are:

1. Two separate and deformable workpieces.
2. Variable sized mesh that defines smaller elements near the weld surface to capture steep thermal and strain gradients.
3. Thermo-mechanical coupling to account for the effect of mechanical work on temperature and vice versa (Mechanical work due to friction and plasticity affects the temperature field which influences the stress and strain field).
4. Material non-linearity. Models must take into account the temperature dependence on material properties.
5. Multiple thermal boundary conditions (BCs) including: conduction at the interface, convection losses due to surrounding air, and radiation losses when reaching high temperatures.
6. Complex frictional BC. This BC must take into affect the variation of contact area with time (the sinusoidal movement of one of the workpieces dictates that the contact area will not be constant throughout). Furthermore, the BC must not be limited to a specific material or experiment; the vast majority of LFW models base the frictional heat input from experimental data instead of physics based models.
7. A 2D model must take into account over-prediction of plasticity at the weld line due to the plane-strain assumption, which neglects material extruded in the transverse direction to oscillation.
8. Mechanical mixing of the materials. In LFW, dissimilar materials are often welded together. Models that account for mechanical mixing typically model the initial phase separately from the latter three phases, mapping data from the end of the first phase onto the beginning of another so that the two initial workpieces can be combined into one. Currently, mechanical mixing can only occur when 2 materials are part of a single modeled workpiece.

TABLE 4.1
PAST LFW FEM SIMULATION PUBLICATIONS ORGANIZED BY RELEASE YEAR

Publication	Year	Software	Dimension/ Approach Type	Finest Mesh Size [mm]	Material Data
Vairis and Frost[73]	2000	ELFEN	2D/1	n/a	Tabular
Jun et al. [69]	2008	DEFORM	3D/2	n/a	n/a

TABLE 4.1
CONTINUED

Publication	Year	Software	Dimension/ Approach Type	Finest Mesh Size [mm]	Material Data
Li et al. [40]	2009	ABAQUS	2D/2	0.5	Johnson-Cook
Sorina Müller et al. [68]	2010	ANSYS	3D/1	0.125	Tabular
Ceretti et al. [13]	2010	DEFORM	2D/1	0.6	Tabular
Turner et al. [70, 71]	2011	Forge	2D/3	0.25	Tabular
Fratini and La Spisa [17]	2011	DEFORM	3D/1	0.5	Equation-based
Wu [81]	2012	ANSYS	3D/1	0.5	n/a
Li et al. [35]	2012	ABAQUS	2D/2	0.5	Johnson-Cook
Kiselyeva et al. [30]	2012	ANSYS	2D/1	n/a	n/a
Fratini et al. [18]	2012	DEFORM	3D/1	0.5	Equation-based
Li et al. [36]	2013	ABAQUS	2D/2	0.5	Johnson-Cook
Li et al. [38]	2013	ABAQUS	2D/2, 3D/2	0.5	Johnson-Cook
Song et al. [67]	2013	ABAQUS	2D/1	n/a	Johnson-Cook and tabular
Schroder et al. [63]	2013	DEFORM	2D/3	0.08	Tabular

TABLE 4.1
CONTINUED

Publication	Year	Software	Dimension/ Approach Type	Finest Mesh Size [mm]	Material Data
Li et al. [37, 39]	2014	ABAQUS	3D and 2D/2	0.75	Johnson-Cook
Grujicic et al. [25]	2014	ABAQUS	2D/1, 3D/1	n/a	Johnson-Cook
Zhao et al. [83]	2014	ABAQUS	2D/2	1.00	Tabular
McAndrew et al. [45]	2014	DEFORM	2D/3	0.25	Tabular
McAndrew et al. [46]	2014	DEFORM	2D/3	0.25	Tabular
Schroder et al. [62]	2015	DEFORM	2D/3	0.08	Tabular
Buffa et al. [10]	2015	DEFORM	3D	n/a	Tabular
Lee et al. [32]	2015	DEFORM	2D/3	0.25	Tabular
McAndrew et al. [47]	2017	DEFORM	3D/3	0.5	Tabular

Note: Updated from [72].

4.1.1 Two-Dimensional Models

The first attempt of an FEA simulation of LFW was performed by Vairis and Frost [73], who used the FEA software Elfen to model the process with one work-piece made up of 764 elements oscillating against a non-deformable object (Table 4.1). Implementing a Coulomb friction model, the friction coefficient (along with mechanical properties) for the Ti-6Al-4V workpiece was defined only as a function of temperature, the values of which were interpolated from limited data defined over a 0-900°C temperature range. Furthermore, the effect of oscillatory movement on contact area was neglected. Figure 4 shows that thermocouple data showed reasonable correlation between the model and experiment. However, Vairis et al. noted that error sources in the thermocouple data were associated with: the slow rate of probe temperature approach to the surrounding metal, response time, and positioning of the junction in the specimen. The results proved that numerical modeling of LFW was possible, but needed further improvement.

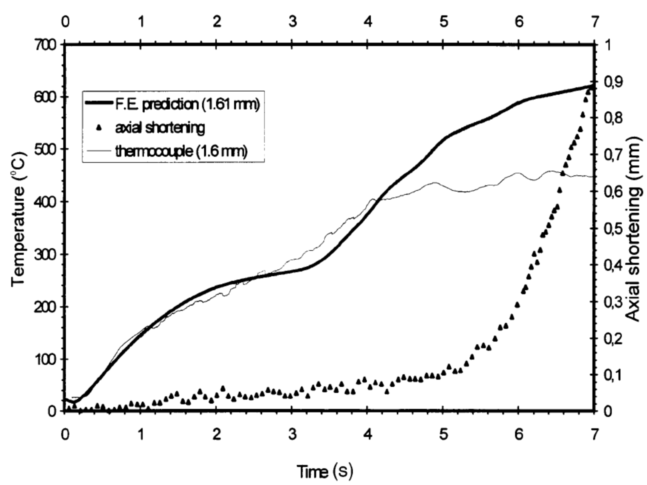

Figure 4.1. Comparison between experimental and finite element temperature data [73]

A decade later, Li et al. [40] attempted to improve the LFW model created by Vairis and Frost, using the commercial FEA package ABAQUS instead of Elfen. As before, only half of the domain was modeled. A variable size mesh was incorporated into the oscillating workpiece to define smaller elements near the weld surface, leading to finer interface temperature calculations; a maximum temperature of 1000°C was calculated at the weld line, and thus material properties were extrapolated to fit the required temperature range. Temperatures were likely higher in this model compared to the Vairis and Frost model because the smaller elements near the interface were able to capture the steep temperature gradient (Fig. 5). The frictional heat input was defined by conventional Coulomb friction for the first phase, with the friction coefficient varying as a function of temperature. Li confirms an equation for heat input, HI, needed for a successful weld as:

$$HI = 4\mu f a F_f, \tag{4.1}$$

where μ is the coefficient of friction, f is the frequency, a is amplitude, and F_f is the friction force (friction pressure times sectional area). A minimum heat input for a successful TC4 titanium alloy weld was calculated to be 1.35 x 10^7 W/m^2. Li later compared this model to results for RFW and friction stir welding [35].

Ceretti and Fratini et al. [13] used DEFORM to model the LFW of AISI 1045 steel. The model used thermal material data from DEFORM's library. A Tresca friction model was incorporated by defining a shear factor as a function of time. The shear factor was derived from the material model itself. The model was verified by comparing the upset from the experiment with the model; the results were described as "satisfactory." Ceretti stated that a finer mesh is needed to capture the steep thermal gradient at the interface. This research group was the first to utilize DEFORM, a software package widely used in recent friction welding models.

Turner et al. [70, 71] developed an LFW model in which the flash morphology, temperature, upset rate, and residual stresses were validated for a titanium alloy. Us-

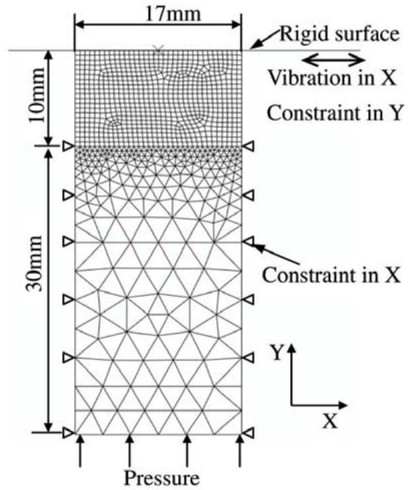

Figure 4.2. 2D model with variable size mesh and appropriate boundary conditions [40]

ing the software package Forge, Turner et al. modeled the equilibrium and transition phases, assuming a “reasonable” temperature profile for the first step of the model (Fig. 4.3a). This assumption was justified by noting minimal differences in upset (Fig. 4.3b), weld line temperature (Fig. 4.3c), and temperature profile (Fig. 4.3d) during the last three phases of LFW after considering four different initial temperature profiles (Fig. 4.3a). This approach reduces the model complexity because only a sticking friction condition is required. Turner discovered that the residual stresses from LFW are primarily a consequence of the cooling of the part after the joint is formed.

Kiselyeva et al. [30] modeled the equilibrium phase of LFW using ANSYS. During the equilibrium stage, an isotropic material model was utilized with a Coulomb coefficient of friction defined as a function of temperature. The effect of oscillatory movement on contact area was neglected. To validate the model, Kiselyeva measured the sizes of the plastic deformation zones (defined as the thickness of the material that undergoes plastic deformation) and found that the measurements were within 2% of the results from the FEA model.

Li et al. [36] adapted their LFW model to a different material (carbon steel) and investigated the effects of heat reflux in the cooling phase of LFW. The study discovered a quicker cooling rate at the weld center because of the heat reflux from the flash to the center of the weld. The first phases of LFW were not detailed, and instead focused on the cooling phase. However, the model indicated that frictional heat input in the form of a Coulomb-based friction coefficient was defined as a function of temperature. Li et al. applied a Johnson-Cook plasticity model to account for the material properties of the steel and to better understand phase transformation during the LFW of a titanium alloy [37]. Among results characterizing grains within the microstructure, Li et al. noted that as weld pressure increased, the joint strength approached that of the base material. Only after post weld heat treatment did the strength of the joint become greater than the base material.

Song et al. [67] investigated the distribution of residual stresses in aluminum alloy AA2024 with ABAQUS/CAE using a balanced master-slave contact arrangement to more accurately depict the contact pressure at the interface. Song et al. proposed a response curve for residual stress using four data points. The model correlated well to the experimental measurements of upset rate, total upset, temperature and residual stress. However, since the paper focused on residual stress formation, determination of the frictional heat generation was not discussed.

Schroder et al. [63] used DEFORM to model all the phases of LFW for turbine engine applications, and therefore considered Ti-6Al-4V, the most widely used titanium alloy for blisks. In the initial stage, referred to as the conditioning stage by Schroder et al., a temperature dependent Coulomb-based coefficient of friction was employed based on experimental in-plane and normal force as well as thermal measurements. The final step from the conditioning stage was used as the initial condition for the

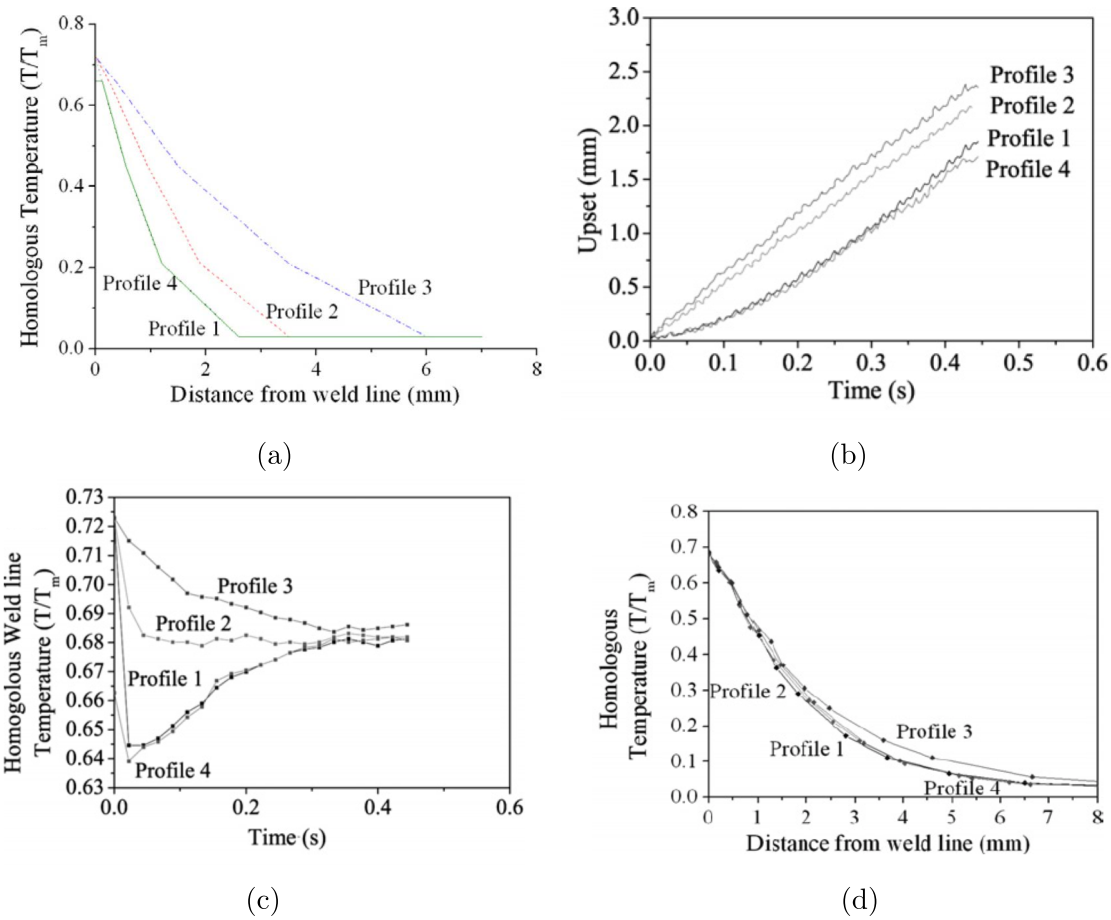

Figure 4.3. (a) Initial thermal profiles assumed for the modeling trials to investigate sensitivity. (b) Prediction of upset curves, (c) peak weld line temperatures, (d) and temperature profile after 20 cycles of LFW for models using the four profiles from (a). A melting temperature of 1660°C was assumed [70]

equilibrium stage when the two workpieces are treated as a single object. Schroder et al. reported "reasonable" agreement between the experimental heating rates and model results to justify the accuracy of the conditioning model, and notes that with this approach it is possible to model the entire LFW process.

Grujicic et al. [25] created an FEM model in ABAQUS for 2D and 3D LFW modeling of a precipitation hardened steel. Focusing on microstructural changes within the weld, the model was able to predict mean radius precipitate size with good agreement to experimental values. A Coulomb friction model was used to define the boundary condition at the weld interface; the coefficient of friction was defined as a function of temperature, slip velocity, and contact pressure.

Zhao et al. [83] used ABAQUS to simulate the temperature distribution and deformation trends in the LFW of TC11 and TC17 titanium alloys. Modeling one of the workpieces as rigid, Zhao simulated contact with a temperature dependent coefficient of friction within a Coulomb friction model; the shape of the friction coefficient curve was almost bell-like (Fig. 4.4). Results confirm the phenomena of heat reflux in the cooling phase of LFW as reported by Li et al. [36]. The model was correlated with upset measurements and showed errors of less than 10% with the model.

McAndrew et al. [45] created a model in DEFORM to model forces in LFW of Ti-6Al-4V, as well as investigate the influence of process parameters on surface contaminant removal [46]. McAndrew et al. implemented two methods in modeling the initial phase: the first used power input calculated from force and displacement history, assuming a perfect sinusoidal displacement,

$$E_x = \int_0^T F_f u \mathrm{d}t, \tag{4.2}$$

where E_x is the total energy inputted to the weld interface, F_f is the frictional

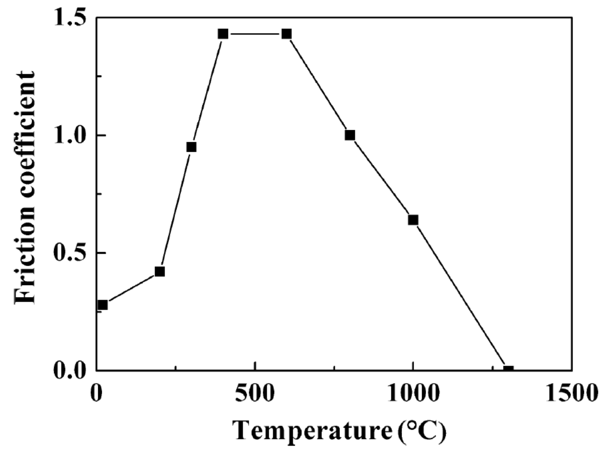

Figure 4.4. Coulomb coefficient of friction between TC11 and TC17 titanium alloys [83]

force, T is the total duration of the weld, and u is the velocity. The second method used an average power input derived from a statistical analysis. The resulting heat flux was applied to the weld surface, linearly reducing to 50% of this value at an amplitude, A, away from the edges to account for overhang at the far end of each oscillation (Fig. 4.5). McAndrew et al. were the first to publish a DOE used in a regression analysis, resulting in formulas for burn-off rate, duration, weld power, interface force, friction coefficient, and process energy as a function of various process inputs. The many outputs were primarily dependent on applied force and average rubbing velocity,

$$v = 4fa, \tag{4.3}$$

where f and a are oscillation frequency and amplitude respectively. Through the regression analysis, McAndrew et al. discovered that interface force (the in plane force minus mass of the chuck/workpiece times acceleration) is insensitive to average rubbing velocity. Using point tracking within the DEFORM software, McAndrew et al. were able to evaluate surface contaminant removal. Results showed that high applied forces lead to less material consumption to remove surface contaminants (Fig. 4.6).

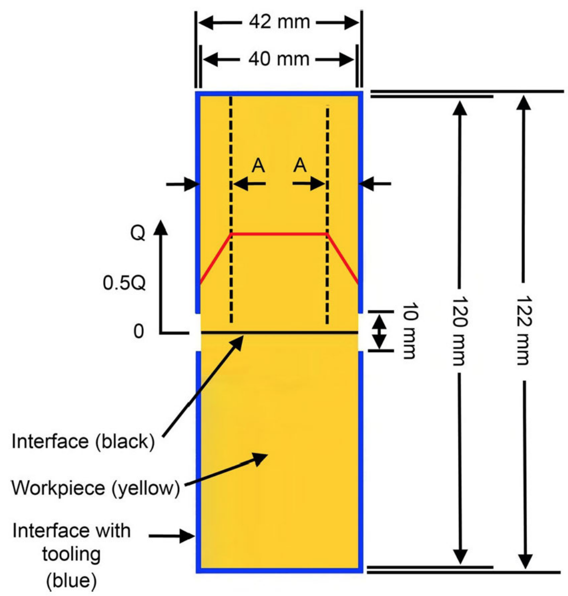

Figure 4.5. Illustration of the 2D model, including the linear reduction of heat flux by 50% at an amplitude (A) away from the edges [45].

Schroder et al. [62] examined the LFW of Ti-6Al-4V with experiments and modeling in DEFORM. Using a temperature dependent friction coefficient derived from measurements of the in-plane and normal forces and modeled temperatures at the center of the weld line using a time dependent friction coefficient, the initial phase was modeled. The point at which the initial phase ends and the equilibrium phase begins was defined as the point at which 95% of the maximum upset rate is reached. Schroder found the plain strain assumption (2D) to be more appropriate at smaller frequencies, larger pressures, and particularly the lowest amplitudes (Fig. 4.7). Schroder also proposed a new equation to define the energy input rate,

$$\dot{Q} = \frac{\int F_f u \mathrm{d}t}{\Delta t A}. \tag{4.4}$$

where F_f is the frictional force, u is the sliding velocity, t is time, and A is the weld cross sectional area.

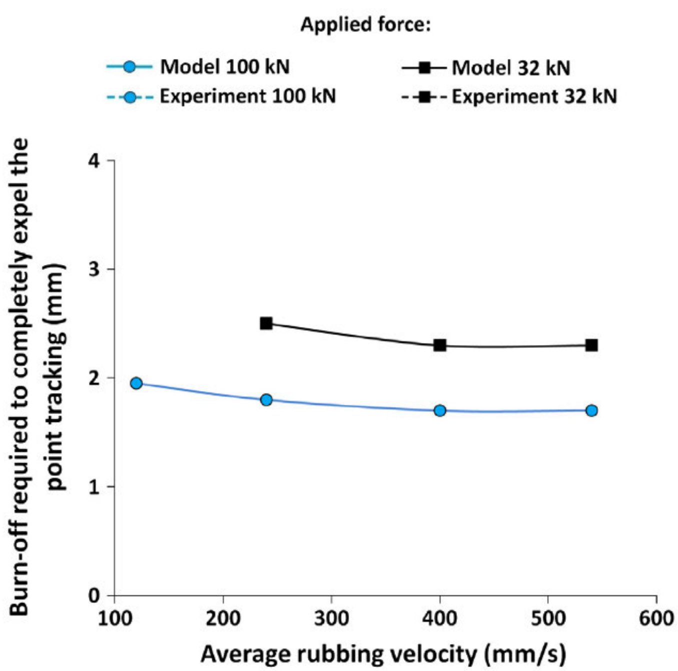

Figure 4.6. Combination of process inputs required to completely expel the point tracking into the flash [46].

While 2D models are computationally inexpensive and useful in determining trends, they do not fully capture the LFW process. Welds that are not rectangular cannot be modeled in 2D. This is especially true for the widest use of the technology:

welding blades to disks to form blisks. Furthermore, when the welds are rectangular, the flash that is extruded in the transverse direction to oscillation is neglected.

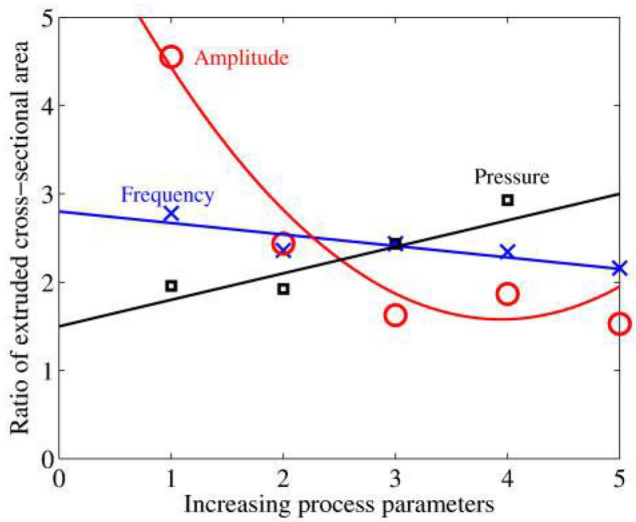

Figure 4.7. Data for ratio of flash extruded in oscillation direction to that extruded in direction normal to it, for various process parameters [62].

4.1.2 Three-Dimensional Models

In an effort to address the shortcomings of 2D models, Jun et al. [69] published a novel 3D study of the LFW process, modeling an oscillating Ti-6Al-4V workpiece against a non-deformable object using DEFORM. Temperature field and upset was modeled and compared against experimental results. Temperature data showed a 12% error and upset showed a 16% error. Material properties were defined as a function of temperature and a Coulomb friction model was utilized; determination of the coefficient of friction was not discussed.

Müller et al. [68] used ANSYS to model both workpieces as individual objects, accounting for the unequal upset between the workpieces. A variable sized mesh was used to capture the steep thermal gradient at the weld interface. Considerable effort was taken in defining the material properties of Ti-6Al-4V up to a temperature of 1250°C; dilatometry, differential scanning calorimetry, and the laser flash method were used to calculate thermal expansion, heat capacity, and thermal diffusivity as a function of temperature, respectively. The Coulomb coefficient of friction was determined using a combination of measurement and simulation; experiments and modeling converged on accurate interface temperatures so that the friction coefficient could be derived as a function of temperature.

Continuing Ceretti's work, Fratini and La Spisa [17] compared Ceretti's 2D DEFORM model with their 3D DEFORM model of the LFW of AISI 1045 steel. The 3D material model was equation based instead of tabular as in their previous work [13]. A tabular approach is generally more robust and reliable than empirically fitted equations for modeling a material's mechanical properties, while an equation based approach offers greater computational efficiency, which is desirable in a 3D model. Furthermore, the friction factor model as a function of temperature was refined to be non-linear, but still restricted to seven data points which were obtained from an unknown and undisclosed source. The true contact area was assumed to be saturated. This study showed that a 2D plain-strain model underestimates the upset because the material extruded in the transverse direction is neglected (Fig. 4.8). Realistic coupons are too short for adequate modeling, so while 3D models are more realistic, the computational power required is immense.

Wu [81] published findings from a simulation of the LFW of TC17 titanium alloy using ANSYS. Wu modeled two workpieces as individual objects and solved for stress and temperature fields. In order to model the frictional boundary condition, Wu defined 200 contact pairs at the interface, but did not describe the method used to

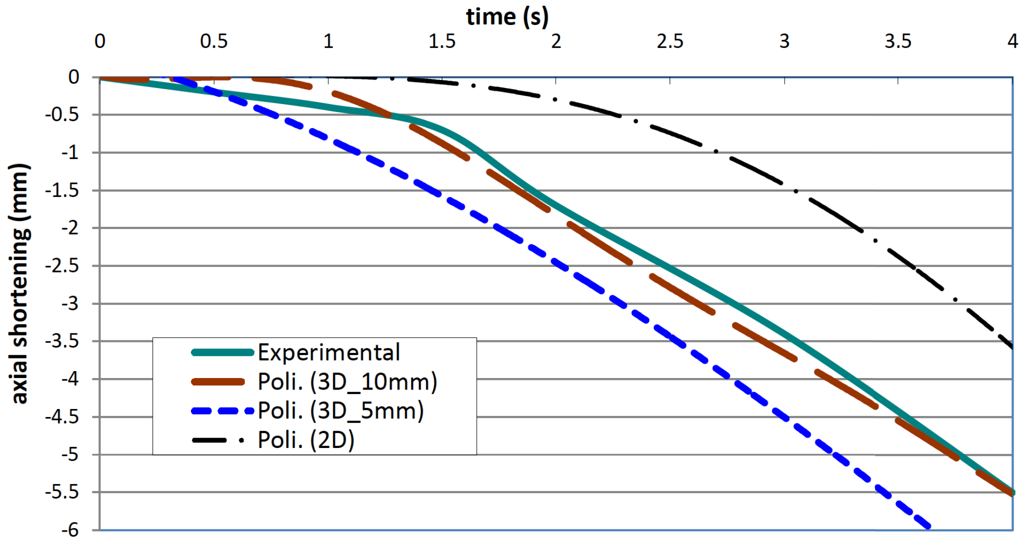

Figure 4.8. upset vs. process time for LFW with a coupon dimension of 10 mm (same as the experiment) and 5 mm transverse to the oscillation direction [17].

define the friction factor used in a Tresca friction model.

Fratini et al. [18] continued their modeling of LFW in 2012 with additional experimentation to validate modeling efforts. A material model similar to one from [17] was used as well as a similar friction factor defined as a function of temperature (within a Tresca friction model). Results from the study showed proper levels of pressure, frequency and temperature must be reached in order to obtain a quality weld. The authors note that these levels will be different for every material, and depend on thermal and mechanical properties.

Li et al. [39] investigated the effect of process parameters on the LFW of mild steel in ABAQUS. Due to computational expense, Li modeled only one plastic workpiece against a rigid non-deformable object. Frictional heat generation was accounted for through a Coulomb friction model with a temperature dependent coefficient of friction. Results from this study showed that an increase in frequency, amplitude, or pressure, while holding the other two constant, will increase the upset over the same amount of time. Li et al. [38] reflected on the challenges of numerically simulating LFW in both 2D and 3D, concluding that 3D simulations more accurately matched experiments and were able to capture more variables (flash characterization on all sides, residual stresses), but at six times the computational cost of 2D simulations.

Buffa et al. [10] investigated the determination of the shear coefficient in LFW of aluminum alloys. The aforementioned papers largely failed to describe the determination of shear coefficient (Tresca) or coefficient of friction (Coulomb), prompting Buffa et al. to detail a combined experimental and numerical investigation into the shear coefficient as a function of temperature for use in a 3D numerical LFW model. The friction factor was defined as the ratio of the applied shear stress to the material shear yield stress:

$$m = \frac{\tau}{\tau_0}. \tag{4.5}$$

The applied shear stress τ (the average welding force divided by the average contact area) was derived from dynamics equations. The material shear yield stress τ_0 is a function of temperature and strain rate; temperatures were obtained through thermocouple measurements and an iterative procedure in DEFORM was executed to converge on accurate strain rate values at the interface. Finally, an equation for friction factor m as a function of temperature was preposed for the aluminum alloy AA2011-T3.

Most recently, McAndrew et al. [47] shifted their Ti-6Al-4V modeling efforts from 2D To 3D, using experimental displacement histories as inputs into the 3D models instead of forces, as a way to reduce the large computational time and memory storage requirements. In their study, it was shown that when welding two rectangular workpieces together, oscillating in the shorter of the two directions reduced the size of the thermo-mechanically affected zone and reduced interface temperatures. Also, it was shown that lack of bonding in the corners of the workpieces can be resolved by increasing the upset distance. McAndrew et al. suggested that parametric studies of LFW be done in 2D, as 3D computational times remain unreasonably long.

4.2 Analytical Model

In FRW, friction is used to generate heat at the weld interface. Byerlee [11] illustrates a typical friction experiment (Fig. 4.9) where a mass is pulled and an elastic force builds until the mass begins to move relative to the ground. The mass then slips and does not regain traction until the spring compresses and the mass speed slows. This process repeats and is known as stick-slip. Stick-slip makes sense as a friction model for FRW. As the oscillating specimen begins to move from one end of the oscillation to the other, an elastic force builds before the specimen slips to the other end of the oscillation, when the process will start over. Until the materials plastically deform and begin to join, stick-slip will occur at the interface between the weld specimens. As temperature increases at the interface, material yield strength decreases. When the shear yield strength of the material is lower than the friction stress, the materials join together.

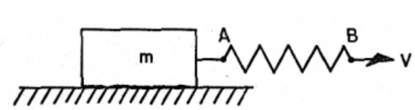

Figure 4.9. Diagram of typical friction experiment.

Maalekian [43] offers a differential equation modeling three dimensional heat conduction in a friction welding process:

$$\rho C_p \frac{\partial T}{\partial t} = \frac{\partial}{\partial x_i}\left(\frac{k \partial T}{\partial x_i}\right) + \rho C_p u \frac{\partial T}{\partial x_1} + \dot{S}, \tag{4.6}$$

where ρ is material density, C_p is the specific heat, k is the thermal conductivity, T is the temperature, t is time, x_i represents Cartesian directions ($i = 1,\ 2,\ 3$), u is the upset velocity of the material during friction welding and when multiplied by the temperature gradient, density, and specific heat gives a convective term accounting for the upset of the piece. $\dot{S}$ is the heat generation due to plastic deformation, which is defined as

$$\dot{S} = \alpha \overline{\sigma}\, \dot{\overline{\epsilon}} \tag{4.7}$$

where $\bar{\sigma}$ is the effective stress, $\dot{\bar{\epsilon}}$ is the effective strain rate, and α is the thermal efficiency of plastic deformation [19].

Equation (4.6) can be used to directly describe the linear friction welding process. Simplifying Eq. (4.6) by neglecting both the upset of the material as well as $\dot{S}$, and using only lumped parameters and time, one obtains a simple form of the heat equation:

$$\rho C_p \frac{\partial T}{\partial t} = 0. \tag{4.8}$$

Solving (4.8) with the initial condition $T(0) = T_0$ yields a solution for $T(t) = (kt)/(\rho C_p) + T_0$, as shown in Fig. 4.10.

4.2.1 One-Dimensional Analysis

Adding one spatial dimension to Eq. (4.8) yields:

$$\rho C_p \frac{\partial T}{\partial t} = k\left(\frac{\partial^2 T}{\partial x^2}\right) \tag{4.9}$$

Figure 4.11 depicts this situation.

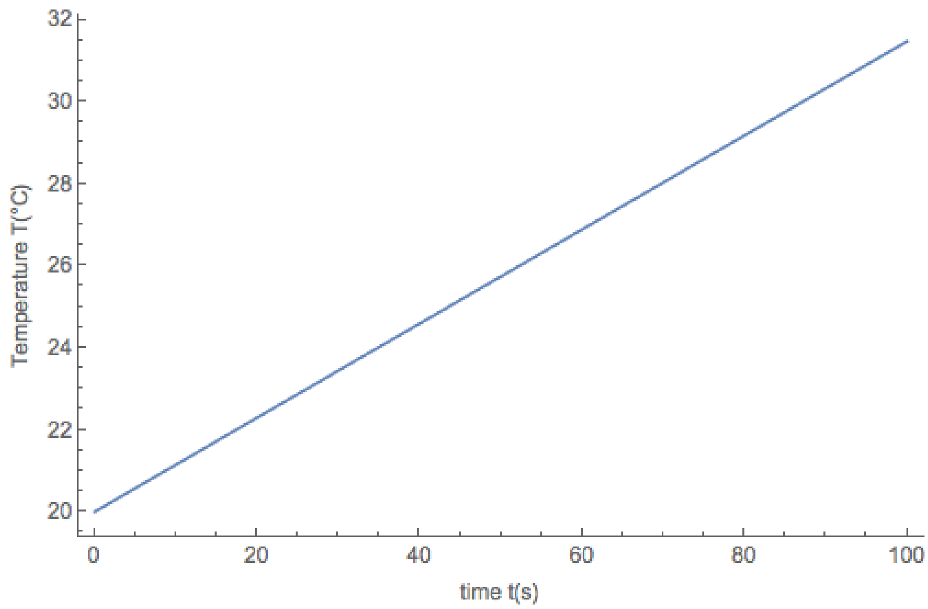

Figure 4.10. Solution to Eq. (4.8), with $T_0 = 100°\text{C}$

The appropriate boundary conditions for Eq. (4.9) are:

$$k \frac{\partial T}{\partial x}_{x=0} = -q_0 \tag{4.10}$$

$$T_{x=\infty,t} = T_0 \tag{4.11}$$

Equation (4.10) represents a flux of heat at $x = 0$. Equation (4.11) specifies a constant temperature T_0 at the infinite boundary. A starting temperature of T_0 at any point within the body is given by:

$$T_{x,t=0} = T_0. \tag{4.12}$$

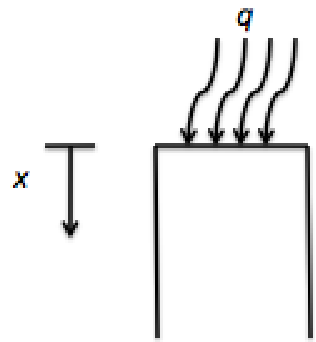

Figure 4.11. Free body diagram for LFW in one spatial dimension

The appropriate heat input q_0 is calculated using work-energy equations from friction:

$$q_0 = \mu N \Delta x. \tag{4.13}$$

where μ is the coefficient of friction, N is the normal force, and Δx is the total distance traveled throughout the friction welding process, and can be calculated from:

$$\Delta x = 4fat. \tag{4.14}$$

where f is the oscillation frequency, a is the amplitude of the oscillations, and t is the total amount of welding time.

The assumptions made are:

1. All other sources of heat transfer (convection, conduction, radiation), are ignored,
2. The upset velocity u is considered to be small compared to the sliding velocity,
3. The the heat generation due to plastic deformation, $\dot{S}$, is ignored,
4. A constant friction coefficient μ,
5. A constant heat flux q,
6. A constant contact area between surfaces,
7. A constant thermal conductivity k,
8. A constant normal force N.

In order to solve the problem analytically, the upset velocity must be neglected. This is an appropriate assumption throughout the first two phases of LFW, before any Upset begins. Without upset, there is no heat generation due to plastic deformation, so it can be neglected as well. In reality, the friction coefficient is a function of six variables [82], some of which are not fully orthogonal:

1. The relative speed between the specimens,
2. The temperature of the friction surfaces,
3. The nature of the material,
4. The presence of surface films,
5. The normal surface pressure,
6. The rigidity of the friction surface.

Without detailed knowledge of friction coefficient, it will be assumed as constant. During one period of oscillation, the heat flux varies depending on the relative speed between the two specimens. In the analytical model, the heat flux is averaged over all of the oscillations. Because almost no surface is truly flat, there is a question of how much *real* contact there is between two surfaces undergoing friction. Persson [53] says that this contact area determines the contact resistivity and the heat transfer between the solids. The result is a prediction that contact area increases linearly with applied force, consistent with the model of Greenwood and Williamson [22]. In order to truly predict the heat transfer between the solids, a model for contact area should be developed. For the sake of simplicity in these calculations, the assumption of perfectly flat surfaces will lead to the assumption of constant contact surface area. Thermal conductivity variation is expected, but cannot be accounted for in the analytical model and will be taken as constant. A friction welding process generally has multiple stages all with different levels of force, but in order to get a good approximation for q, a constant value will be assumed. These constraints will be relaxed in the numerical model presented in Section 4.3.

Carslaw and Jaeger [12] give a solution to this problem for temperature as a function of space, x, and time, t:

$$T(x,t) = \frac{2q}{k}\left[\left(\frac{\alpha t}{\pi}\right)^{\frac{1}{2}} e^{-x^2/4\alpha t} - \frac{x}{2}\mathrm{erfc}\frac{x}{2\sqrt{\alpha t}}\right]. \tag{4.15}$$

where q is defined in Eq. (4.8), and α is the thermal diffusivity $\alpha = \frac{k}{\rho c_p}$. Substituting appropriate material parameters, a solution for $T(x,t)$ is obtained with an initial temperature $T_0 = 25°\mathrm{C}$ (Fig. 4.12).

4.3 Development of the Numerical Model

As described in Section 4.1, there are currently three different approaches for modeling LFW:

1. Model the two workpieces as individual objects.
2. Model one workpiece oscillating against a non-deformable object.
3. Model a single body representing two workpieces.

For this thesis, a combination of the first and third types were used in a method similar to that of previous studies [45, 46, 62, 63, 70, 71]. In those studies, the initial phase of LFW was modeled thermally with a heat flux at the interface between the two individually modeled workpieces. After the workpiece surfaces reached temperatures hot enough for deformation, the temperatures from the initial phase of LFW are transferred from the two individual objects onto a single object occupying the same geometric space as the previously separate workpieces. At this point the single workpiece is a plastic object, capable of changes in both shape and temperature. The modeling approach in this thesis follows that of the aformentioned studies, however, instead of using a purely thermal model to capture temperature rise during the initial phase of LFW, a coupled thermo-mechanical model was used in combination with a novel friction user routine to calculate the friction coefficient along the boundary

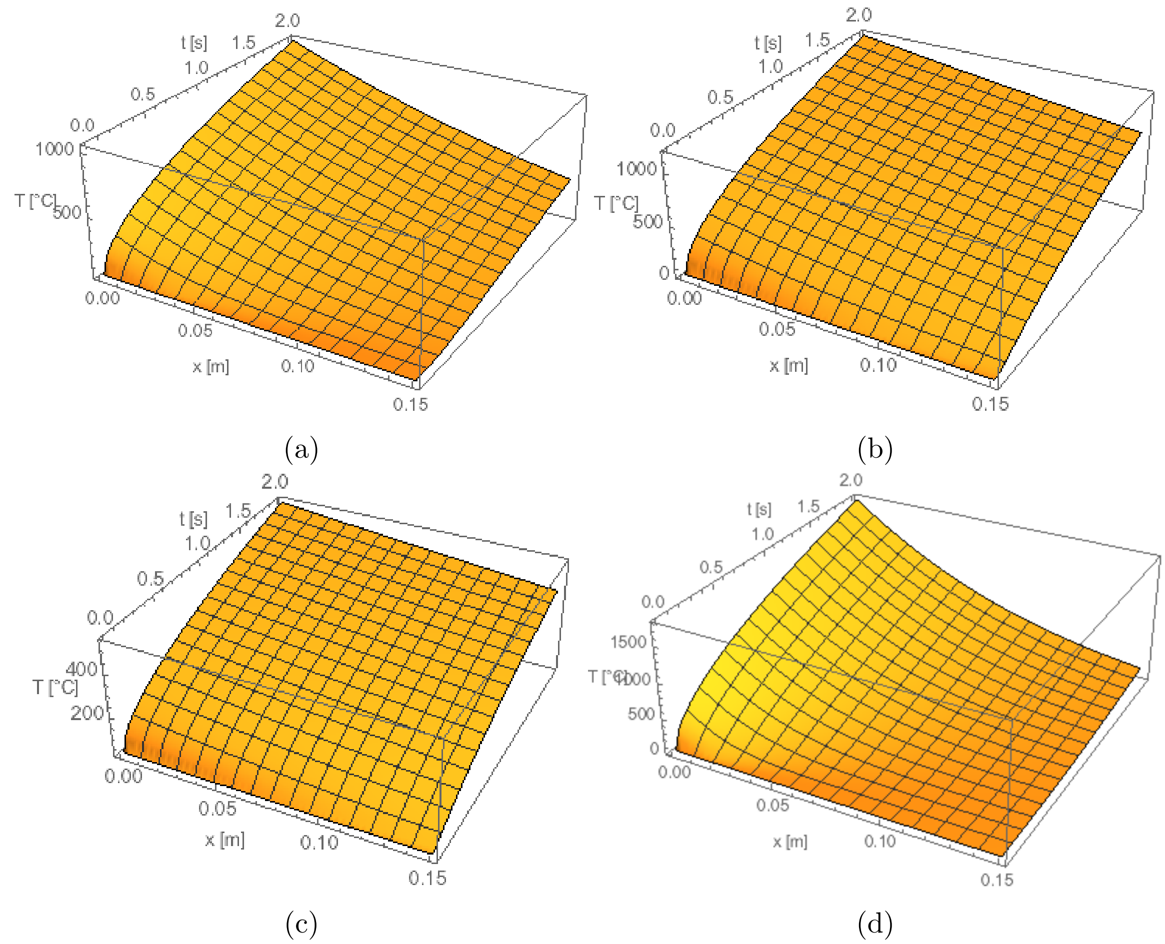

Figure 4.12. Specimen temperature as a function of x and t only for (a) Steel (b) Aluminum (c) Copper and (d) Titanium. $T_0 = 25°\text{C}$

between the two workpieces.

While the modeling approach may be similar to past studies, it is important to recognize the differences. First and foremost, the material used in the majority of LFW modeling publications is Ti-6Al-4V; for this thesis, it is AISI 1020 steel. Ti-64 is seven to eight times less conductive than 1020 steel, and two times stronger, meaning that frictional heating will be more concentrated at the surface, and deformation more localized. With 1020 steel, the frictional heating should spread further into the workpiece, and deformations (both elastic and plastic) should be less localized. Furthermore, in this thesis, IH is used to preheat the parts so that less mechanical energy is required from the LFW machine. This further increases the depth of heating and leads to lower yield strengths throughout the hot regions of the workpiece. As discussed in the previous chapter, the induction heating was not uniform on the surface of the workpiece, so different areas of the weld joint will begin to yield before others. Knowing these differences is important to understanding both the modeling and experimental data.

4.3.1 Geometry

Figure 4.13 shows the 2D model geometry in DEFORM. There are four different objects: a top and bottom die, and a top and bottom workpiece. Each workpiece was modeled to be 101.6 mm wide and 101.6 mm in height. In the experiments, the workpiece geometry was 101.6 mm wide and 152.4 mm in height, however in the interest of reducing the complexity of the model, the height of the workpieces was shortened; this strategy has been implemented by many of the research groups referenced in Table 4.1. Additionally, the height of the workpieces in the LFW model had to match that of the IH model in order to interpolate temperature data from the IH mesh onto the LFW mesh for the initial condition. The two dies were modeled to provide physical and thermal boundary conditions for the two workpieces.

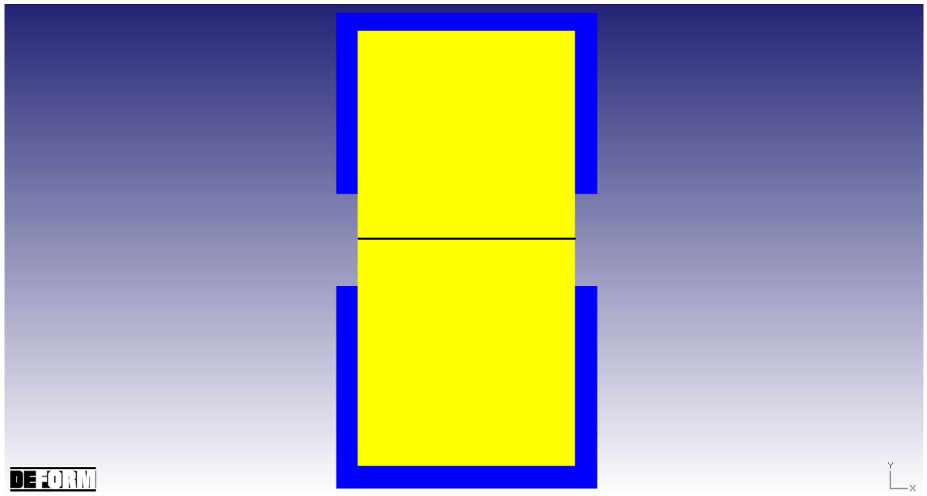

Figure 4.13. Model geometry for the LFW numerical model.

4.3.2 Mesh Generation

As in Section 3.3.2, identical meshes with tetrahedral elements were generated for the top and bottom workpieces using mesh density windows (Fig. 4.14). A window for smaller elements near the weld surface extended 2.54 mm into the workpiece for elements 0.25 mm in width. A second window for slightly larger elements was defined for elements 1.25 mm in width that extend 10 mm into the workpiece. A third window was defined for elements 3.8 mm in width that extended 25.4 mm into the workpiece, and a final window was defined for elements 5 mm in width that extended the remainder of the workpiece depth. The mesh windows were then coupled to the movement of the workpieces so that as one workpiece oscillates and the other upsets, the mesh windows associated with those workpieces follow.

For the simulation of weld number 16 from the DOE, the top and bottom workpieces in total were comprised of 7903 nodes and 8393 tetrahedral elements. The minimum element size of 0.25 mm at the weld surfaced is consistent with the work of [45, 46] using the same FEA software in DEFORM. It has also been proven small enough to accurately capture the steep thermal and strain gradients near the work-

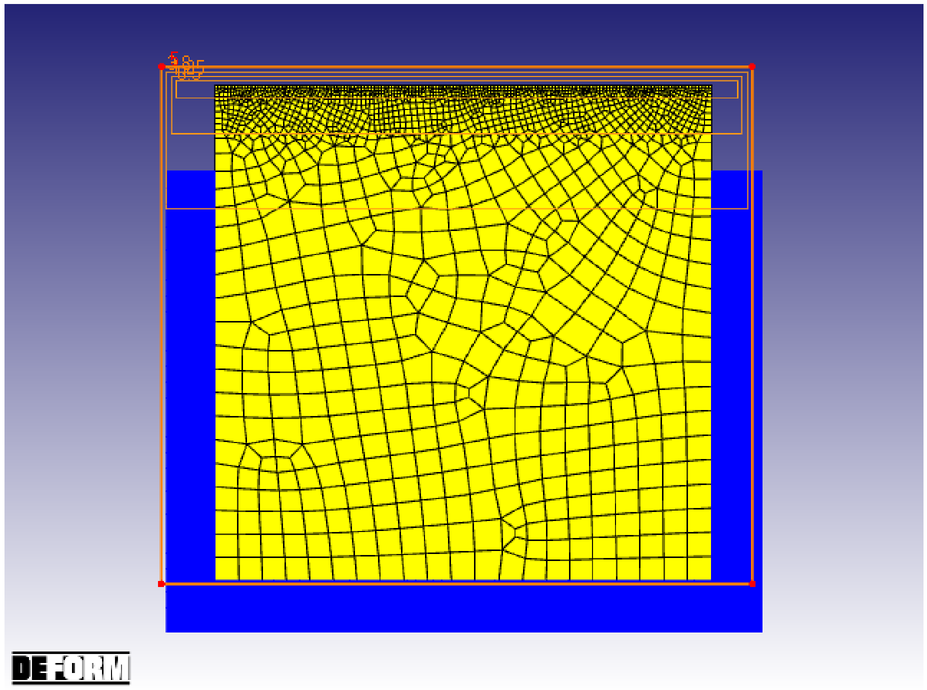

Figure 4.14. Mesh windows for the LFW numerical model.

pieces surfaces. The top and bottom dies were modeled as rigid entities and therefore were not meshed, however they were assigned thermal material properties in order thermally interact with the workpieces.

4.3.3 Material Properties

In DEFORM, there are two different methods to account for a material's plastic constitutive data: the tabular method, and the equation based method. In LFW modeling, groups have utilized both the former [10, 13, 32, 45–47, 62, 63, 67, 68, 70, 71, 73, 83], and to a lesser extent the latter [17, 18, 25, 35–40, 67]. In the tabular approach, discrete flow stress values are recorded for different values of temperature, strain, and strain rate, and are interpolated within the available data region. As long as extrapolation outside the data region is not necessary, the tabular format is robust and reliable. However, equation based models are computationally more efficient, making them particularly useful for complex 3D LFW models [17, 18].

In this thesis for the 2D model, the tabular method was utilized. The flow stress data for AISI 1020 steel was supplied by DEFORM and defined for temperatures up to 1370°C, strain rates up to 40 s^{-1}, and strains as high as 0.8 mm/mm. Because temperatures never exceeded 1100°C in the experiments, extrapolation outside of the temperature range of the data was not necessary. Figure 4.15 shows plasticity data for four of the nine temperatures given in DEFORM. The thermal material properties of the material were described in Section 3.3.4, and included data for thermal conductivity (Fig. 3.14), volumetric heat capacity (Fig. 3.15), emissivity, and mass density. The interface heat coefficient specifies the coefficient of heat transfer between the two object in contact, and was set to 11 N/(sec-mm-°C) as recommended by DEFORM.

In order to help convergence, the limiting strain rate (LSR) is used in DEFORM to identify rigid regions of the part, and to calculate flow stress in regions with near zero deformation rates. At values below the LSR, the flow stress-stain rate relationship is assumed to be linear between 0 and the value of the flow stress at the LSR. The LSR is a fixed ratio of the average strain rate, and is typically 100:1. In the LFW simulation, the average strain rate was 1 s^{-1} and the limiting strain rate was set to 0.01 s^{-1}. If the LSR is too small, the solution may have difficulty converging, but if the LSR is too high, the accuracy of the solution will be degraded. The volume penalty constant specifies a large positive value that is used to enforce volume constancy of plastic objects, and was set to 10^6. A penalty constant that is too small can result in high volume losses, and a penalty constant too large can make it difficult for a solution to converge [64].

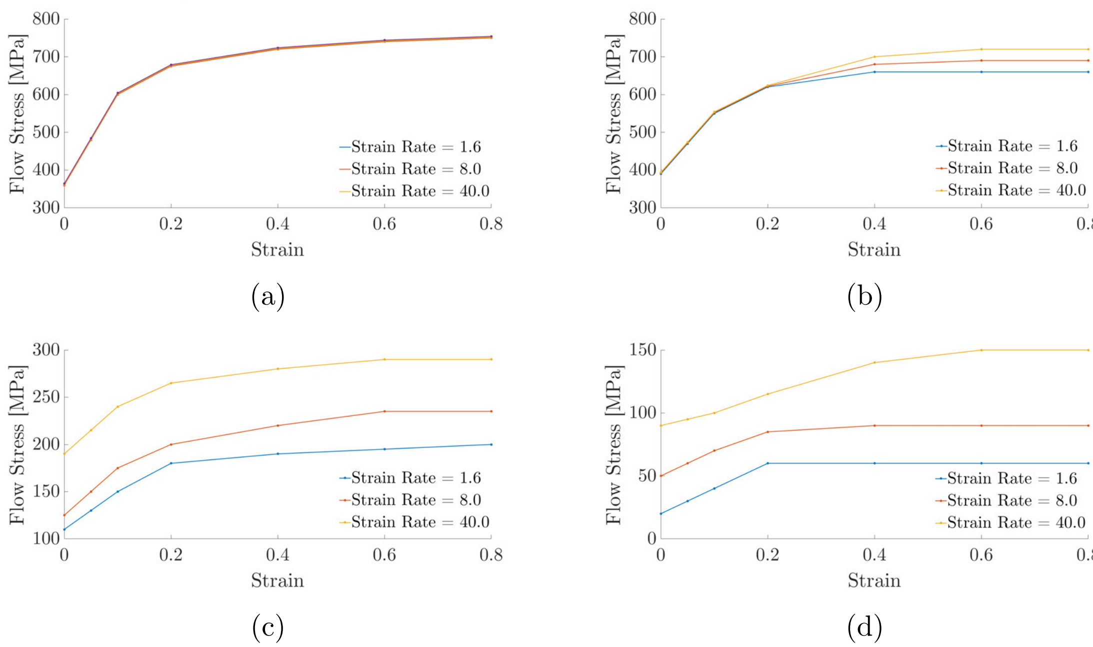

Figure 4.15. Constitutive data of AISI 1020 steel for the 2D LFW numerical model. (a) Temperature = 20°C (b) Temperature = 400°C (c) Temperature = 800°C (d) Temperature = 1200°C

4.3.4 Modeling Parameters

In DEFORM, temperature data can be interpolated from one mesh onto another as long as the geometries are the same. Therefore, the temperature data from the final step of the IH numerical model was copied and interpolated onto the LFW numerical model for the two different preheat levels. In Chapter 3, the simulation finishes with an induction coil remaining in between the two workpieces. Figure 4.16 shows the initial thermal condition for the LFW model, after the coil has retracted and the workpieces are brought into weld position.

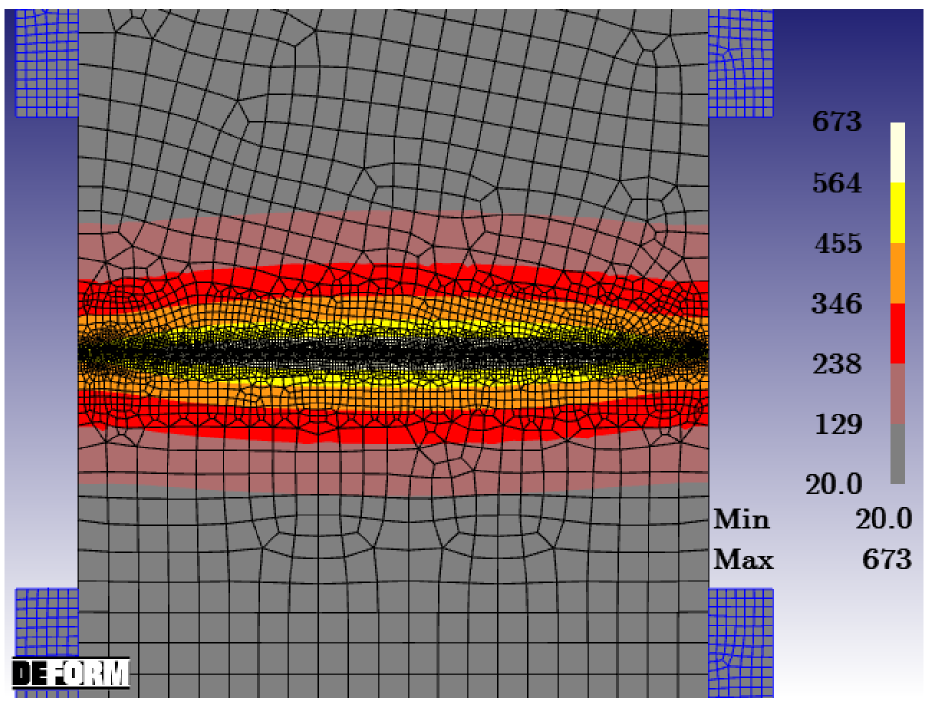

Figure 4.16. Initial condition for the LFW phase of weld number 16.

Weld numbers 14 and 16 were modeled because they represented both the high

(850 °C) and low (650 °C) extremes of preheat temperature. In addition, for the four welds in which temperature was measured, welds 14 and 16 had the most accurate looking thermocouple data of the high and low preheat levels. Temperature and upset distance were the intended methods for correlating the experiment to the model.

The thermal boundary conditions specified 100% contact between the dies and the workpieces with an interface heat coefficient of 11 N/(sec-mm-°C), heat exchange with the environment at a temperature of 20°C and a convection coefficient of 0.02 N/(sec-mm-°C).

Weld number 14 used a 30 Hz oscillation frequency, 2 mm oscillation amplitude, 100 MPa weld pressure, and 2.5 mm upset distance (high preheat temperature). Weld number 16 was carried out with 30 Hz oscillation frequency, 2 mm oscillation amplitude, 40 MPa weld pressure, and 2.5 mm upset distance (low preheat temperature). As in the experiment, the ramp time for both the oscillation amplitude and the weld pressure was 0.2 seconds. Figure 4.17 shows oscillation frequency vs. time for both the high and low settings of the experiment, and represent the path followed by the lower die in the LFW simulation of the initial phase. Figure 4.18 shows weld pressure vs. time for both the high and low settings of the experiment, and are indicative of the downward pressure generated by the top die in the LFW simulation of the initial phase.

Several research groups have shown that modeling the latter stages of LFW with a single workpiece representing two individually joined workpieces results in a better prediction of flash morphology and a closer approximation of upset distance vs. time ([45, 46, 62, 63, 70, 71]. Therefore, as the interfacing nodes reach temperatures at which the parts have shown to deform in the associated experiments, the temperature, stress, and strain data for the nodes and elements will be mapped onto a single workpiece, and the simulation will continue. This will separate the initial phase of the LFW model from the latter phases.

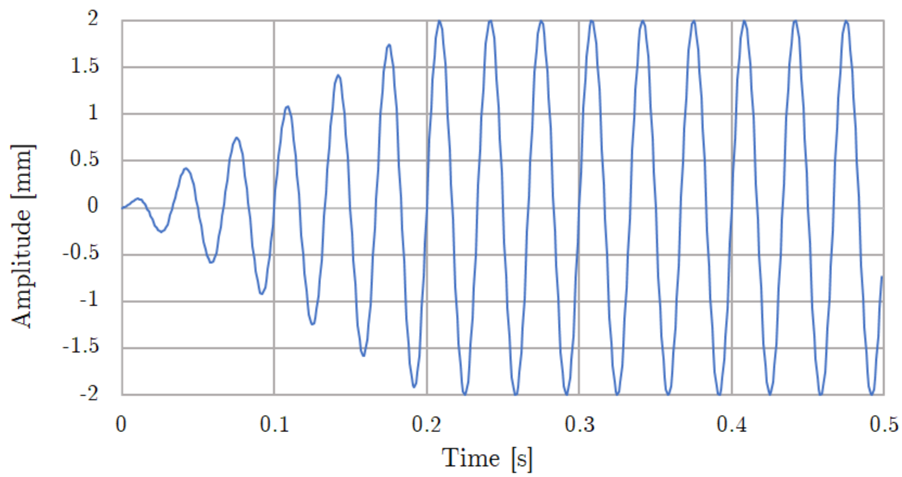

(a)

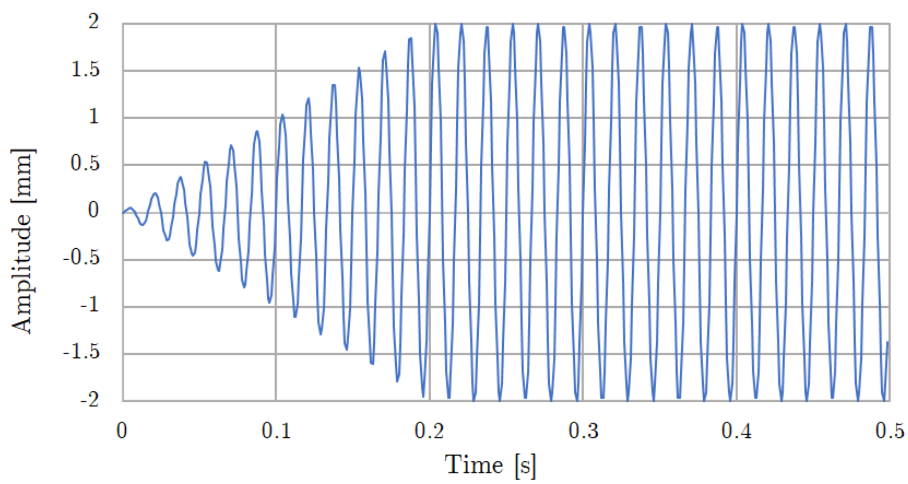

(b)

Figure 4.17. Oscillation path during the initial phase of LFW for the (a) low frequency setting and (b) high frequency setting.

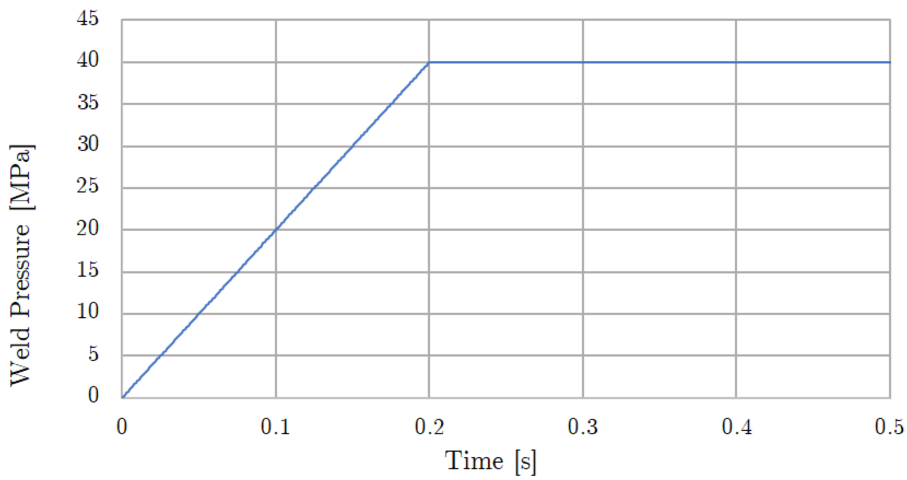

(a)

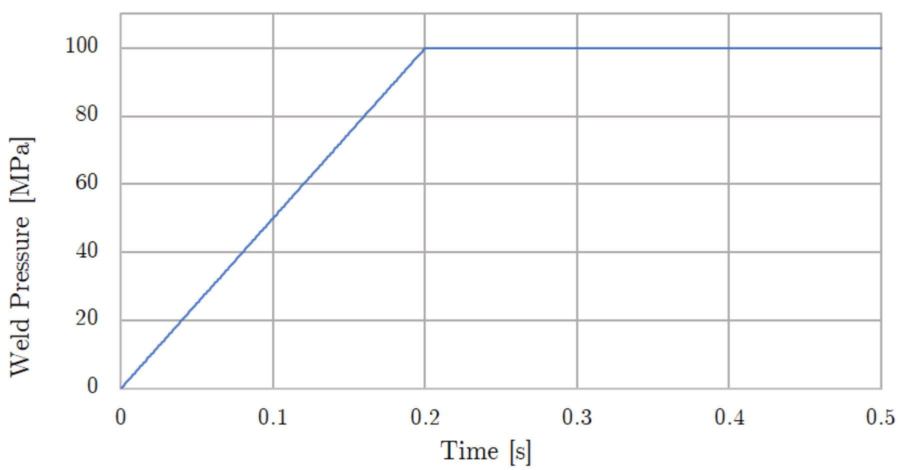

(b)

Figure 4.18. Weld pressure vs. time for the initial phase of the LFW numerical model. (a) Pressure = 40 MPa. (b) 100MPa.

In DEFORM, a Lagrangian framework is recommended for all conventional forming and heat transfer applications [64]. Therefore, a Lagrangian incremental simulation was chosen assuming plane strain conditions. A Multifrontal Massively Parallel sparse direct Solver (MUMPS) was used to calculate both deformations and temperatures. This type of solver can solve large systems of equations on distributed memory parallel computers, reducing computation time.

DEFORM recommends that the maximum displacement for any node does not exceed about 1/3 the length of its element edge [64]. This prevents the mesh from becoming overly distorted from step to step. Using the high and low values for oscillation frequency from the DOE matrix, it is possible to calculate the maximum velocity of the oscillating workpiece as it passes through the zero position of the sine wave. The maximum velocity of a workpiece oscillating at 30 Hz and an amplitude of 2 mm is 377 mm/s, and the maximum velocity for a workpiece oscillating at 60 Hz frequency and 2 mm amplitude is 754 mm/s. Therefore, the step increment was strategically set at 0.0001 seconds per step so that a node will at most travel 0.075 mm in a single step (assuming a peak velocity of 754 mm/s), just less than 1/3 the length of the smallest element edge of 0.25 mm. The interface penalty constant was 10^9, a high number used to penalize the penetration velocity of a node through a master surface (this should be two to three orders higher than the volume penalty constant). The Boltzmann radiation constant was 5.67×10^{-8} W/(m^2-K^4) for radiation heat transfer calculations. When slave nodes touch and separate from the master surface, it was chosen that after three cycles, the nodes are made to touch for the sub step.

4.3.5 Friction User Routine

The majority of the LFW models referenced in Table 4.1 are very similar, but one of the biggest differences (within 2D and 3D models) is the way friction is modeled. In DEFORM, and likely other FEA software packages, the friction coefficient can be specified as a function of time, temperature, pressure, pressure temperature surface stretch, pressure dependent, strain rate, and sliding velocity. The friction types allowed are Coulomb, Tresca, and hybrid (combination of Tresca and Coulomb).

Figure 4.19a depicts Coulomb, or, sliding friction where the friction stress is defined by the relationship

$$f_s = \mu p. \tag{4.16}$$

where f_s is the frictional stress, μ is the friction coefficient, and p is the interface pressure between the two components. Unfortunately, the linear relationship between frictional stress and interface pressure is not valid at interface pressures that exceed the yield strength of the material. For Tresca, or sticking friction, the friction stress is given by

$$f_s = mk, \tag{4.17}$$

where m is the friction factor and k is the shear yield strength (Fig. 4.19b). In the hybrid model, the user can use both the Coulomb and Tresca friction types to quantify friction stress as a function of pressure; the Coulomb type is used until the friction stress reaches the shear strength of the material, and the Tresca type is used thereafter (Fig. 4.19c). Typically in DEFORM, Coulomb friction is used for sheet metal forming operations and Tresca friction is used for bulk-forming simulations. However, sheet forming is highly non-linear, so neither friction model truly works well.

Numerous tribological mechanisms contribute to the LFW process:

1. Plastic deformation of the workpieces results in asperity softening and a rapid increase in true contact area,

2. Deflection of the surface layers removes oxides and contaminants from the weld zone

3. Nascent oxide-free material from the substrate is brought into the contact zone, producing a strong weld without melting.

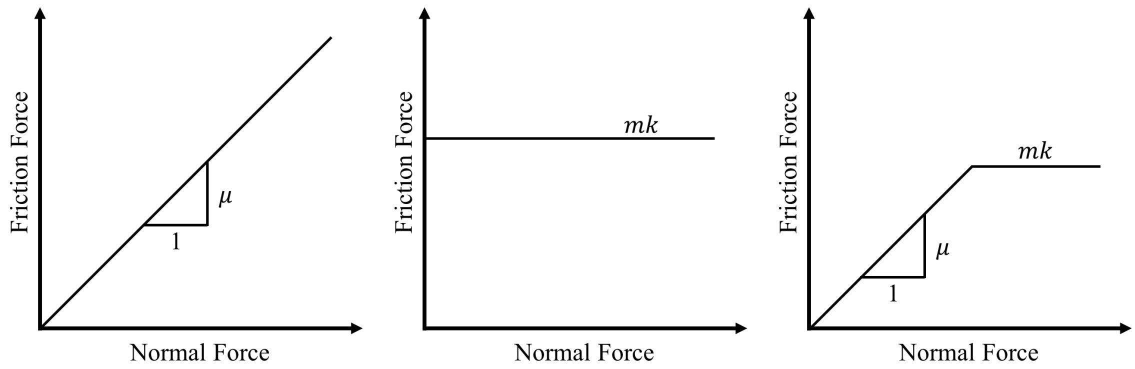

(a) (b) (c)

Figure 4.19. Various popular friction models. (a) Coulomb friction, (b) Tresca friction, (c) Hybrid Coulomb and Tresca

From a modeling standpoint, as friction transitions from Coulomb to Tresca behavior, the friction stress becomes larger as the substrate is exposed. The initial phase of LFW, as described by Vairis and Frost [73], is associated with Coulomb friction and heating at asperities that are remote from each other. Plastic deformation localized in the frictionally heated layers causes the softened layers to deform laterally in the equilibrium phase, at which point the model will transition from the Coulomb to the Tresca model of friction, and eventually to sticking friction where the two workpieces can be modeled as a single workpiece.

Previous LFW modeling studies have used both the Coulomb and the Tresca friction type, and typically, the coefficients or factors are experimentally measured as a function of time, temperature, and or pressure, and subsequently input as data into a simulation. In those approaches, friction force is quantified by lumping together all of the interface phenomena into a single friction coefficient or factor. These models do not take into account many of the tribological mechanisms in metal forming and LFW.

Orowan [52] was the first to develop improved friction models for metal forming, suggesting that friction stress increases with pressure for a constant coefficient of friction up until the critical pressure where the apparent area of contact is equal to the real area of contact, and the friction stress is constant. This is much like the hybrid Coulomb and Tresca model of friction shown in Figure 4.19c. Shaw et al. [65] and Wanheim and Bay [75] suggested that there be a more gradual transition from the Coulomb friction model to the Tresca friction model, as depicted in Figure 4.20.

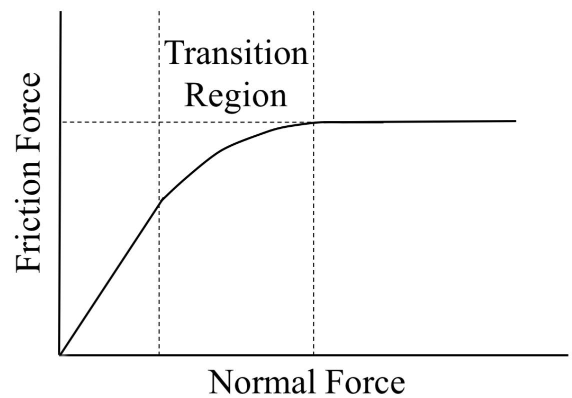

Figure 4.20. Hybrid Coulomb and Tresca model with a gradual transition between the two.

Saha and Wilson [59] have shown that a smooth transition can occur due to a phenomenon known as asperity flattening. Two surfaces can appear to be in contact, but are not truly in 100% real contact; microscopic asperities on the surfaces of the two workpieces make real contact with each other, and this real contact area changes as asperities flatten. In order to develop an appropriate boundary friction model for LFW, the effects of asperity flattening must be accounted for; the friction factor for regions in true contact is different from the friction factor for regions separated by pockets of lubrication, or, in the case of LFW, air.

Wilson and Sheu [78] used the upper bound method to model the flattening of asperities in the plane strain condition. They defined the fractional contact area A as the ratio of the real area of contact to the apparent area of contact, and obtained the following relationship between fractional contact area, A, and strain, ϵ:

$$\frac{dA}{d\left(\epsilon/\theta\right)} = \frac{Pf_1}{2A - Pf_2}. \tag{4.18}$$

P is the non-dimensional interface pressure given by

$$P = \frac{p}{k}, \tag{4.19}$$

where p is the interface pressure and k is the material shear yield strength. θ is the initial asperity slope, and the functions f_1 and f_2 are given by

$$f_1 = 0.515 + 0.345A - 0.86A^2, \tag{4.20}$$

and

$$f_2 = \frac{1}{2.571 - A - A\ln\left(1 - A\right)}, \tag{4.21}$$

respectively. The relationship given by Wilson and Sheu was verified by experimental measurements in rolling. Note that Equation 4.18 can predict an increase or decrease in fractional contact area based on the current values of fractional contact area and non-dimensional pressure. Done carefully, this model of fractional contact area can be incorporated into an FEM analysis with discrete time stepping to solve for an average friction factor m_{avg}, given by

$$m_{\text{avg}} = m_a A + m_o\left(1 - A\right), \tag{4.22}$$

where m_a is the friction factor of the asperities, and m_o is the friction factor of the oxides surrounding the asperities in contact.

In DEFORM, user routines are written and compiled in Fortran, and are called at each step to make calculations. Because friction boundary conditions are calculated and applied at nodes, the fractional contact area state variable must be tracked node by node. To calculate fractional contact area in DEFORM using equation 4.18, pressure, flow stress, and a strain increment must be known. Because DEFORM is using time discretization, the strain increment at a given time step is simply the strain rate at that step multiplied by the time increment. Therefore, to calculate the average friction factor m_{avg}, pressure, strain rate, and flow stress (elemental effective stress) must be known for each node. Unfortunately, strain rate and flow stress are calculated at element centroids in DEFORM, and contact pressure is not passed down to user subroutines for rigid-plastic objects.

The contact pressure is calculated on element faces, but needs to be quantified at each node. Therefore, in a user subroutine, the resultant node force vector was used to calculate the elemental area associated with each node (half of the area of each adjoining element face). Then, the normal of each element face is calculated and averaged to get an average unit normal at each node. Taking the dot product of this normal and the force vector results in a component of force along the normal. This normal force can then be divided by the elemental area associated with each node to get a pressure at each node.

For flow stress and strain rate, it is necessary to lump both of these values to the appropriate boundary nodes in order to do the calculations of fractional contact area, and eventually friction factor. In DEFORM, the tetrahedral elements are defined by the four nodes that make up their corners. For the friction user routine, the nodes must conversely be defined by the four elements that attach it. Therefore, a reverse mapping of the nodes to the elements associated with each node must be executed.

This is computationally expensive, so a data flag is used to do this mapping only the first time USR_MSH is called after each re-meshing step. After the reverse mapping is complete, and each node is defined by the elements surrounding it, the associated stress and strain rate values for each node can be calculated. The stress and strain rate variables associated with each element that is attached to a given node is added up, and then divided by the number of elements on that node to get the average stress and strain rate at that node.

The definition of pressure, strain rate, and flow stress (elemental effective stress) at each node as described above was all executed in the user subroutine USR_MSH.f, which can be viewed in Appendix A and was written with the assistance of DEFORM technical specialists so that the fortran code could interface with the elemental and nodal variable names. Another user subroutine, USR_BCC.f, was written to calculate the friction factor (Eq. 4.22) from the fractional contact area increment calculated in the user subroutine USR_MSH.f.

4.3.5.1 Simple Test Case

A simple test case for the friction user routine was setup in DEFORM, simulating a rigid die in contact with a deformable workpiece, with the die traveling downwards at 1 mm/s. The initial fractional contact area was defined to be 0.333, the friction factor of the asperities was chosen to be 0.9, the friction factor of the oxides was set to 0.4, and the initial asperity slope was set to 10°. Looking at the simulation results, as the die moves downwards and the part deforms, the fractional contact area A, increases (Fig. 4.21), along with the average friction factor m_{avg}.

This makes sense based upon the mathematical evolution of those variables with increasing strain. The simple test case demonstrated that the user routines function with a simplified geometry and simplified die movement, and were grounds to continue with a complete LFW simulation using the two user subroutines.

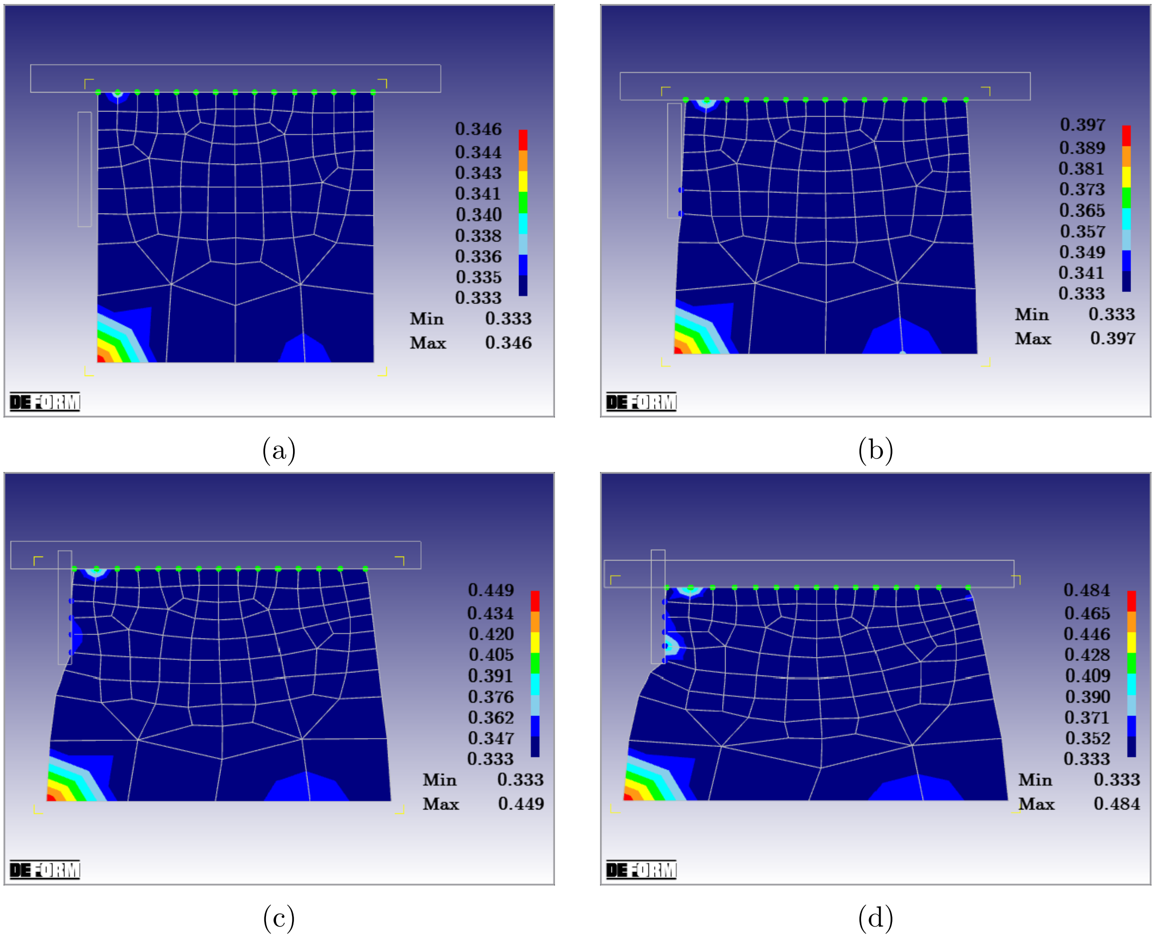

Figure 4.21. Screen captures in DEFORM showing the fractional contact area, A, from a simplified test case of the friction user routine after (a) 1 second, (b) 7 seconds, (c) 15 seconds, and (d) 22 seconds

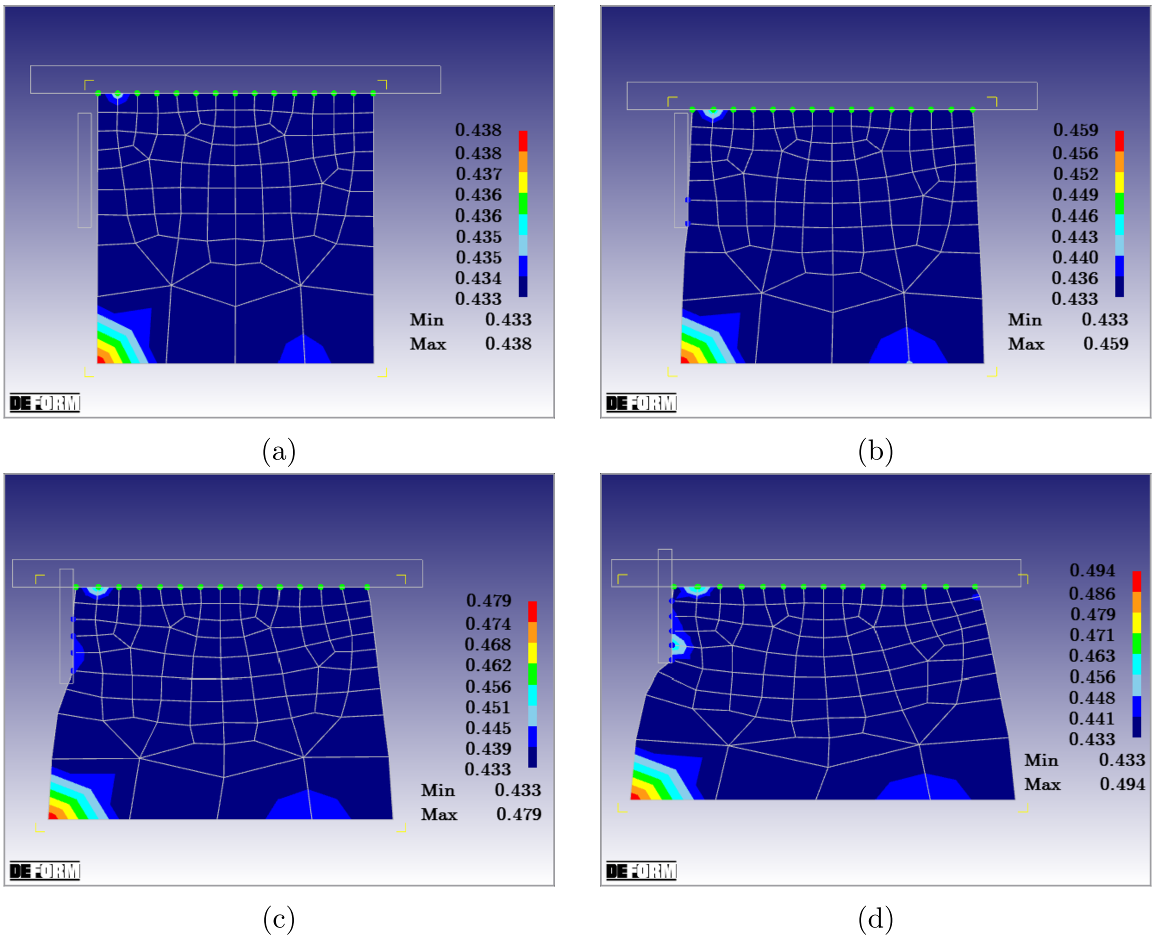

Figure 4.22. Screen captures in DEFORM of the average friction factor, m_{avg}, from a simplified test run of the friction user routine after (a) 1 second, (b) 7 seconds, (c) 15 seconds, and (d) 22 seconds

4.4 Results and Discussion

4.4.1 Initial Phase of LFW numerical model

Prior to using the friction user routine in the full LFW simulation, a test simulation for weld 16 was run with the above parameters for a constant friction coefficient at the interface between the two workpieces. In this simulation, there was a gradual loss of contact between the two workpieces that resulted in under-predictions of temperature. Figure 4.23 illustrates the issue of contact loss during the initial phase of the LFW simulation.

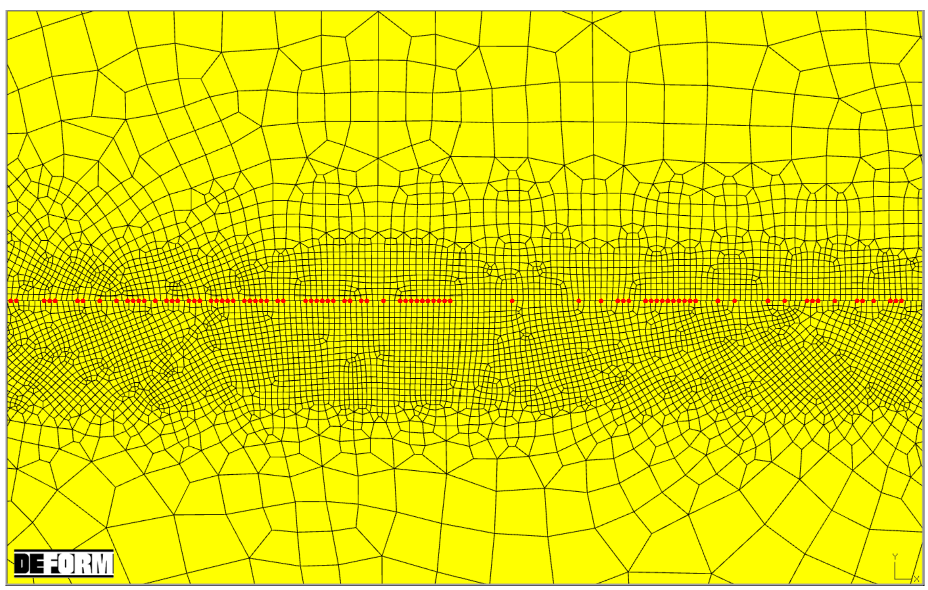

Figure 4.23. Screen capture of the repeating contact loss issue. The red dots represent contact between the master surface and the slave nodes.

Many changes were made to the modeling parameters in an attempt to resolve the issue and maintain contact between the master (top, forging) and slave (bottom, oscillating) workpieces: The time step was reduced so that the maximum displacement for any node did not exceed 1/6 the length of its element edge. The limiting strain rate was increased to 0.001 s^{-1} to assist with convergence. The volume penalty constant was lowered as well as the interface penalty constant to try to assist with convergence. The friction coefficient was increased. A friction factor was used, and varied between 0 and 1. The default separation criteria for a node is that a contacting node will separate when it experiences a tensile force or pressure greater than 0.1. In order to make it harder for nodes to separate, the separation criteria was changed so the the nodes would separate when the tension on the contact node was greater than 50% of the flow stress of the slave object. Regardless of the changes made to the modeling parameters, the contact loss issue persisted.

Correspondence was made with a research group (McAndrew et. al) in the United Kingdom that has used DEFORM extensively to model LFW [45–47] of Ti-6Al-4V. When questioned, they reported similar issues of contact loss when attempting to model the initial phase of LFW. Unable to resolve the issue of contact loss between the workpieces, McAndrew et al. resorted to modeling the initial phase of LFW purely thermally, with a heat flux boundary condition on the weld surface. In order to account for the oscillations, the heat flux was reduced to 1/2 of its value at the edges of the workpiece, beginning to reduce at a distance of 1 amplitude away from the edge. After the workpieces reached the Ti-6Al-4V beta-transus temperature, the thermal model was stopped and the temperature data was transferred from the two separate workpieces onto a single deformable workpiece for the remainder of the simulation. During that secondary phase of the simulation, it is assumed that the parts are already joined together, and therefore exhibit no frictional behavior outside of sticking friction, or, a Tresca friction model with a friction factor of 1.

Intiially, this semi-empiricism was unsatisfying and one of the driving reasons for the development of the friction user routine in this thesis. However, after communicating with McAdrew et al., it was clear why a semi-empirical model for the initial phase of LFW was used. It became evident after years of testing that the technology in DEFORM is not yet able to resolve frictional contact between two separate and deformable workpieces oscillating at high frequencies and under high pressures. However, the friction user subroutines were still developed and proven to be functional, and will hopefully interface with a future release of DEFORM, or another software, to use in an LFW model.

A purely thermal model for the initial phase of LFW was created, akin to that of McAndrew et al. [45–47]. However, instead of predicting the heat flux at the surface of the two workpieces, it was experimentally recorded during the weld and used as input data for the experiment. The process power was recorded during the weld and was scaled by the 25.4 mm width of the workpieces to generate a heat flux boundary condition on the weld interface. This curve for weld 16 can be seen in Figure 4.24. As done by McAndrew et al. [45, 46] the heat flux was linearly reduced to 1/2 its value, beginning at 1 amplitude away from the edges of the workpieces.

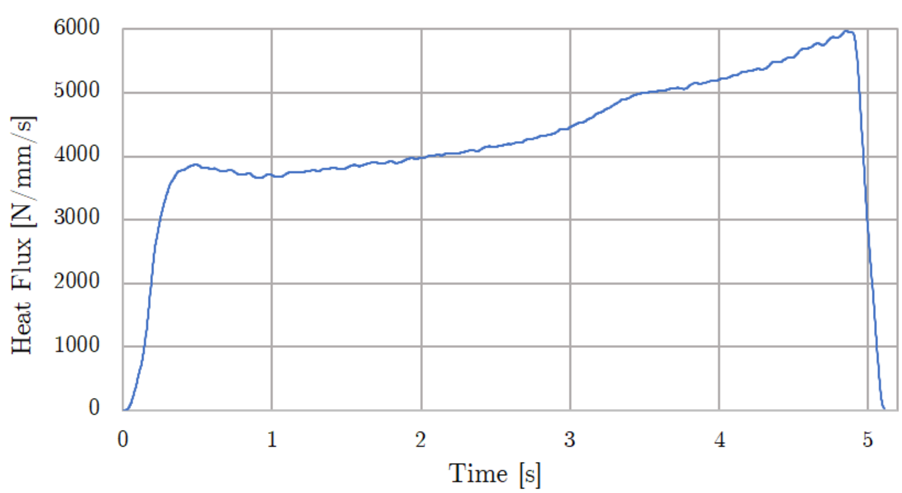

Figure 4.24. Heat flux versus time for weld number 16

Figure 4.25 shows the temperature growth in DEFORM for the purely thermal model of the initial phase of LFW. Using point tracking, temperatures were tracked at the exact locations of the thermocouples in the experiment. Figure 4.26 compares

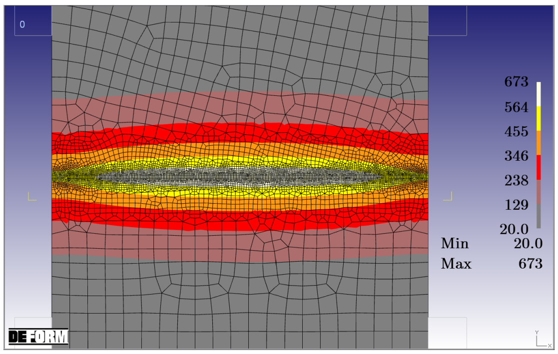

(a)

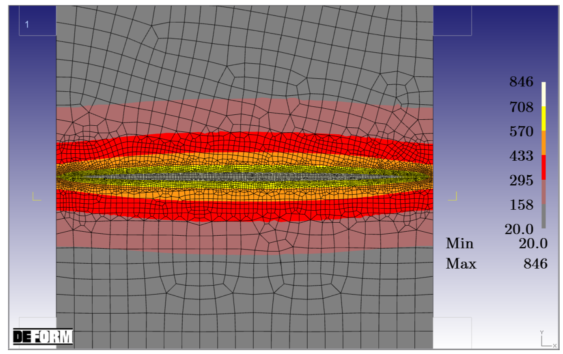

(b)

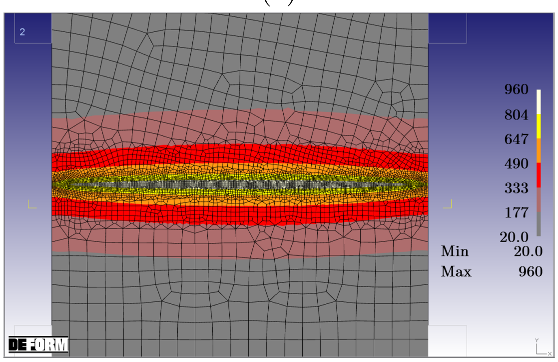

(c)

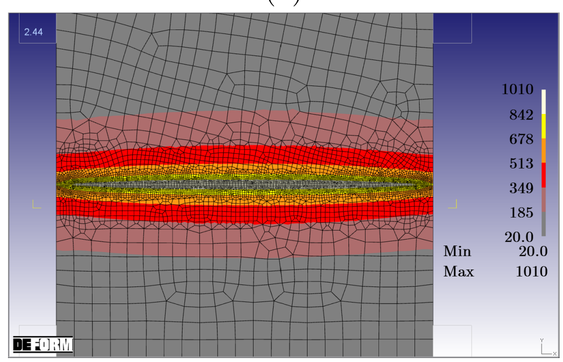

(d)

Figure 4.25. Purely thermal model for the initial phase of weld 16 after (a) 0 seconds, (b) 1 second, (c) 2 seconds, and (d) 2.44 seconds, the end of the initial phase for weld number 16.

the temperatures from the numerical model versus the temperatures recorded during the experiment at the four thermocouple locations described in Chapter 2. The maximum percent error between the numerical model and a thermocouple at the end of the initial phase was 16.7%.

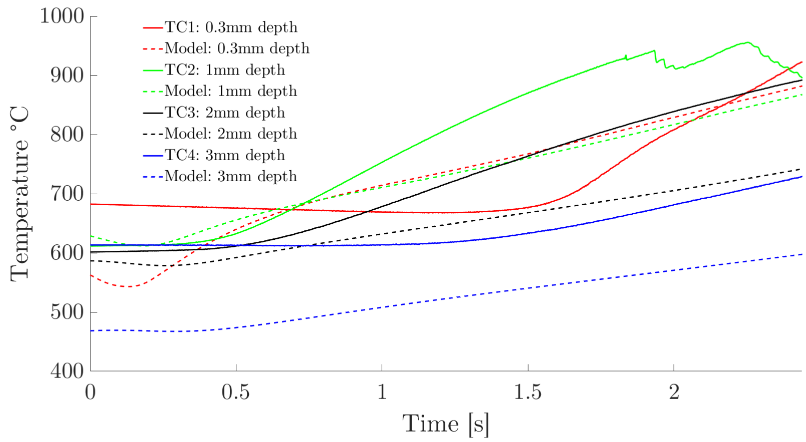

Figure 4.26. Comparison of the LFW thermal simulation for the initial LFW phase of weld number 16 and the experimental temperature measurements

4.4.2 Latter phases of LFW numerical model

Figure 4.27 shows the temperature and strain growth in weld number 11 throughout the LFW phases. If the latter phases of the LFW process had been modeled, it is worth noting that the experimentally measured temperatures can only be assumed accurate up until the moment that the thermocouple is consumed by the flash. In other words, as the two workpieces join and begin to travel towards each other (upset), the thermocouples placed at 0.3 mm, 1.0 mm, 2.0 mm, and 3.0 mm will eventually cross into the region of plastically deforming material at upset distances of approximately 0.6 mm, 2.0 mm, 4.0 mm, and 6.0 mm, respectively (assuming an equal amount of flash is formed from both workpieces). So, for welds 14 and 16 with target upset distances of 2.5 mm, the two closest thermocouples are likely to enter into the plastically deforming region.

It is hoped that FEA software packages in the future resolve the issue of contact loss at the workpiece surfaces, and that future LFW modeling research groups will utilize the friction user routines in Appendix A.

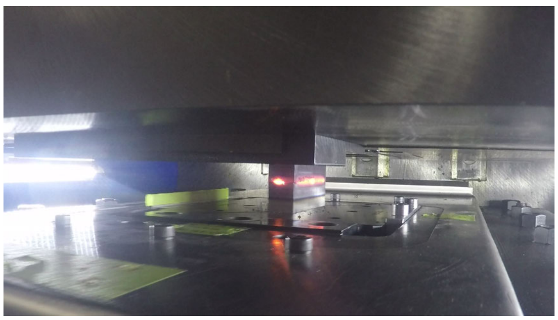

(a) (b)

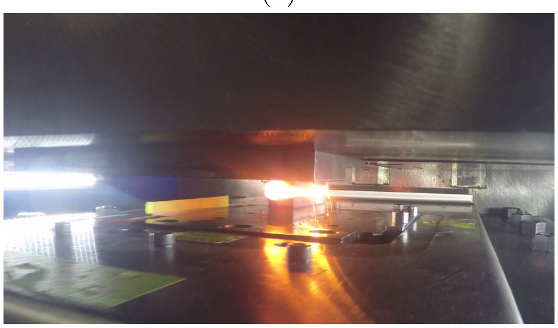

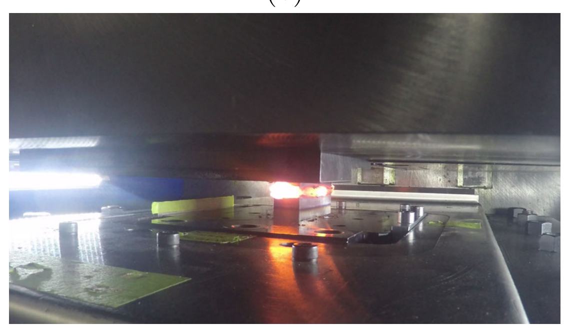

(c) (d)

Figure 4.27. Still images from a video of weld number 11 from the DOE during the LFW stage

CHAPTER 5

EVALUATION OF WELD PROPERTIES

As discussed in Section 2.1, an unreplicated, two-level factorial DOE (Table 2.1) was used to study the effect of four process parameters (or, in the nomenclature of design of experiments, factors):

1. Average rubbing velocity (equal to four times the oscillation frequency and amplitude),
2. Weld pressure,
3. Upset distance (also known as burn-off distance),
4. Preheat temperature (on the surface due to induction heating),

on three outcomes (response variables):

1. Weld strength (yield strength in bending),
2. Heat affected zone (HAZ) width / peak hardness,
3. Energy usage,

for the IH & LFW of AISI 1020 steel. The following details the experimental methods used in measuring the three response variables, and reports and analyzes the results of the DOE.

A commercial DOE software package, Minitab, was used to analyze the data and determine whether any of the process parameters had significant effects on the responses. When a DOE is *replicated*, Minitab uses t-statistics to test whether or not an effect is significant; significance is determined by the differences in the group averages, the sample size, and the standard deviations of the groups. When a DOE is *unreplicated*, there are no group averages or standard deviations, and hence no internal estimate of error [48]. In these cases, there are two alternative approaches for determining significance. In one approach, significance of the *nonstandardized effects* can be determined by using Lenth's pseudo standard error (PSE) [34]. In the other approach, significance of the *standardized effects* can be determined by assuming negligible high-order interactions, also known as the sparsity of effects principle (combining their mean squares to estimate the error)[48]. In this dissertation, the results from both methods are reported in the form of Pareto charts, where the reference line for statistical significance is a dashed red line. Any factor or combination of factors that shows statistical significance will extend past this reference line.

Three requirements from the data of the response variables must be met for the DOE model to be valid:

1. The raw data must be normally distributed.
2. The residuals must be "normally and independently distributed with mean zero and constant, but unknown variance [48]."
3. The residuals must be uncorrelated.

To test if the data is normally distributed, Anderson-Darling normality tests were performed for each response variable, and normal probability plots were generated [4]. If the p-value is greater than 0.05, the hypothesis of normality is confirmed and the model is valid. To test if the residuals are normally and independently distributed with mean zero and constant, but unknown variance, residuals versus fits plots were generated. To test if the residuals are uncorrelated, residuals versus order plots were generated. If the model is valid, the structure of the plots of the residuals should not exhibit any trends or patterns.

5.1 Weld Strength

The first of the three response variables was weld strength. Initially, tension tests were performed to determine the strength of the welded joints. However, the first three tests resulted in fractures away from the weld zone, indicating weld joints stronger than the parent material. In order to determine yield strength near the weld zone, three point bending was employed, positioning the center pin directly above the weld zone to apply the greatest force there (Fig. 5.1). An MTS 810 Material Testing System was used to perform 32 bend tests (two from each weld) in accordance with ASTM E-290 standards using the guided-bend technique. The 3 hardened steel pins were 4.75 mm in radius and the span between the outside pins was 1.42 mm, corresponding to r and C in Fig. 5.1, respectively. The specimens were sectioned from the welds by wire EDM into 5.1 mm $\times$ 10.2 mm pieces, t and w in Fig. 5.1, respectively. Flexural stress-strain curves were generated for all 32 bend tests to quantify the bending behavior of the weld joints (Fig. 5.2). For three point bending, the stress at the outer fibers is given by

$$\sigma_f = \frac{3FC}{2wt^2}, \tag{5.1}$$

where F is the load, C is the span between the supports, and the beam is rectangular with dimensions $w \times t$ ($C = 36.1$ mm, $w = 10.2$ mm, $t = 5.1$ mm). The flexural strain is given by

$$\epsilon_f = \frac{6Dt}{C^2}, \tag{5.2}$$

where D is the maximum deflection of the center of the beam.

For stress-strain curves without an easily detectable transition from elastic to plastic behavior, a consistent measure of yield strength is the 0.2% offset yield point: the point at which 0.2% plastic deformation occurs. This value was calculated by drawing a line with equal slope to the initial portion of the stress-strain curve, offset

0.002 mm/mm from the origin. The point at which the stress-strain curve intersects the offset line was reported as the yield strength. Yield strength values for the two specimens per weld were averaged and reported in Table 5.1.

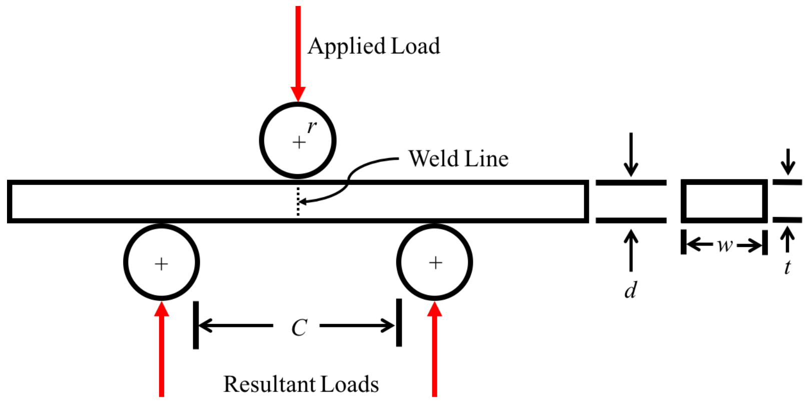

Figure 5.1. Schematic of a three point bend test

A normal probability plot of the weld strength data was generated, and confirmed the assumption of normality (Fig. 5.3). A residuals versus fits plot was generated to test for non-linearity, unequal error variances, and outliers for yield strength (Fig. 5.6). A brief evaluation of the plot shows that the residuals and the fitted values are uncorrelated and have a constant variance. A residuals versus order plot was generated to verify that the residuals were uncorrelated to each other and the order in which the test was run (Fig. 5.7). The randomness of the residuals in these plots indicates that the model is valid.

After validating the model, Pareto charts of both the *nonstandardized effects* (using Lenth's PSE), and the *standardized effects* (using sparsity of effects) were gen-

TABLE 5.1

FLEXURAL YIELD STRENGTH MEASUREMENTS

Weld Number	Pattern	Flexural Strength (MPa)
1	−−+−	707
2	+−−−	666
3	−−−+	730
4	+−+−	738
5	−++−	707
6	+−−+	737
7	++−−	699
8	−+−−	709
9	+−++	724
10	++−+	722
11	−−++	713
12	−+++	687
13	+++−	716
14	−+−+	716
15	++++	717
16	−−−−	726

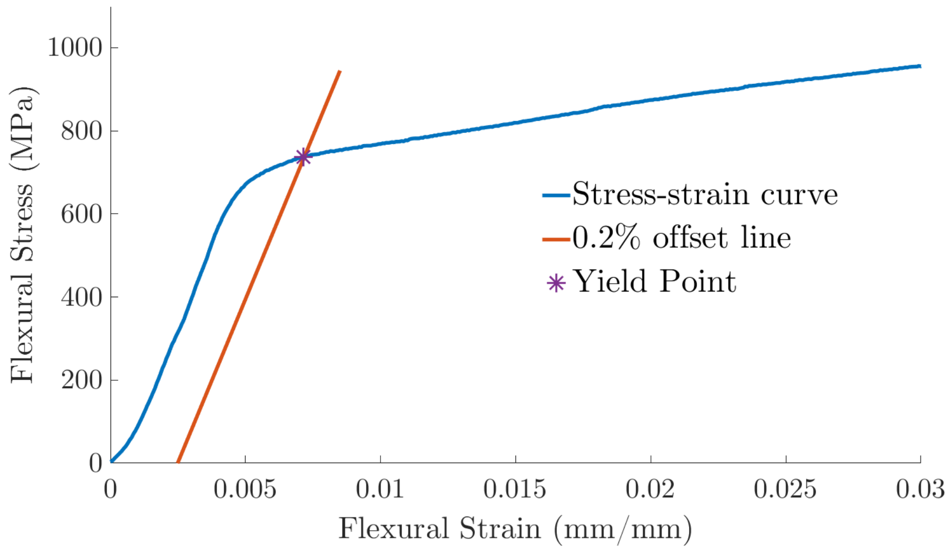

Figure 5.2. Flexural stress-strain curve for weld number 4.

erated and showed that none of the input factors or their interactions had statistically significant effects on yield strength in bending (Figs. 5.4, 5.5). The average yield strength in bending among all of the welds was 713 MPa, with a standard deviation of 18 MPa. These results suggest that weld strength was insensitive to the input factors for the parameter range tested. It is important to note that a value smaller than 2.5 mm for upset may have resulted in a decrease in weld strength; there is a minimum upset distance required to allow for the two workpieces to join and withstand a three-point bend test.

The absence of factorial influence on weld strength is understandable, since LFW is a known to be a robust process with existing machinery that can produce good welds. The finding that weld strength is insensitive to process parameters is welcome, as it allows for greater freedom in reducing energy during welding. However, there may be additional opportunities by extending machine capabilities. While the strength of an IH & LFW weld may be robust, further testing of the weld joint (i.e.

fatigue testing) should be studied to further examine weld quality.

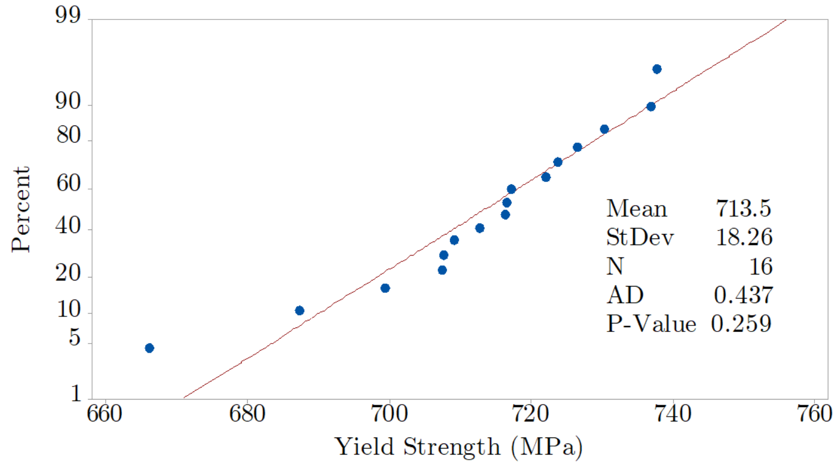

Figure 5.3. Normal probability plot for weld strength.

5.2 HAZ Width and Peak Hardness

The second of the three response variables was HAZ width/peak hardness. Increases in hardness near the weld zone can be detrimental to applications where value is placed on high toughness, therefore, a smaller HAZ width is usually desirable for a finished part. In order to determine HAZ width and peak hardness, microhardness tests were performed on a Leco M400 testing machine with a diamond-tipped pyramidal indenter following ASTM E92-17 standards. A test specimen was sectioned from each weld by wire EDM so that the plane illustrated in Fig. 5.8 could be prepared for indentation. The test specimens were then set with epoxy and ground on an automatic grinding/polishing machine with mounted abrasives of increasing fineness

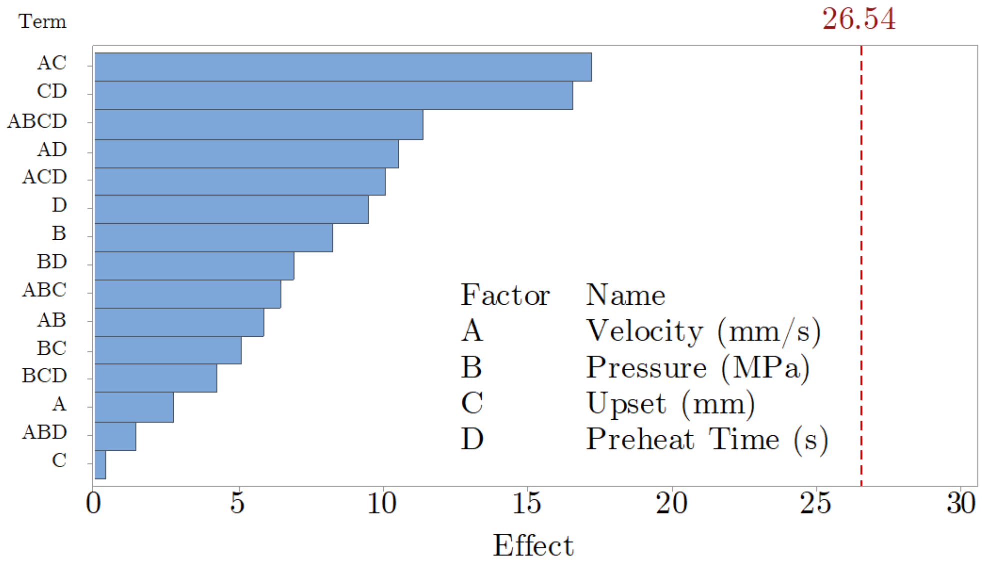

Figure 5.4. Pareto chart of the *nonstandardized effects* for flexural strength (MPa), $\alpha = 0.05$, Lenth's $PSE = 10.3240$.

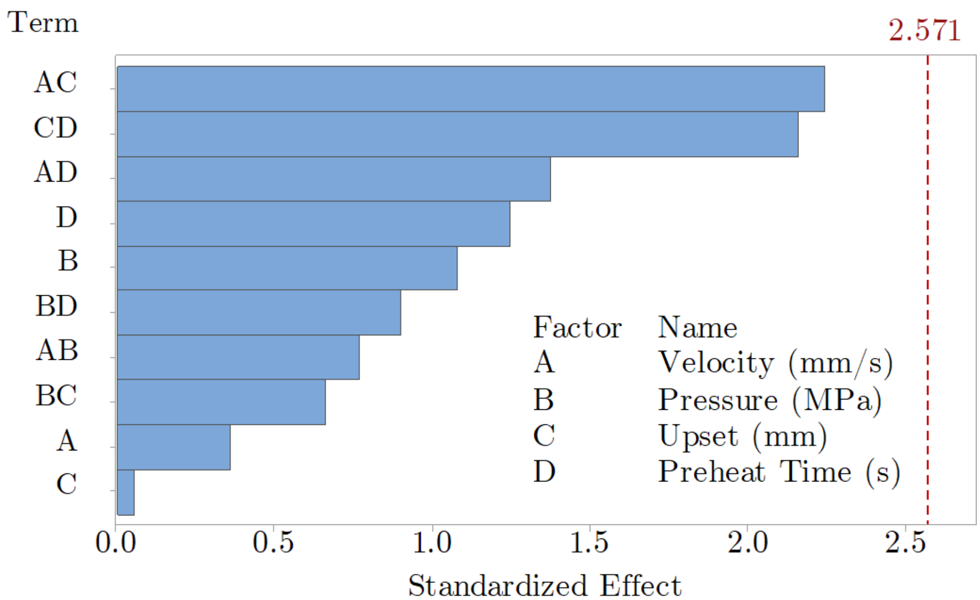

Figure 5.5. Pareto chart of the *standardized effects* for flexural strength (MPa), $\alpha = 0.05$.

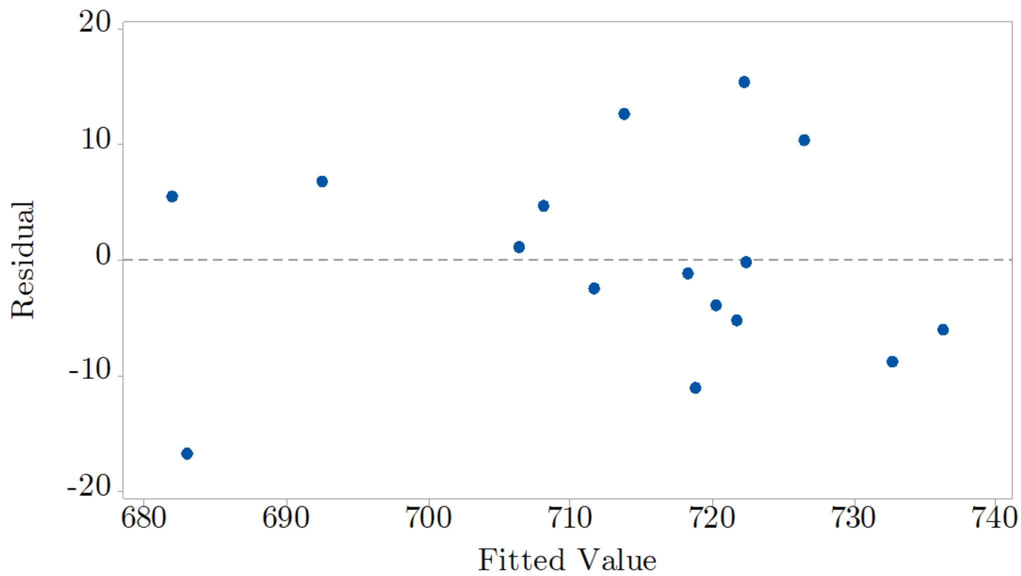

Figure 5.6. Residuals versus fits plot for yield strength.

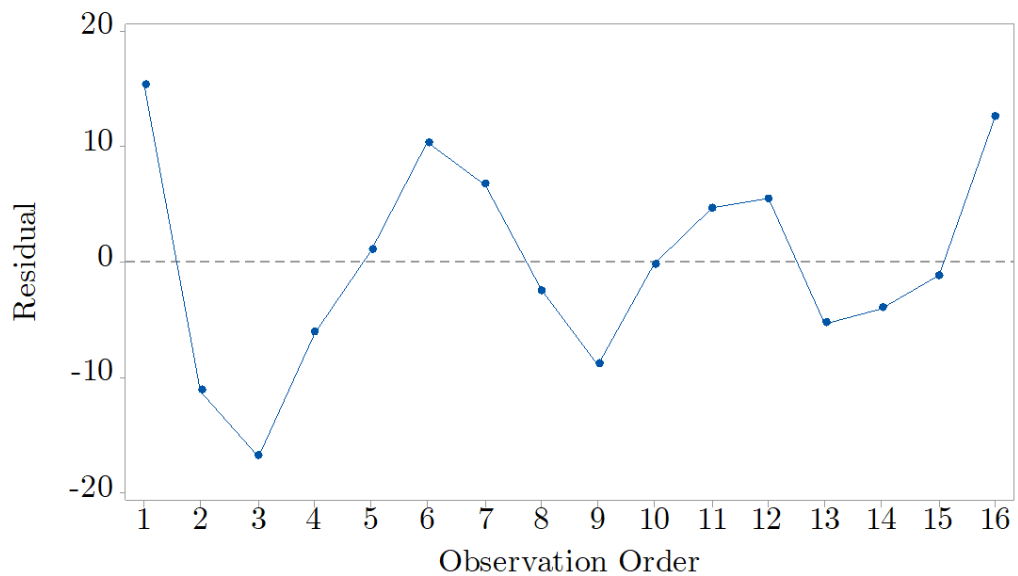

Figure 5.7. Residuals versus order plot for yield strength.

up to 2.5 microns. Indentations were made outside of the weld zone to determine a mean and standard deviation for the non-welded material. Any indentation that resulted in a Vickers hardness number (VHN) greater than one standard deviation away from the mean was considered part of the HAZ.

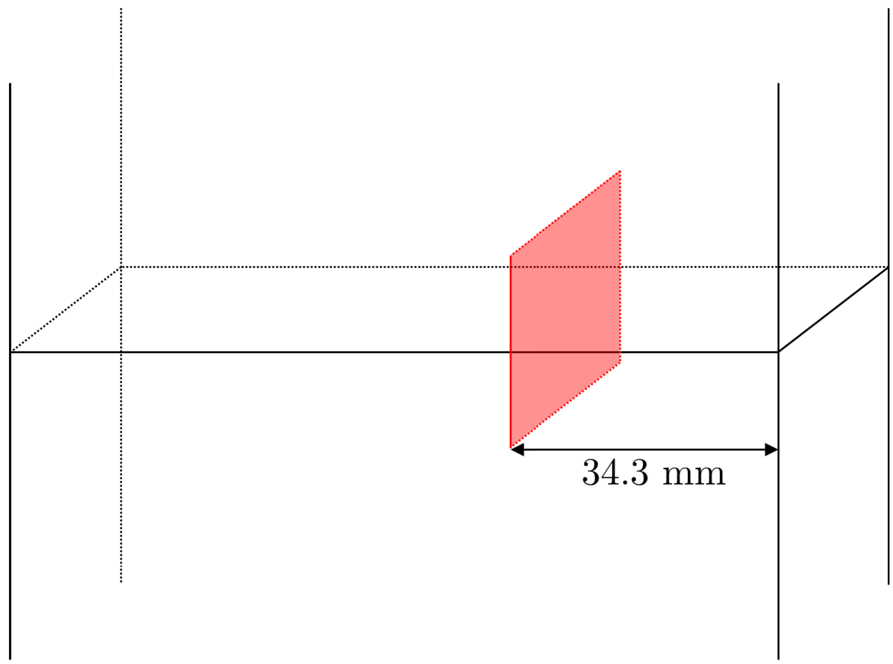

Figure 5.8. Plane where microhardness measurements were made across the weld line in the transverse direction to oscillation.

The Vickers hardness number,

$$\mathrm{VHN} = 1.8544\frac{P}{d_v^2}, \tag{5.3}$$

is a function of the indentation force P (kgf), and the mean diagonal of impression d_v

(mm). The test indentation force used was 1 kgf. The critical value to be considered part of the HAZ was 208.3 HV. The HAZ begins at the first of three consecutive measurements above this value, and ends at the last of three consecutive measurements above this value. For reference, in weld number 4 (Fig. 5.9), the HAZ width was 1.09 mm and the peak VHN was 224.8 HV. As can be seen in Fig. 5.9, the hardness measurements achieve a maximum value that was assumed to correspond with the weld line. The measured values for HAZ width and peak hardness for all 16 of the welding conditions can be seen in Table 5.2.

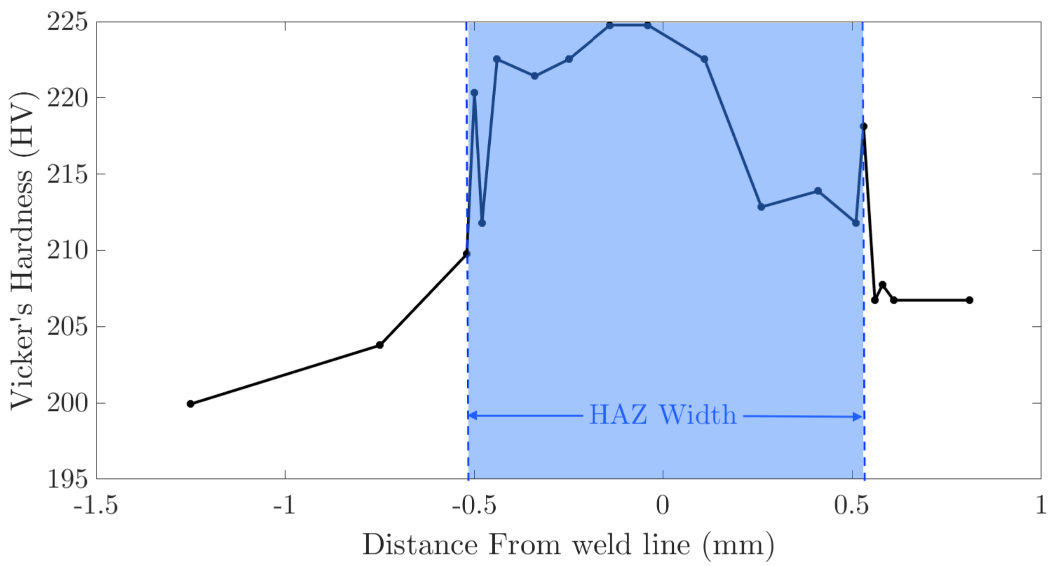

Figure 5.9. Microhardness measurements for weld number 4.

The average HAZ width was 1.02 mm with a standard deviation of 0.57 mm. During welding, temperature recordings reached as high as 930 °C. If quenched from this

TABLE 5.2

MICROHARDNESS MEASUREMENTS

Weld Number	Pattern	HAZ Width (mm)	Peak Hardness (HV)
1	−−+−	1.20	251.8
2	+−−−	0.87	260.1
3	−−−+	0.60	261.5
4	+−+−	1.09	224.8
5	−++−	0.61	262.9
6	+−−+	2.00	240.2
7	++−−	2.28	265.8
8	−+−−	0.99	247.9
9	+−++	1.40	254.5
10	++−+	0.71	247.9
11	−−++	1.65	241.5
12	−+++	0.46	231.7
13	+++−	0.90	246.6
14	−+−+	0.37	232.0
15	++++	0.98	234.1
16	−−−−	0.24	251.8

temperature, the material near the weld joint would undergo a phase transformation and form martensite, characterized by hardness levels around 800 HV [29]. Hardness measurements across the weld never exceeded 266 HV, suggesting that cooling rates post-weld were slow enough to prevent the formation of martensite near the weld zone.

In traditional LFW, thermal gradients are steep and cooling rates post-weld are high. This can lead to recrystallization of grains near the weld joint and increases in hardness due to the Hall-Petch effect [46, 77]. By heating the workpieces prior to friction welding, thermal gradients are not as steep and extend further into the workpieces, leading to lower cooling rates after LFW. The lower cooling rates may partially be responsible for the relatively small increases in hardness across the HAZ. In the future, a wider gap between the high and low values of preheat should be investigated to determine whether similar welds with little or no preheat generate larger HAZ widths and peak hardness values than those with higher levels of preheat.

Normal probability plots of both HAZ width and peak hardness were generated, confirming the assumption of normality for both (Figs. 5.10, 5.11). In order to further validate the model, an investigation into the residuals was performed. For HAZ width and peak hardness, the residuals were not correlated to the fitted values and had constant variance (Figs. 5.12, 5.14). The residuals versus order plots showed that the residuals were uncorrelated to each other and the order in which the test was run (Figs. 5.13, 5.15). The lack of structure and pattern in all of the residuals plots validates the model.

After validating the model, Pareto charts of both the *nonstandardized effects* (using Lenth's PSE), and the *standardized effects* (using sparsity of effects) were generated and showed that none of the input factors or their interactions had statistically significant effects on HAZ width (Figs. 5.16, 5.17). The same can be said for the effects on peak hardness (Figs. 5.18, 5.19).

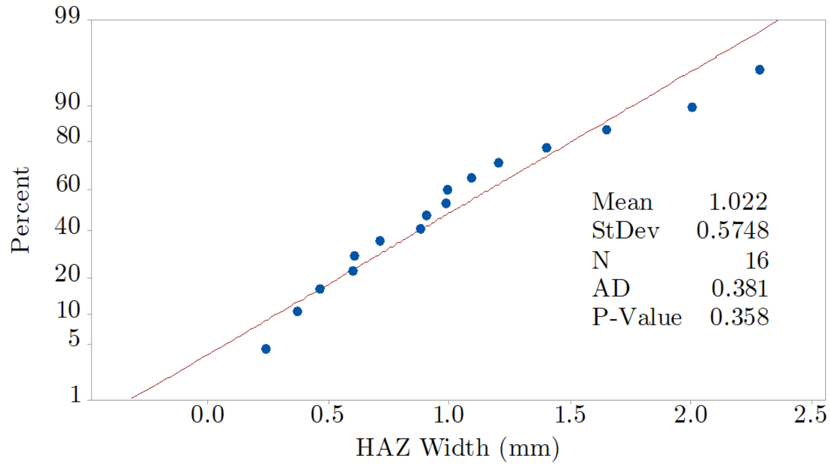

Figure 5.10. Normal probability plot for HAZ width.

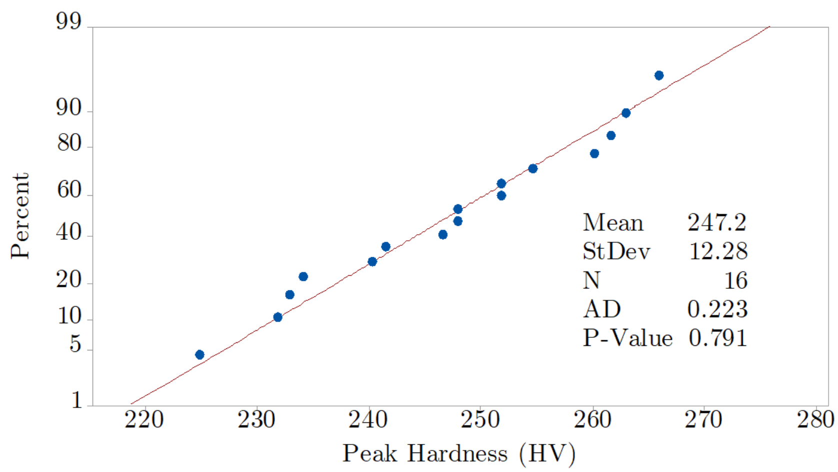

Figure 5.11. Normal probability plot for peak hardness.

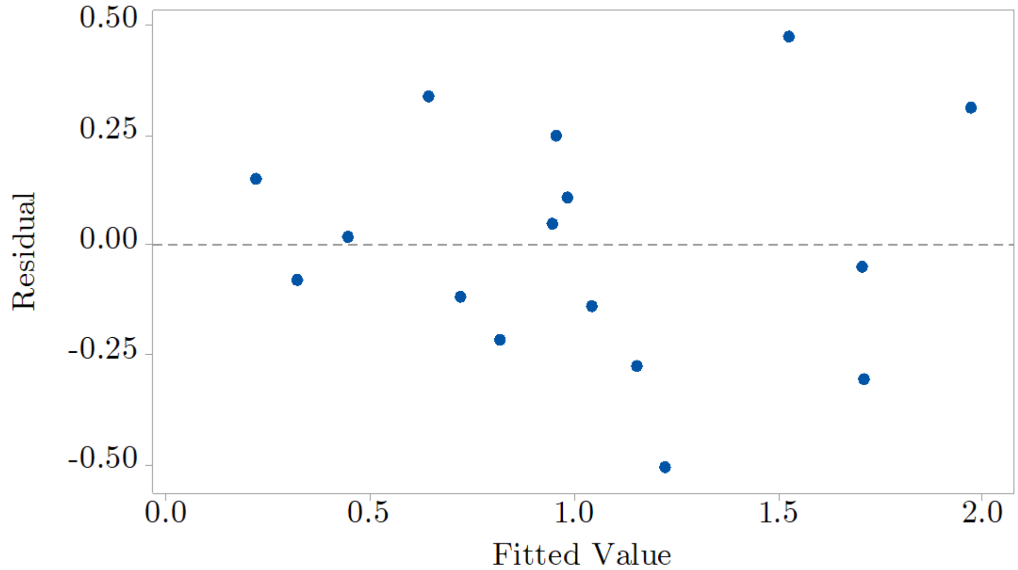

Figure 5.12. Residuals versus fits for HAZ width.

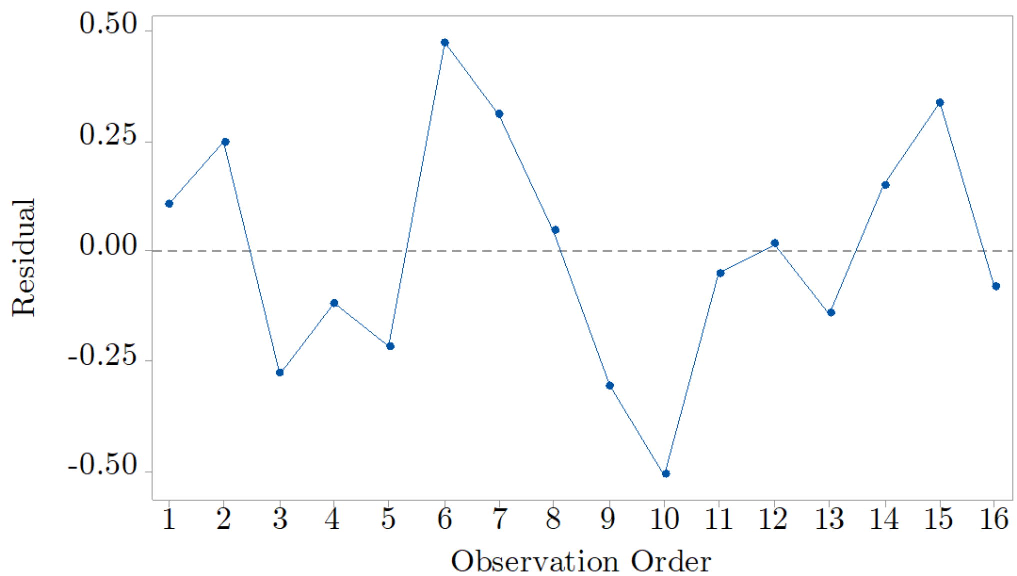

Figure 5.13. Residuals versus order for HAZ width.

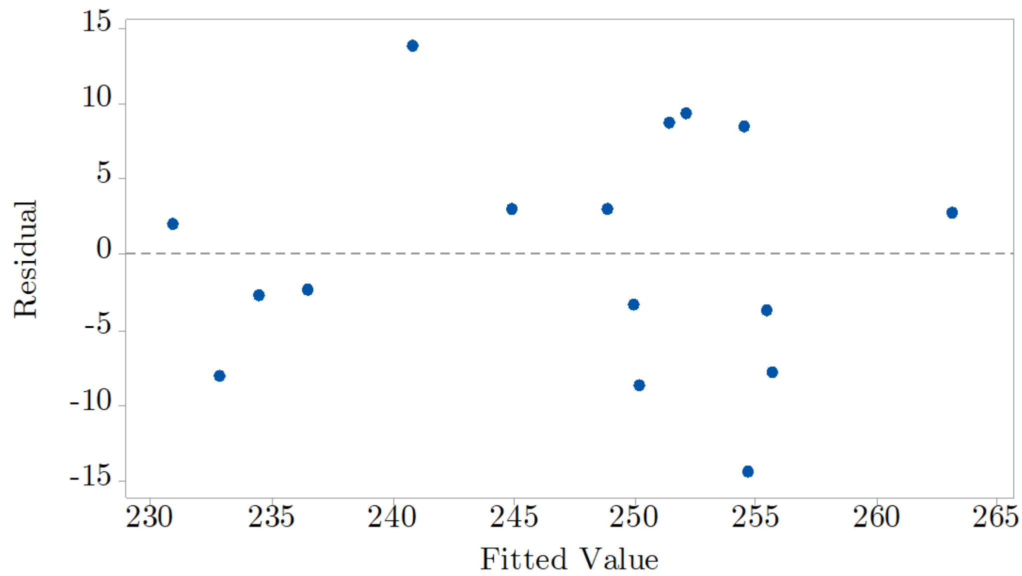

Figure 5.14. Residuals versus fits for peak hardness.

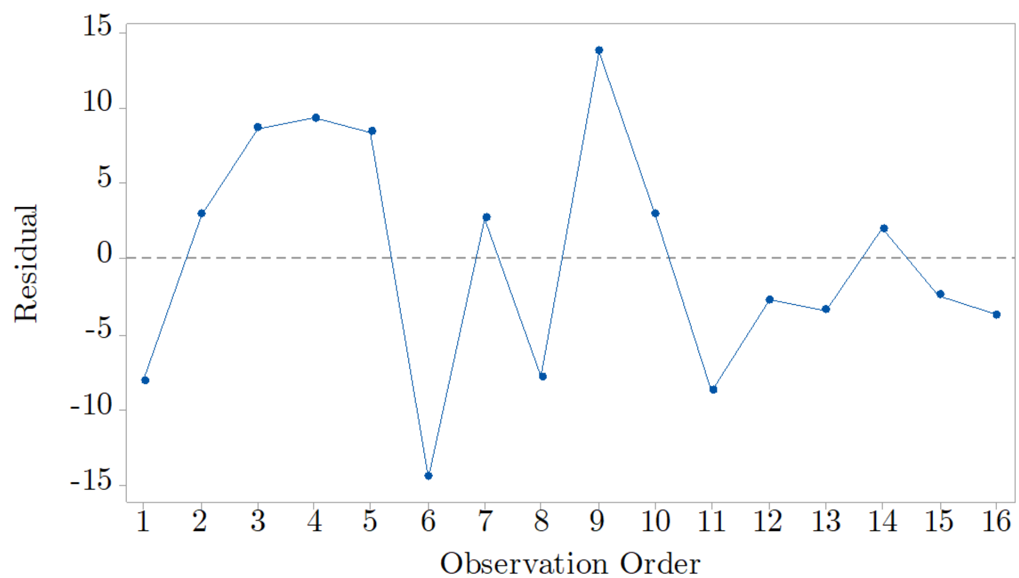

Figure 5.15. Residuals versus order for peak hardness.

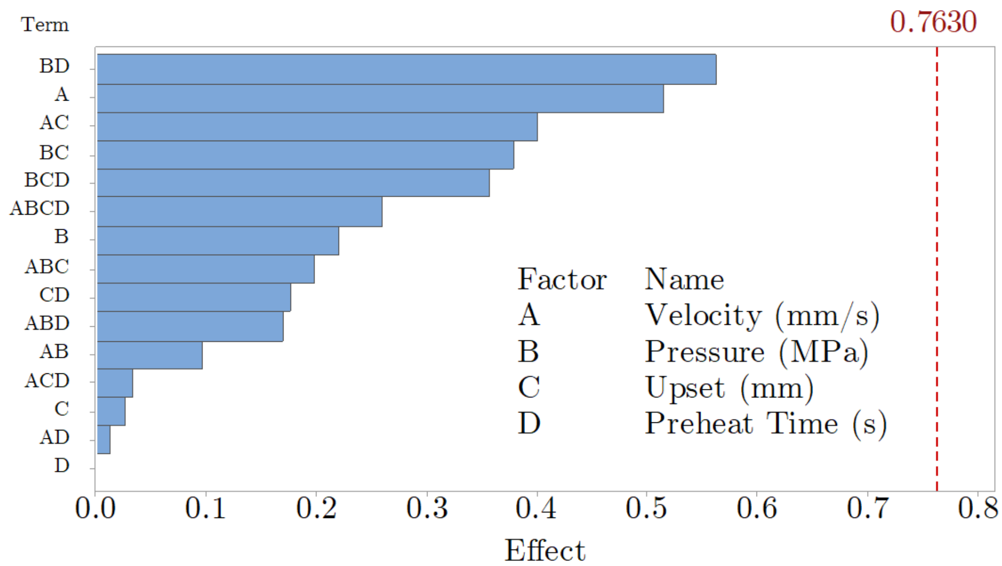

Figure 5.16. Pareto chart of the *nonstandardized effects* for HAZ width (mm), $\alpha = 0.05$, Lenth's $PSE = 0.296812$.

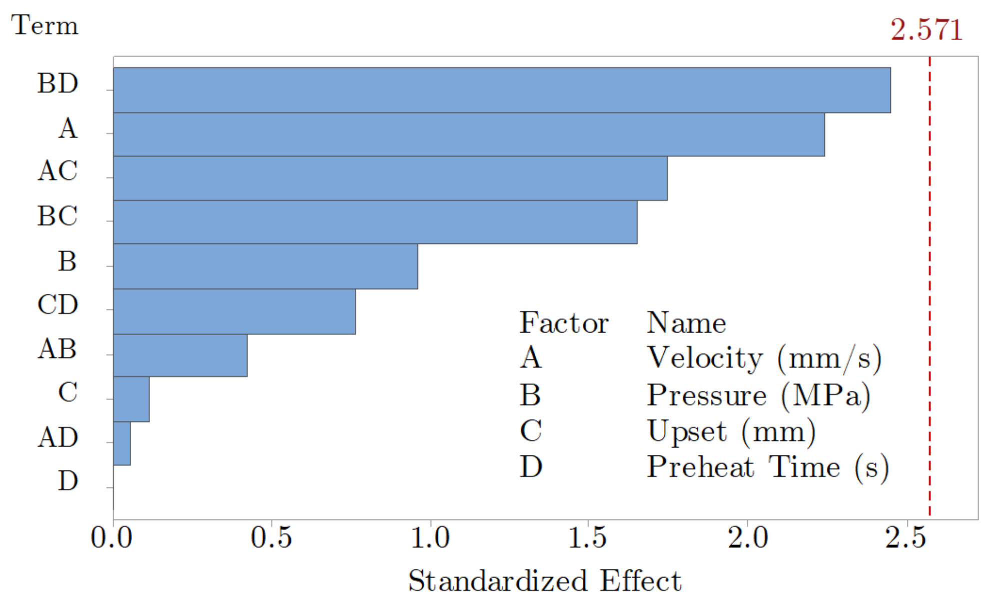

Figure 5.17. Pareto chart of the *standardized effects* for HAZ width (mm), $\alpha = 0.05$.

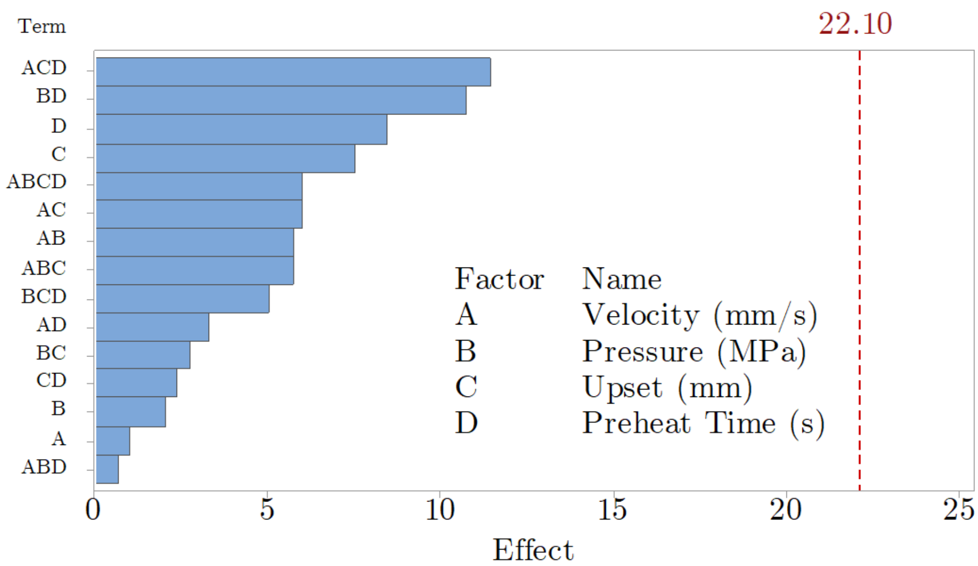

Figure 5.18. Pareto chart of the *nonstandardized effects* for peak hardness (HV), $\alpha = 0.05$, Lenth's $PSE = 8.59875$.

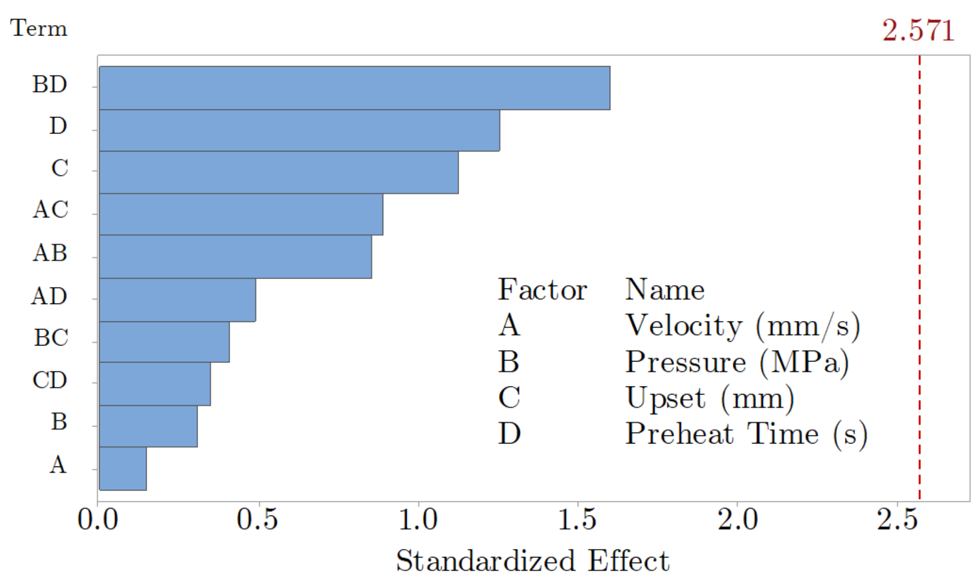

Figure 5.19. Pareto chart of the *standardized effects* for peak hardness (HV), $\alpha = 0.05$.

5.3 Energy Usage

The third response variable within the DOE was energy usage. This is given by

$$E = Pt, \tag{5.4}$$

and was defined as the energy that directly contributes to the formation of the weld joint where P is power and t is the time. The energy used during the IH step of the process was not included in the calculation. Excluding the power from IH, the power term P, of the energy equation is given by

$$P = F_f u, \tag{5.5}$$

where F_f is the friction, or process force, and u is the velocity. If F_t is the total force, and F_I is the inertial force (Fig. 5.20), then

$$F_f = F_t - F_I. \tag{5.6}$$

The velocity is given by

$$u = a\omega\cos(\omega t), \tag{5.7}$$

where a is the oscillation amplitude and ω is the angular frequency. The total force is measured by a pressure sensor on the oscillation sled, and the inertial force is equal to the combined mass of the piston rod, coupling to the sled, the sled, the tooling, and the part inside the tooling, multiplied by the acceleration $\ddot{x} = -a\omega^2\sin(\omega t)$. Acceleration and velocity are the second and first derivatives of the position $x = a\sin(\omega t)$ of the oscillator, respectively. Figure 5.21 shows power vs. time during the LFW portion of weld number four. Results from energy usage during the welds (not including energy consumed during IH) are listed in Table 5.3.

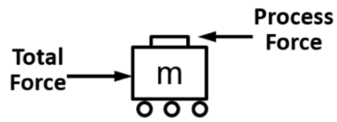

Figure 5.20. Dynamic analysis of forces.

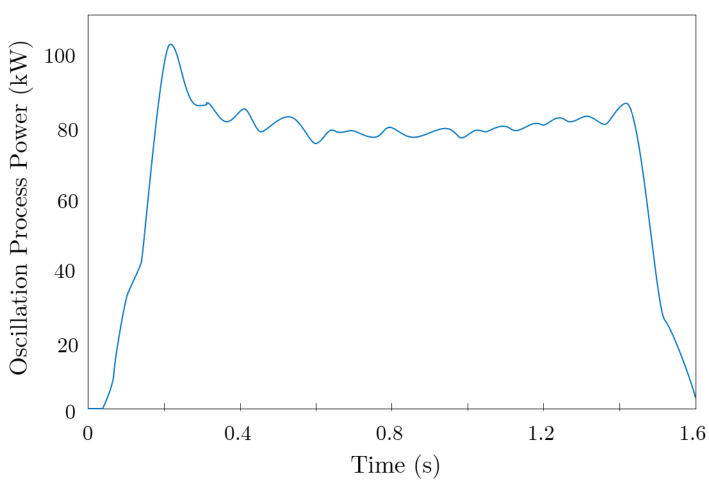

Figure 5.21. Power vs. time for an induction heated linear friction weld.

The average amount of energy used was 146.1 kJ with a standard deviation of 80.5 kJ. An Anderson-Darling normality test was performed on the data collected for energy usage and the test showed a p-value less than 0.05, indicating a non-normal distribution (Fig. 5.24). Therefore, the energy usage data was transformed to normality using a Box-Cox Transformation [9]. In order to further validate the model, an investigation into the residuals was performed and showed that they are not correlated to the fitted values, have constant variance, and were uncorrelated to each other and the order in which the test was run, as evidenced by the lack of structure and pattern in the plots (Figs. 5.23, 5.22).

After normalizing the data and validating the model, a Pareto chart of the *non-standardized effects* (using Lenth's PSE) was generated and showed that weld pressure and average rubbing velocity had significant effects on energy consumed (Fig. 5.25). When using the second approach for quantifying significance (sparsity of effects), the Pareto chart of the *standardized effects* showed that upset also had a significant effect on energy consumed (Fig. 5.26). A main effects plot was generated for the average rubbing velocity, weld pressure, upset distance, and preheat temperature on the transformed data for energy consumed (Fig. 5.27). Pressure had the most significant effect on energy used, followed by velocity and upset. Pressure had an inverse effect on energy used, whereas velocity and upset had linear effects. Equation 5.8 is the regression equation that shows the relationship between the process parameters and the energy consumed, where E is energy use is kJ, u is average rubbing velocity in mm/s, p is the weld pressure in MPa, d is upset distance in mm, and T is preheat temperature.

$$E = 145.4 + 0.30u - 1.88p + 26.5d - 0.08T, \tag{5.8}$$

The significance of weld pressure, average rubbing velocity, and upset distance on energy use can be explained:

TABLE 5.3

ENERGY CONSUMED DURING WELDING

Weld Number	Pattern	Energy Usage (kJ)
1	$--+-$	163.2
2	$+---$	167.8
3	$---+$	114.7
4	$+-+-$	341.2
5	$-++-$	98.2
6	$+--+$	252.9
7	$++--$	109.0
8	$-+--$	77.5
9	$+-++$	273.4
10	$++-+$	80.3
11	$--++$	149.6
12	$-+++$	71.3
13	$+++-$	119.7
14	$-+-+$	49.6
15	$++++$	111.3
16	$----$	157.6

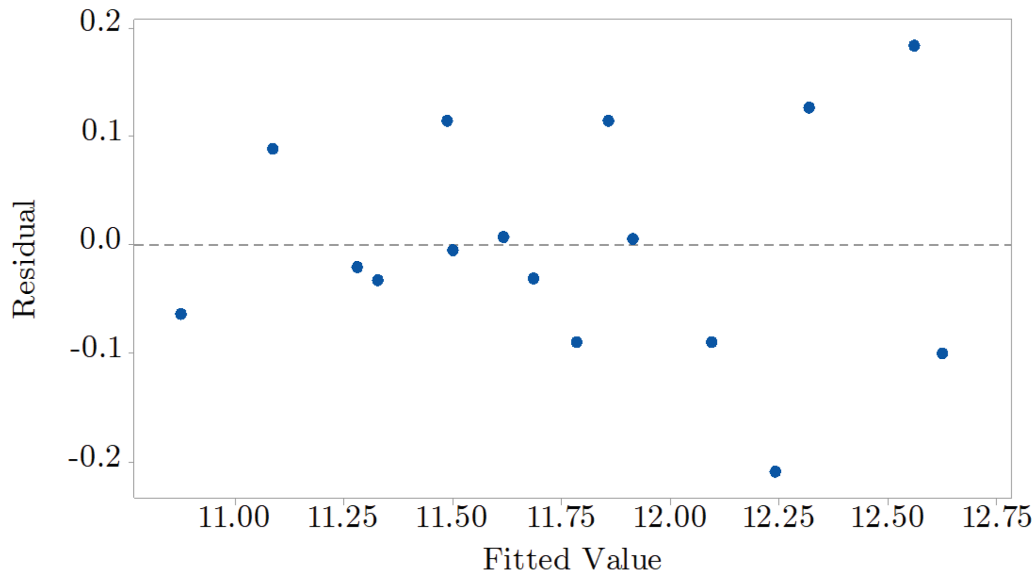

Figure 5.22. Residuals versus fits for transformed energy used.

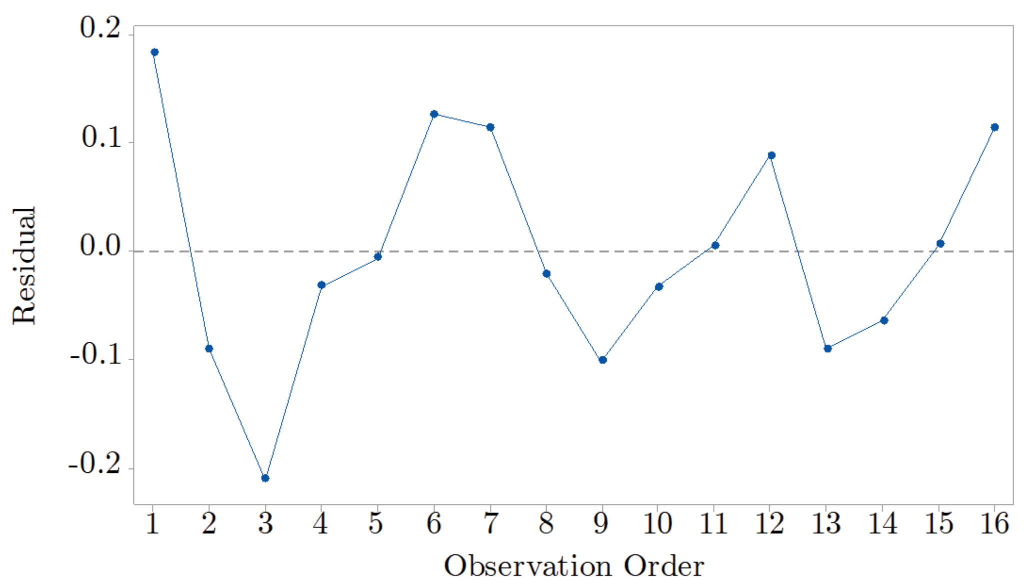

Figure 5.23. Residuals versus order for transformed energy used.

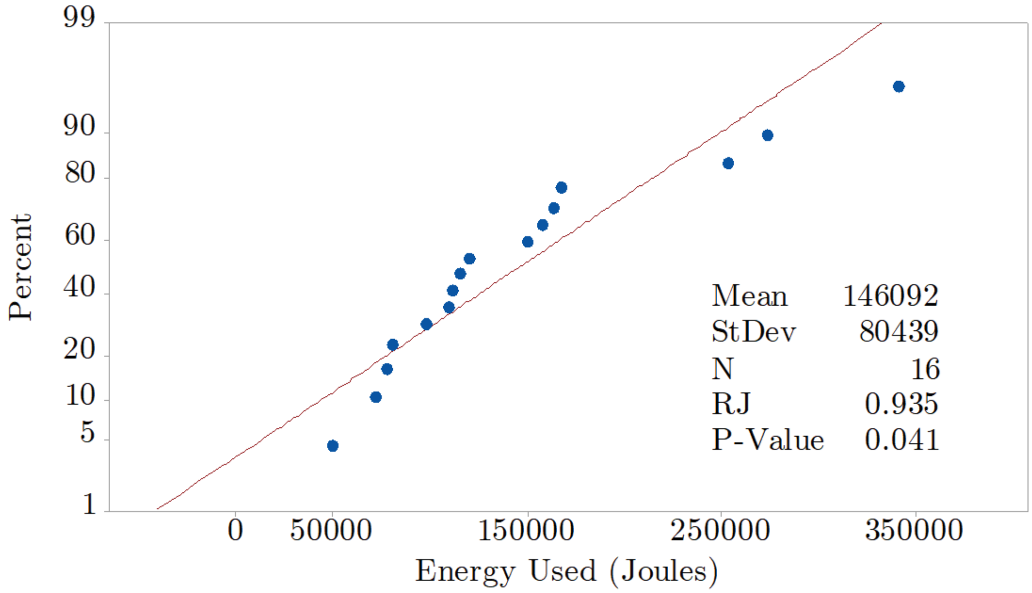

Figure 5.24. Normal probability plot for energy used.

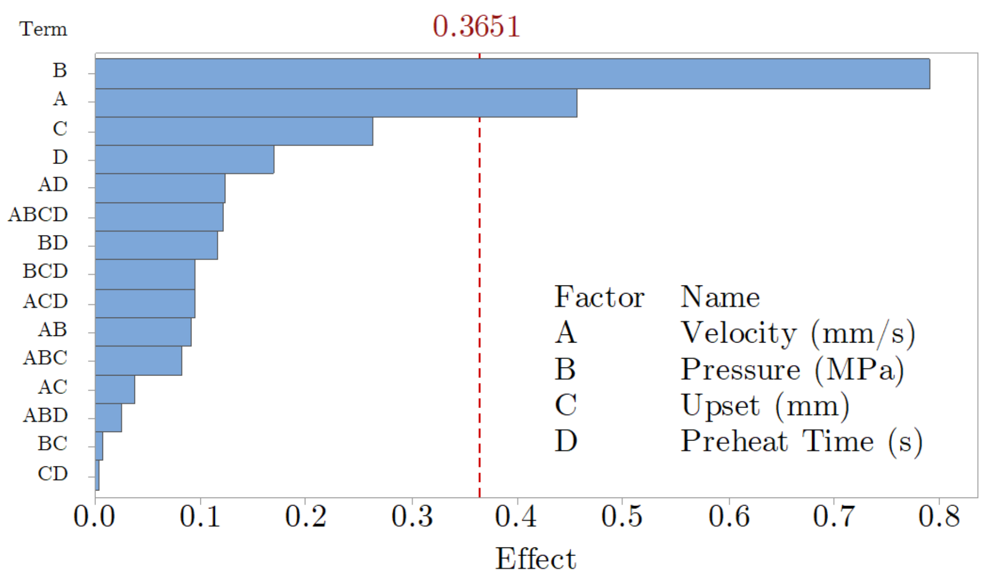

Figure 5.25. Pareto chart of the *nonstandardized effects* for transformed energy used, $\alpha = 0.05$, Lenth's $PSE = 0.142038$.

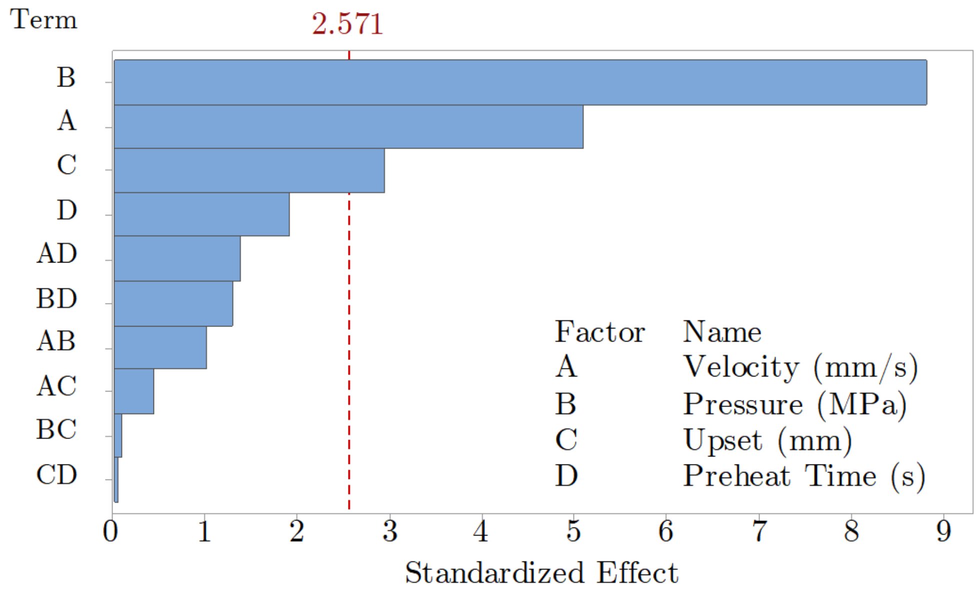

Figure 5.26. Pareto chart of the *standardized effects* for transformed energy used, $\alpha = 0.05$.

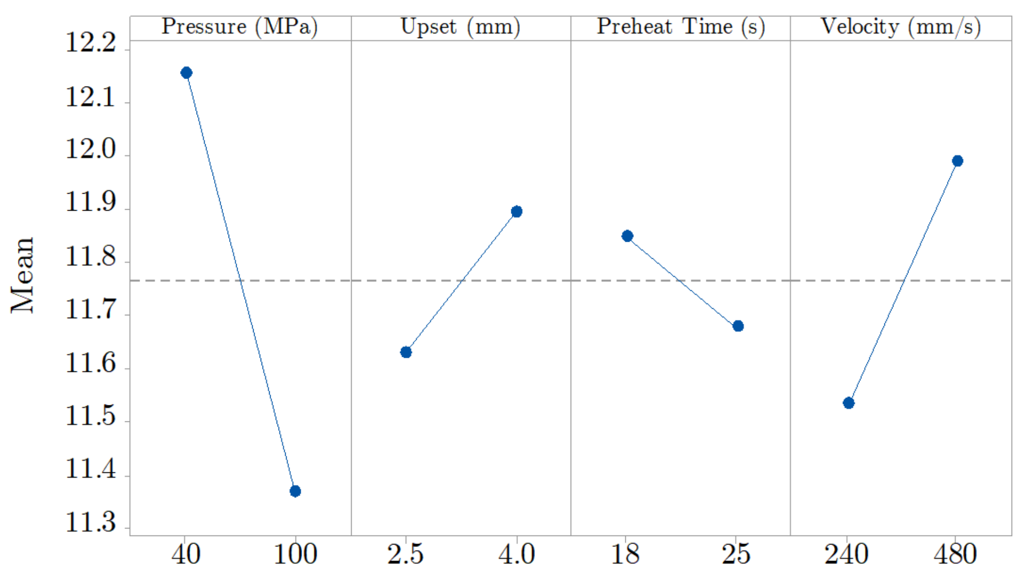

Figure 5.27. Main effects for transformed energy used.

1. *Weld pressure*: The length of a linear friction weld is determined by the time it takes to reach the desired upset distance; when the forge slide reaches a predetermined upset distance, the oscillator decelerates, and the forge slide compresses the joint. By increasing weld pressure, friction force and power increase, so that the length of time it takes to reach the desired upset distance decreases. A reduction in time directly leads to a reduction in energy use. A similar effect on energy use was reported by McAndrew et al. [45].

2. *Average rubbing velocity*: The final calculation of the required power is dominated by rubbing velocity because the oscillation frequency ω, is cubed and the amplitude A, is squared. Therefore, lower rubbing velocities will lead to lower energy use as long as weld time is not increased.

3. *Upset distance*: As explained above, increasing the upset distance will increase the time it takes to complete a weld, increasing the energy use.

It is important to note that the results from this DOE are only true within the parameter range tested. In this range, as upset distance decreased, energy use decreased. Because higher pressures and lower velocities lead to lower energy use without compromising on weld strength or HAZ width, pressures higher than 100 MPa and velocities lower than 240 mm/s should be investigated. Concurrently, the amount of flash decreases and surface contaminants can become entrapped in the weld zone. Therefore, the ideal upset distance is the minimum amount of upset at which all the surface contaminants are expelled into the flash. In order to determine the optimum parameter settings, a full factorial design must take place varying the most important parameters (pressure, rubbing velocity, upset).

In the above evaluation of energy use, LFW *machine energy* was neglected and only the *process energy* was considered (i.e. the energy input at the interface during LFW). IH energy was excluded from the calculations because only the IH *machine energy* was measured; there was no way to calculate the *process energy* of IH (i.e. the energy input at the workpiece surfaces during IH).

Keeping in mind that that there are losses in energy between the IH machine and the workpieces: if the machine energy from the IH is included in the calculation of energy use, it increases by 467.5 kJ, or 635.4 kJ for the lower or higher levels of preheat, respectively. Adding in the comparatively large amounts of energy from IH alters the Pareto charts of both the *nonstandardized* (using Lenth's PSE) and *standardized* effects (using sparsity of effects) so that preheat temperature has the largest positive effect on energy usage (Figs. 5.28, 5.29). The positive effect of upset distance on energy use is no longer significant after taking into account energy due to IH. The regression equation also changes (Eq. 5.9).

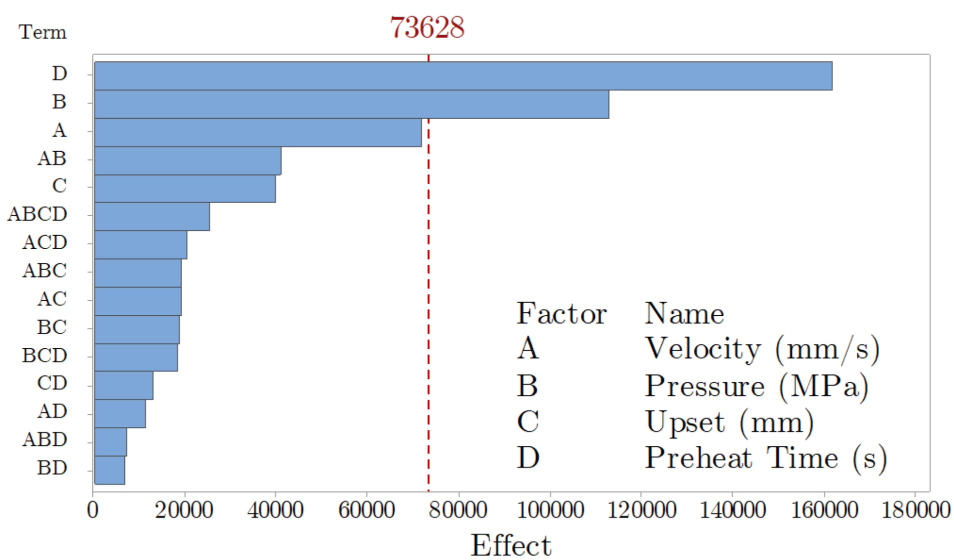

Figure 5.28. Pareto chart of the *nonstandardized effects* for energy used, $\alpha = 0.05$, Lenth's $PSE = 28{,}642.7$.

$$E = 24.7 + 0.30u - 1.88p + 26.5d + 0.8T, \tag{5.9}$$

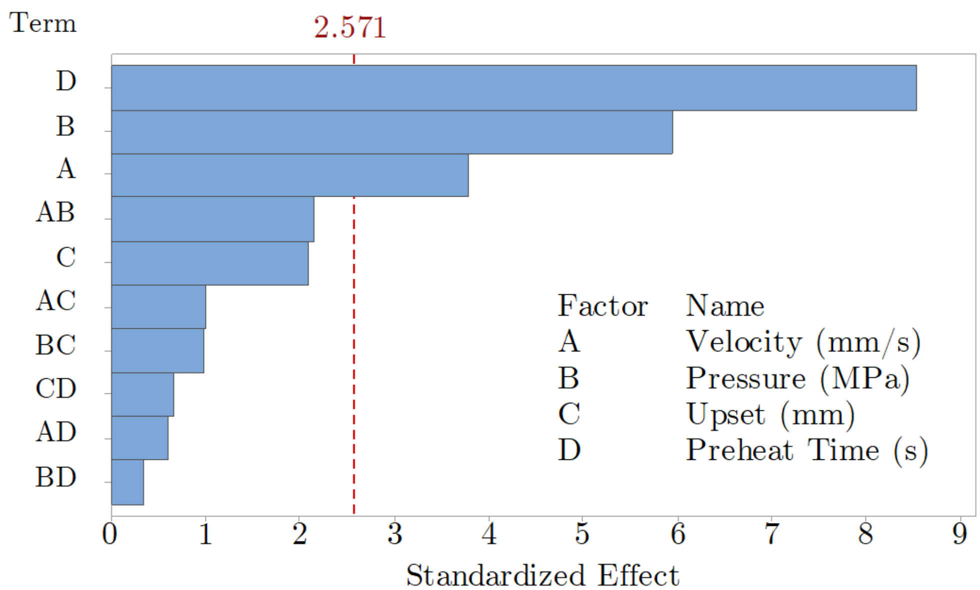

Figure 5.29. Pareto chart of the *standardized effects* for energy used, $\alpha = 0.05$.

CHAPTER 6

MICROSTRUCTURAL INVESTIGATION

Understanding the fundamental mechanics of the LFW process is key to understanding the microstructure, properties and performance of the welded joint. This type of causation has been referred to as the process-structure-property-performance (PSPP) paradigm [66]. In previous chapters, the IH and LFW process was described in detail. In this chapter, the structure of the material in the welded region is investigated via Optical Microscopy (OM) and Scanning Electron Microscopy (SEM). Understanding the structure of metals can help predict its mechanical properties (strength, hardness), and these mechanical properties can help predict the performance of the material that makes up an object.

In order to examine the microstructure of the welded joints, the microhardness test specimens sectioned from welds 14, 15, and 16 in Section 5.2 were set in epoxy a second time and ground on an automatic grinding/polishing machine with mounted abrasives of decreasing grain size down to 0.5 microns. The specimens were then etched with No. 1 Nital etchant (5% Nitric Acid concentration in alcohol) for 20 seconds before undergoing examination under optical and scanning electron microscopes.

Figure 6.1 shows the iron-carbon eutectic phase diagram. This phase diagram can help determine the types of microstructure expected for iron-carbon steels with varying carbon content. The eutectoid is the point at which upon cooling, a solid phase transforms into two other solid phases. For iron-carbon, austenite transforms into lamellae of alternating α ferrite and cementite, at the eutectoid point 0.76%

carbon. Alloy steel with a carbon content of less than 0.76% are known as hypoeutectoid steels, and alloy steel with a carbon content of greater than 0.76% are known as hypereutectoid steels.

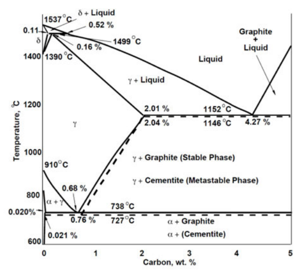

Figure 6.1. Iron-carbon euctectic phase diagram [31]

For hypereutectoid steels (steels with a carbon content greater than 0.76%), during cooling, austenite begins to nucleate into cementite, so that the microstructure is made up of austenite and proeutectoid cementite. As it cools below the eutectoid temperature of 727°C, the austenite transforms into alternating lamellae of α ferrite phase and cementite, also known as pearlite. This yields a final microstructure of proeutectoid cementite and pearlite.

Conversely, for hypoeutectoid steels (steels with a carbon content less than 0.76%), during cooling, austenite begins to nucleate into ferrite, so that the microstructure is made up of austenite and proeutectoid ferrite. As it cools below the eutectoid temperature of 727°C, the austenite transforms into pearlite, and yields a final microstructure of proeutectoid ferrite and pearlite.

For this thesis, a hypoeutectoid steel was chosen, meaning that given proper time for heating and cooling, the microstructure would evolve as described above. Therefore, as cast, the microstructure should consist of proeutectoid ferrite and pearlite. When hypoeutectoid carbon steel is etched with nital, pearlite is darkened and proeutectoid ferritic boundaries are revealed in lighter regions.

6.1 Base Material

Optical and scanning electron microscopes captured images of the material outside of the weld zone at 100X and 250X magnification, respectively. Figures 6.2 and 6.3 show the microstructure of 1020 steel for for four different material samples. Figures 6.2a and 6.3a are from a section of non-welded material. Figures 6.2b and 6.3b, Figures 6.2c and 6.3c, and Figures 6.2d and 6.3d are from sections of material outside of the weld zone for welds 14, 15, and 16, respectively. Theoretically, these samples should look identical. Figures 6.2a and 6.3a however, are distinct from the others; the grains are uniformly spaced throughout, whereas in the others the grains are aligned vertically. In Figures 6.2 and 6.3 (b-d), the test specimen was ground, polished, and etched on a surface perpendicular to the weld plane, whereas in Figures 6.2a and 6.3a, the test specimen was ground, polished, and etched on a surface parallel to the weld plane. This is a critical difference because the steel used for this experiment was cold-rolled.

In the cold rolling process, metal sheets or bars are gradually reduced in thickness by a series of hardened rollers. For this experiment, the weld coupons were cut from 25 mm x 100 mm cold rolled plate stock. Usually the process is done at room temperature, the rollers impart a good surface finish on the metal, and the compressive forces lead to strain hardening and enhanced mechanical properties. Large grains from the original cast material deform and elongate, resulting in grains that are oriented in the rolling direction (Fig. 6.4) [28]. This manufacturing process explains the elongated grain structure seen in Figures 6.2 and 6.3 (b-d); the grains

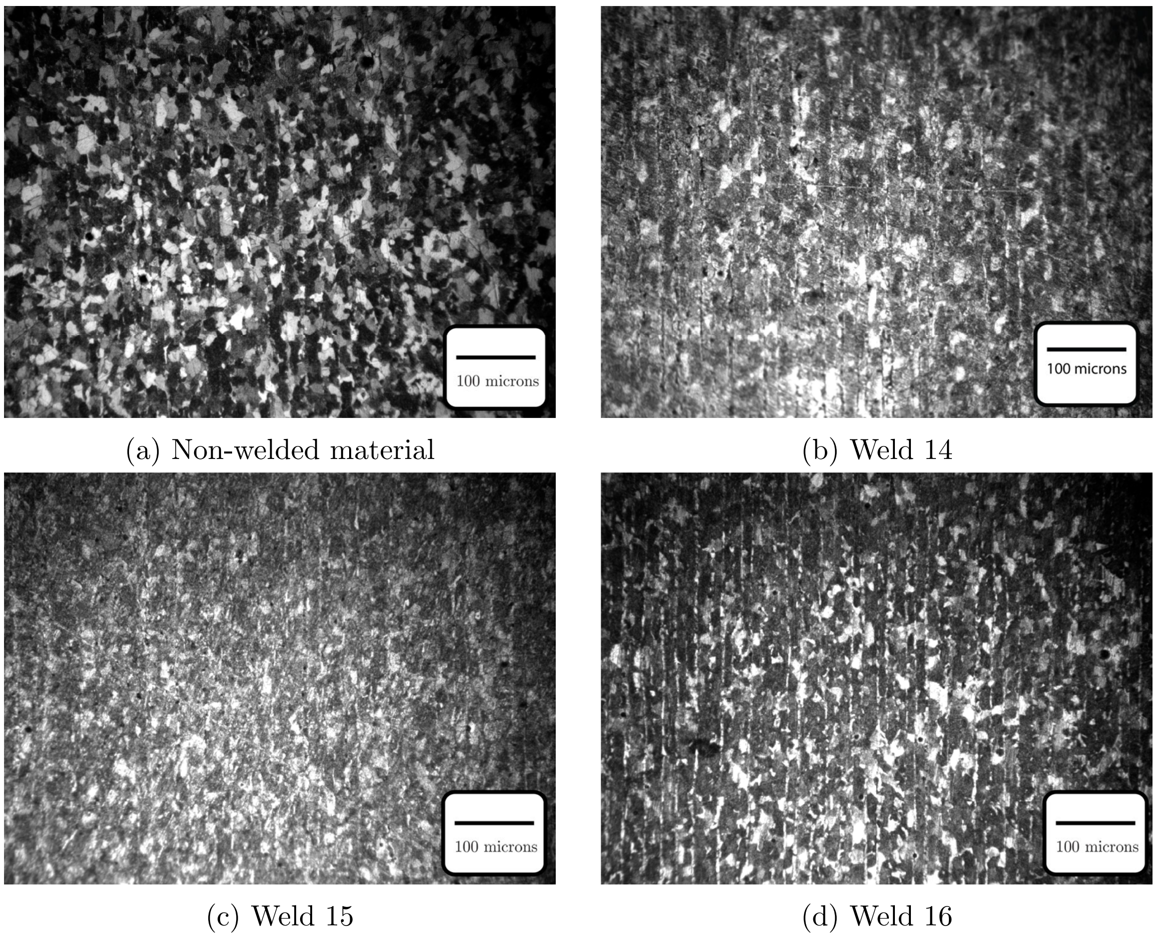

(a) Non-welded material (b) Weld 14 (c) Weld 15 (d) Weld 16

Figure 6.2. Optical micrographs of etched specimens outside the weld zone.

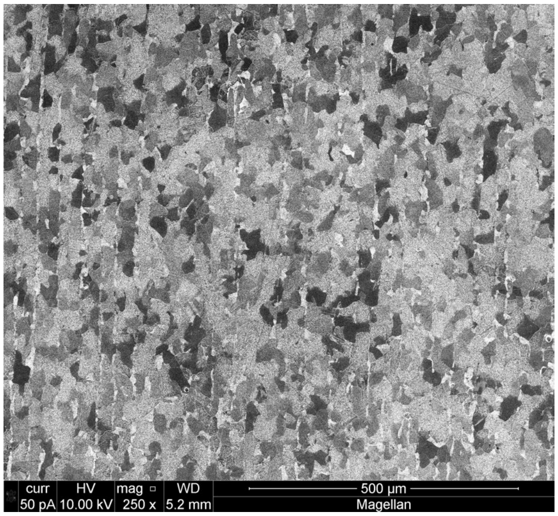

(a) Non-welded material

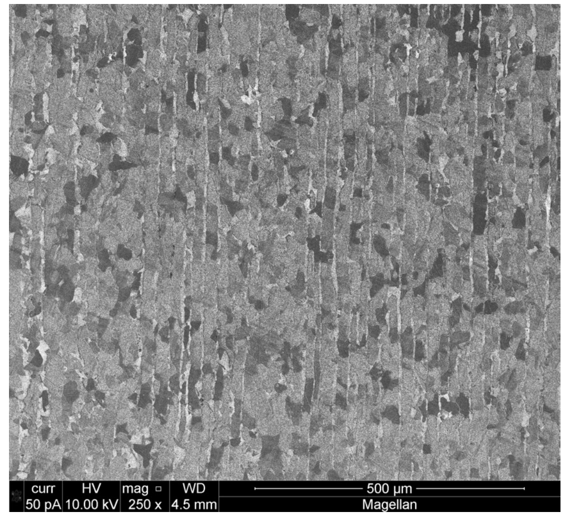

(b) Weld 14

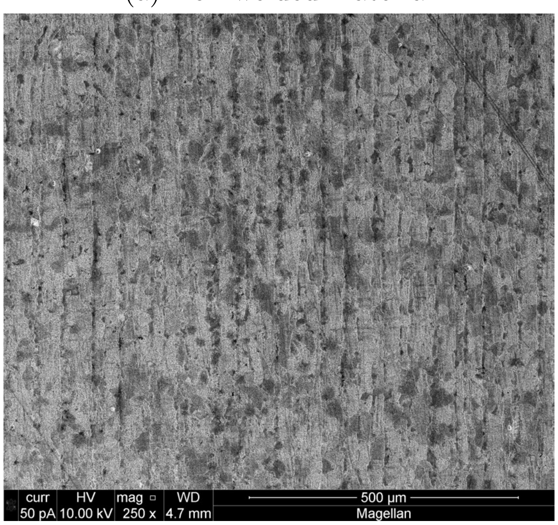

(c) Weld 15

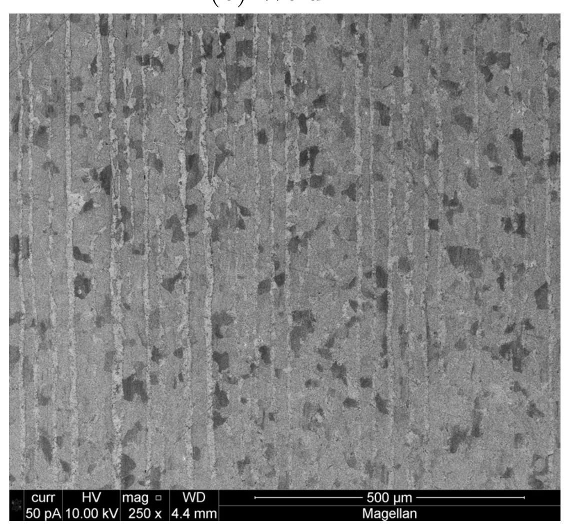

(d) Weld 16

Figure 6.3. SEM images of etched specimens outside the weld zone.

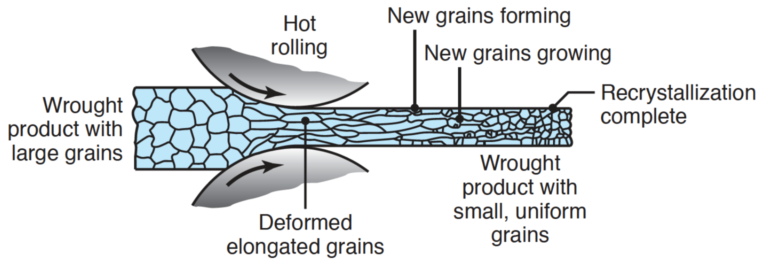

Figure 6.4. Changes in the grain structure of of cast or of large-grain wrought metals during hot rolling [28]. Unlike hot rolling, cold rolling does not allow enough time at an elevated temperature for long term grain growth and recrystallization.

are oriented vertically with the rolling direction. In Figures 6.2a and 6.3a, the test specimen was still sectioned from a cold-rolled metal workpiece, but the specimen was ground, polished, and etched on a plane perpendicular to the rolling direction, so that the plane in view of the microscope does not capture any evidence of the manufacturing process. When compared to the cast or annealed material equivalent, the cold rolled material would have smaller grain sizes.

In Figures 6.2a and 6.3a, there is clear evidence of the lighter, proeutectoid ferrite, and the darker pearlite. The resolution in these figures is not fine enough to resolve the pearlite into its alternating α ferrite and cementite lamellae.

6.2 Transition Region

The same optical and scanning electron microscopes were used to capture the transition from base material (cold-rolled) to the thermo-mechanically affected zone (TMAZ) (Figs. 6.5 and 6.6). In Chapter 5 the HAZ was defined by the hardness of the material in that region. In this chapter the TMAZ will be defined visually by evidence of strain-hardening and reduction in grain size. For each weld, there is an evidential transition from base metal (at the bottom of the images) to the TMAZ (at the top of the images) by the reduction in grain size and fading definition of the elongated, oriented, cold rolled grains. The microstructure looks otherwise similar from the base metal to the TMAZ at this resolution.

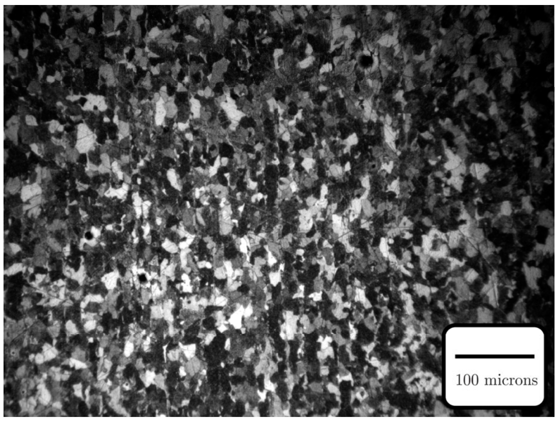

(a) Non-welded material

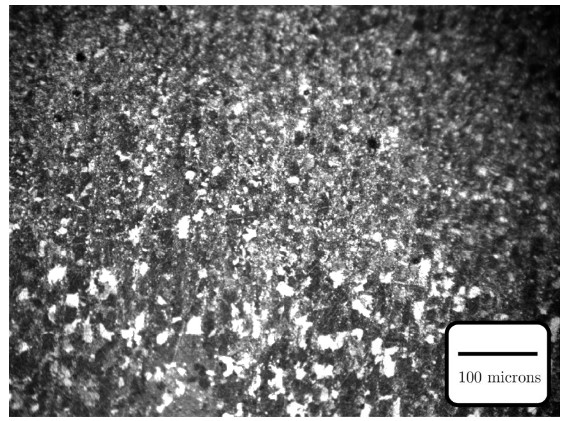

(b) Weld 14

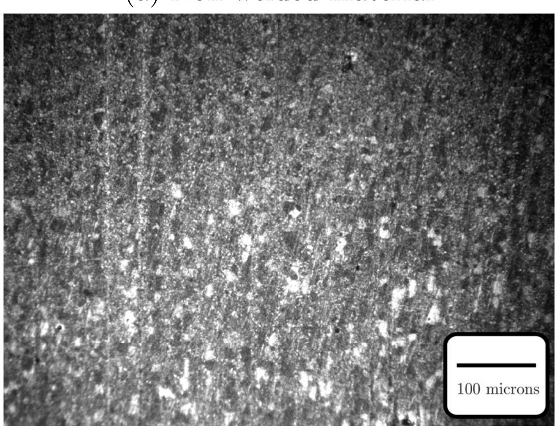

(c) Weld 15

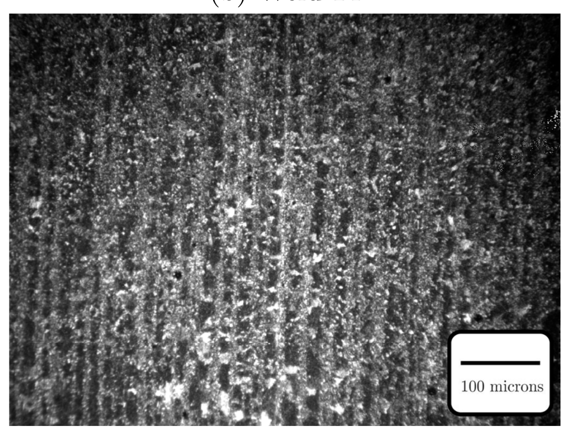

(d) Weld 16

Figure 6.5. Optical micrographs of the transition from base material to the TMAZ in etched specimens.

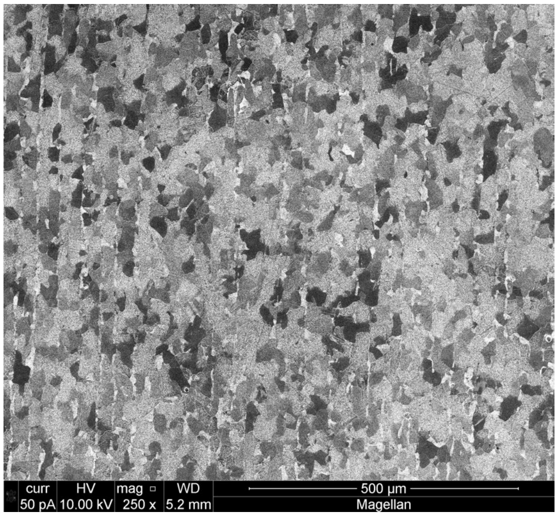

(a) Non-welded material

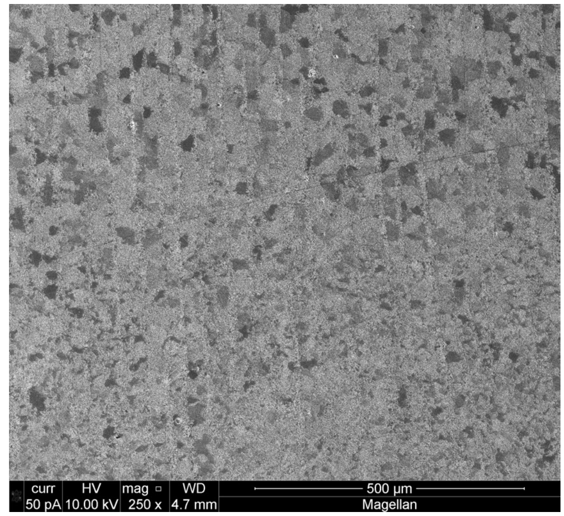

(b) Weld 14

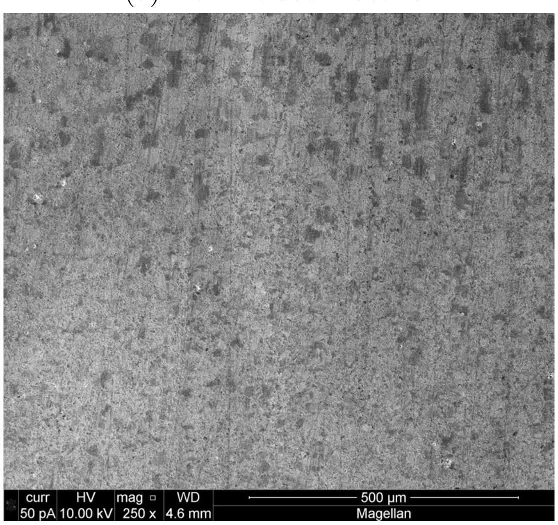

(c) Weld 15

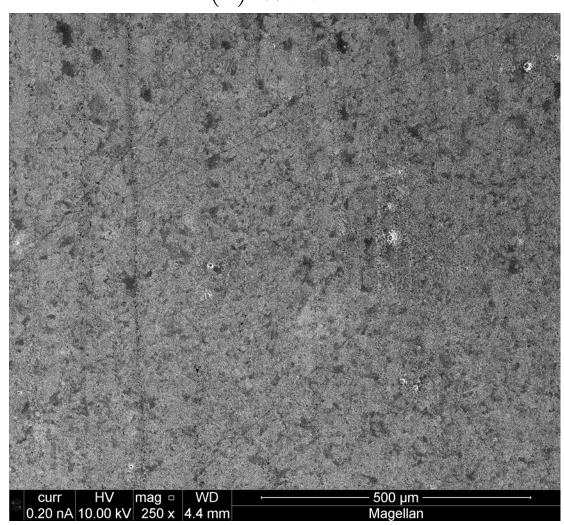

(d) Weld 16

Figure 6.6. SEM images of the transition from base material to the HAZ in etched specimens.

6.3 TMAZ Region

The same optical and scanning electron microscopes were used to capture microscopic images at a higher magnification in the TMAZ just past the transition region (Figs. 6.7 and 6.8). Images of the non-welded material at this resolution are shown in Figures 6.7a and 6.8a, remembering that the plane imaged is perpendicular to the rolling direction of the processed material. The grain size of the TMAZ is around 10 μm or smaller, compared to the non welded material, where grain size ranges from 5 to 50 μm. This reduction in grain size is due to a phenomenon called dynamic recrystallization. Just as in previous images, the resolution in these figures is not fine enough to resolve the pearlite into its alternating α ferrite and cementite lamellae.

6.4 Weld Zone

In dynamic recrystallization (DRX), grain growth and nucleation occurs during the deformation of the material, whereas in traditional heat treatment, recrystallization happens after the part has undergone deformation, in an additional heat treating step. In low carbon steels, DRX has been shown to occur at temperatures above the A_3 temperature (910°C) due to large strains [15, 16]. In the experimental trials, the temperature of the steel during LFW was measured as high as 1000°C near the surface, hot enough for the deforming material to undergo dynamic recrystallization. However, the time that the weld interface remained above the A_3 temperature was on the order of seconds or less depending on the weld parameters.

During DRX, smaller austenitic grains nucleate, and some transform into fine ferrite grains below the A_3 temperature after the oscillations have ceased and the joint begins to cool. As the temperature further falls to below the eutectoid temperature (727°C), the remaining austenite transforms to pearlite, undoing much of the DRX that occurred above the A_3 temperature. At a fine enough resolution, a grain size

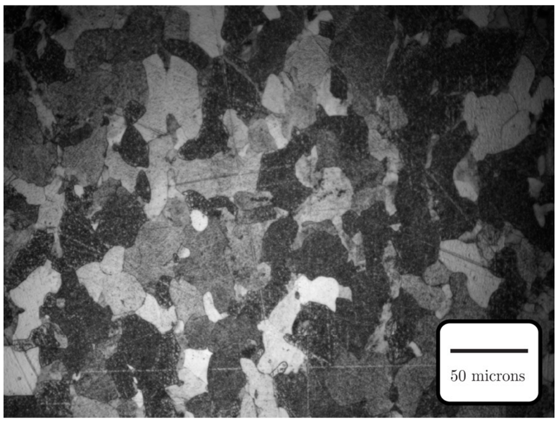

(a) Non-welded material

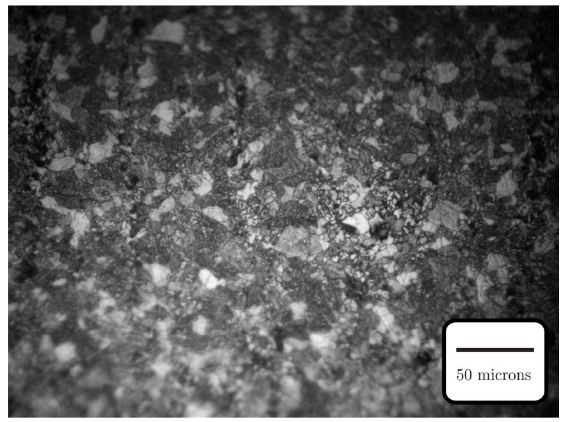

(b) Weld 14

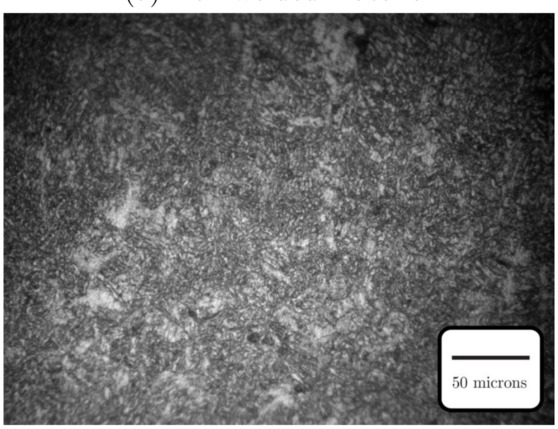

(c) Weld 15

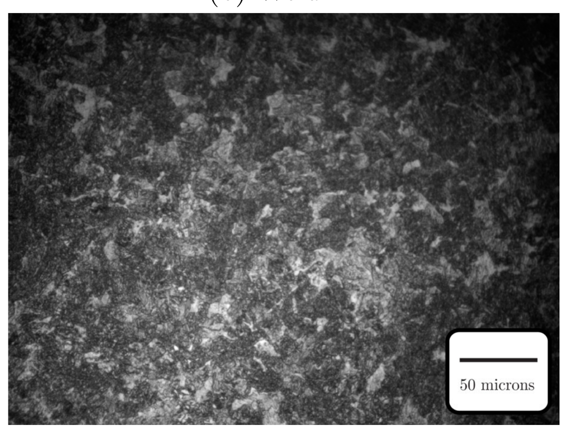

(d) Weld 16

Figure 6.7. Optical micrographs of the etched specimens in the region just after the transition from base material to the TMAZ

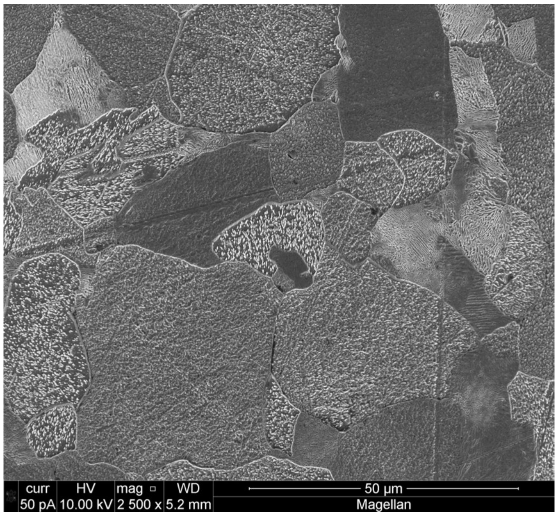

(a) Non-welded material

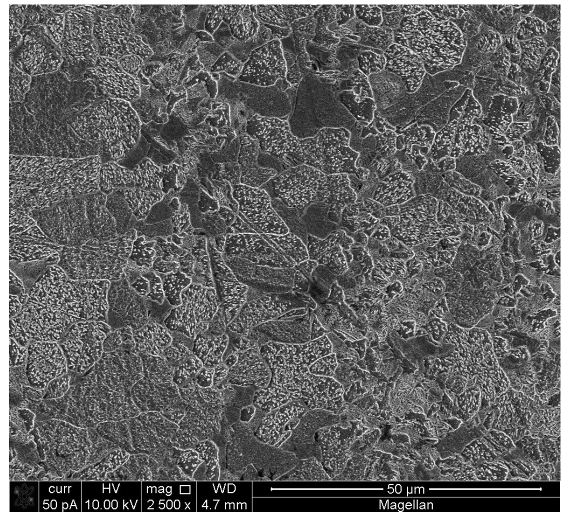

(b) Weld 14

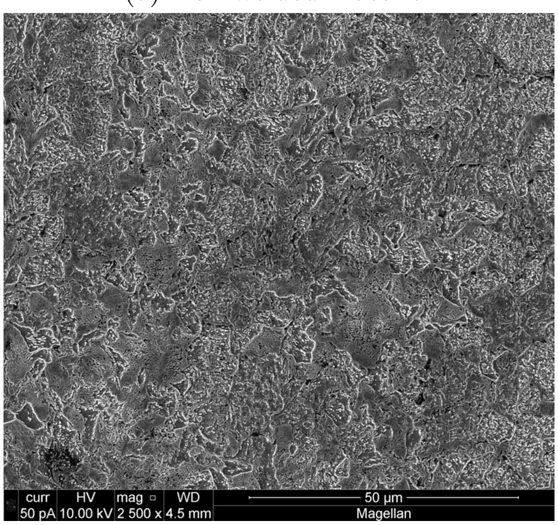

(c) Weld 15

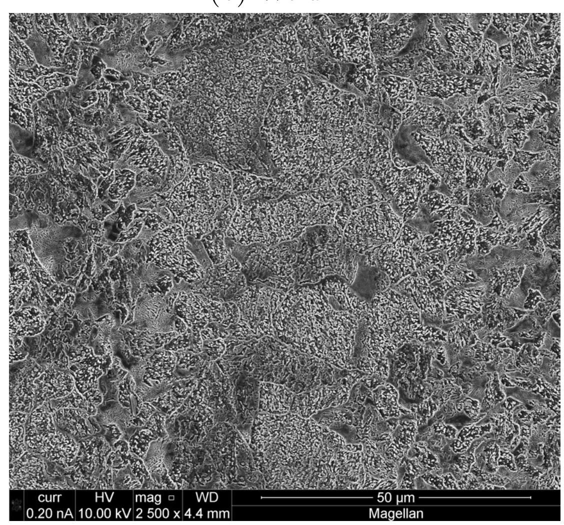

(d) Weld 16

Figure 6.8. SEM images of the etched specimens in the region just after the transition from base material to the HAZ

reduction and small increase in the amount of ferrite would be expected. At the magnification in Figure 6.7a, it is difficult to measure the reduction, but the grain size has visually decreased. The same 400x magnification was used to capture images in the weld zone (Fig. 6.9), visually determined by the relatively smallest grain size across the weld line. Unfortunately the resolution in these figures is not fine enough to resolve the pearlite either. Future work should use a higher magnification with an SEM machine in order to resolve the pearlite.

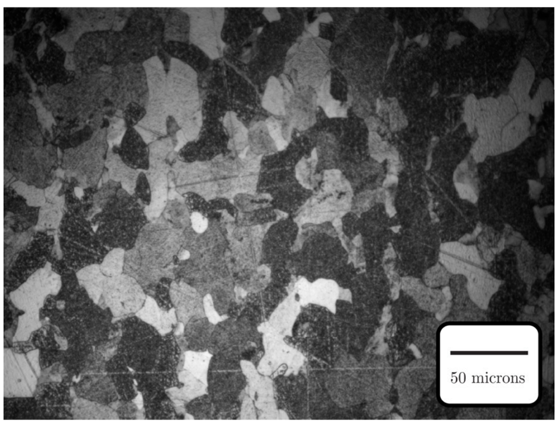

(a) Non-welded material

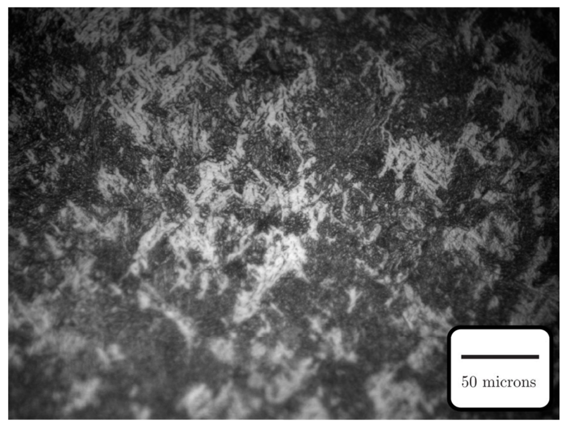

(b) Weld 14

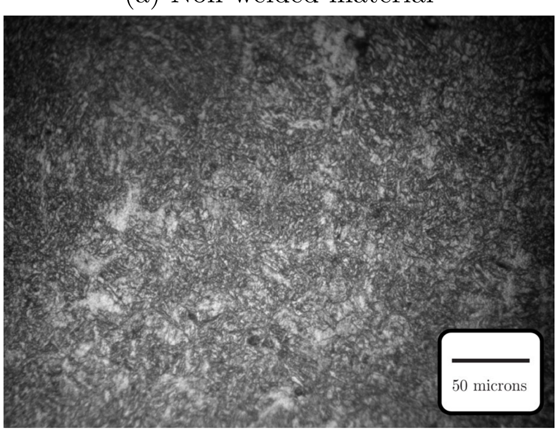

(c) Weld 15

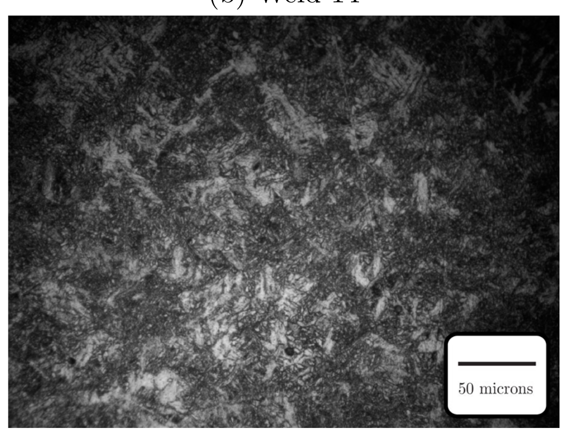

(d) Weld 16

Figure 6.9. Optical micrographs of the etched specimens in the center of the HAZ.

CHAPTER 7

CONCLUSIONS AND FUTURE WORK

The primary goal of this thesis was to demonstrate preheating as a viable option, in order to establish a cost-cutting strategy for the production of LFW equipment that makes it practical for a wider variety of applications. The first action taken to achieve this goal was to perform an unreplicated, two-level factorial DOE (Table 2.1) to study the effect of four process parameters (average rubbing velocity, weld pressure, upset distance, and preheat temperature) on three response variables (weld strength, HAZ width . peak hardness, and energy usage) for the IH and LFW of AISI 1020 steel. The second action taken to achieve this goal was to develop an IH and LFW numerical model in DEFORM to predict both the experimental temperature growth and upset measurements; this way future parametric studies can utilize a numerical model instead of costly experiments. The final action taken to achieve this goal was to characterize the microstructure within the IH and LFW joints via microscopic and scanning electron microscopic imaging.

Based on the experimental results, it can be concluded for AISI 1020 steel in the parameter ranges tested that the yield strength in flexure is insensitive to changes in pressure, velocity, upset, and preheat temperature. Furthermore, pressure, velocity, upset, and preheat temperature do not significantly affect the HAZ width and peak hardness across the weld zone, but do increase the hardness inside of the HAZ for all of the welds. This was confirmed visually via a microstructural investigation: DRX can be seen in both microscopic and scanning electron microscopic imaging, evidenced by a grain size reduction and a small increase in the amount of ferrite in the TMAZ and weld zone. Additionally, in-situ measurements of energy during welding showed that increasing weld pressure, decreasing rubbing velocity, and decreasing upset distance will decrease the energy used during the LFW phase of IH and LFW. Lastly, it was shown that preheat temperature has no effect on energy used during the LFW phase of IH and LFW, but has a positive effect on energy used during the combined phases of IH and LFW.

Based on the modeling results, it has been shown that IH can be numerically modeled by approximating a 1-turn induction coil in 2D space by revolving a rectangular coil around a large radius, and scaling the IH parameters accordingly. It has also been shown that a friction user subroutine can be used to predict the average friction factor for the frictional boundary condition between two workpieces in dry, sliding contact. This user subroutine accounts for asperity flattening and fractional area of contact growth for two LFW workpieces in contact. It became evident after years of testing that the technology in DEFORM is not yet able to resolve frictional contact between two separate and deformable workpieces oscillating at high frequencies and under high pressures. However, the friction user subroutines were still developed and proven to be functional in simple test cases, and will hopefully interface with a future release of DEFORM, or another software, to use in an LFW model. An alternative path forward for thermally modeling the initial phase of LFW was proposed and tested.

After FEA software packages in the future resolve the issue of contact loss the workpiece surfaces in oscillating, sliding friction, future LFW modeling research groups should utilize the friction user subroutines in Appendix A to simulate the initial phase of LFW with greater accuracy. Until that time, future studies should focus on developing develop better methods of accounting for the frictional boundary condition during the initial phase of LFW using a purely thermal model. The accuracy of the flash morphology and upset rate requires this phase to be modeled separately from the latter phases of LFW in which the two workpieces are in 100% contact, and can be modeled as a single deformable workpiece with a forging die on one end, and an oscillating die on the other.

Although the preheating technology may not have been optimal for the material and geometry of this experiment, the basic theory of preheat prior to LFW should continue to be developed. This development should focus on generating a more uniform and concentrated preheat zone on the weld surfaces of the workpieces, as well as focus on reducing the energy costs associated with the preheating step.

At this stage of development, the energy costs of a linear friction weld with IH are significantly higher than that of a traditional linear friction weld. This leads to questions about how beneficial preheat is since it has no effect on weld strength or HAZ width, and increases energy use. However, these conclusions lead to the main finding that preheating may enable welding at lower average rubbing velocities than previously considered possible in traditional LFW. If rubbing velocities are reduced, stored energy, and machine size and cost can also be reduced. This confirms the hypothesis, and the rationale for IH and LFW experiments as described in this thesis. Future studies should explore lower average surface velocities, higher weld pressures, and wider differences in preheat temperature, and examine the potential cost savings on capital equipment that can result. A lower machine cost would make the technology accessible to applications that require a lower capital investment on machinery, as well as generate a competitive alternative to traditional joining techniques.

APPENDIX A

Below is one of the two user routines written to calculate friction factor. This user routine is titled USR_BCC.

```
C==========================================================================
      SUBROUTINE USRBCC(VARIABLE,NODE1,NODE2,IELEM,NBCD,NDIE,RZ,
     &         DRZ,USRNOD,NUSRN,ENVTEM,TEMO,TEMC,CURTIM,MODEL,IMODE,ITYPE,
     &         NURZ)
C==========================================================================
C
C       User defined boundary value
C
C==========================================================================
      IMPLICIT REAL*8 (A-H,O-Z), INTEGER*4 (I-N)
c         COMMON /ZSTRCH/ STRCH      ! moved STRCH to common block UFHCOM2
      COMMON /UFHCOM2/ STRCH,EFSTS,EFEPS
      COMMON/MSNODE/MSNODE1,MSNODE2
      DIMENSION NBCD(NURZ,2),RZ(2,2),DRZ(NURZ,2),USRNOD(NUSRN,1),
     &         TEMO(2),TEMC(2)
      GO TO (10,20), MODEL
C
 10   CALL UBCC1(VARIABLE,NODE1,NODE2,IELEM,NBCD,NDIE,RZ,
     &         DRZ,USRNOD,NUSRN,ENVTEM,TEMO,TEMC,CURTIM,IMODE,ITYPE,NURZ)
      RETURN
C
 20   CALL UBCC2(VARIABLE,NODE1,NODE2,IELEM,NBCD,NDIE,RZ,
     &         DRZ,USRNOD,NUSRN,ENVTEM,TEMO,TEMC,CURTIM,IMODE,ITYPE,NURZ)
      RETURN
```

```
C
C  TO BE CONTINUED BY THE USER,  IF  NECESSARY
C
      END

C========================================================================
      SUBROUTINE UBCC1(VARIABLE,NODE1,NODE2,IELEM,NBCD,NDIE,RZ,
     &         DRZ,USRNOD,NUSRN,ENVTEM,TEMO,TEMC,CURTIM,IMODE,ITYPE,NURZ)
C========================================================================
C
C       User defined boundary condition
C
C========================================================================
      IMPLICIT REAL*8  (A-H,O-Z),  INTEGER*4  (I-N)
C
C       TMPENV: Interpolated Master Temperature
C       TMPSLF: Interpolated Slave Temperature
C       SLDVEL: Sliding Velocity
C       STRCH : Surface stretch on slave side
C       PRESSN: Pressure
C       EFSTS : Effective stress
C       EFEPS : Effective strain rate (not available)
C
      COMMON /UFHCOM/  TMPENV,TMPSLF,SLDVEL,PRESS
      COMMON /UFHCOM2/  STRCH,EFSTS,EFEPS
      COMMON/MSNODE/MSNODE1,MSNODE2
C
      DIMENSION NBCD(NURZ,2),RZ(2,2),DRZ(NURZ,2),USRNOD(NUSRN,1),
     &        TEMO(2),TEMC(2)
      DIMENSION USRND1(100),USRND2(100)
                 CHARACTER*80  IUSRVL
      COMMON /IUSR/  IUSRVL(10)
```

```
C
C      TO READ DATA (10 RESERVED LINES)
C         READ(IUSRVL(LINE NUMBER),*) DATA1,DATA2,DATA3...
C
C      TO WRITE DATA (10 RESERVED LINES)
C         WRITE(IUSRVL(LINE NUMBER),*) NEWDATA1, NEWDATA2, NEWDATA3 ...
C **************
C      VARIABLES FOR NOTRE DAME TRIBOLOGY MODEL
C      A0 : Initial contact area fraction
C      MA : Asperity friction factor
C      MO : Oxide friction factor
C      Theta : Asperity slope
       REAL*8 MA, MO, NODE1A, NODE2A
       IF(KOBJ.GT.1) RETURN
       VARIABLE=0.0


C
C      copy user variables
C
       DO I=1,NUSRN
          USRND1(I)=USRNOD(I,NODE1)
          USRND2(I)=USRNOD(I,NODE2)
       ENDDO
C
C      define pressure value
C
C      IMODE=1, ITYPE=1
C

       IF(IMODE.EQ.1) THEN
          IF(ITYPE.EQ.1) THEN
C
```

```
C         Assuming Pressure is a function of time
C
            PRESSURE=1.0*CURTIM
            VARIABLE=PRESSURE
         ENDIF
C
C         USER DEFINED FRCITION FACTOR
C   *************    Modifying Friction for Notre Dame **********
C   **** This routine is called for every *Iteration*.   Need to update
C   **** area as a user variable after every *converged step*
C
         IF (ITYPE.EQ.2) THEN
C
              READ(IUSRVL(1),*) A0
              READ(IUSRVL(2),*) MA
              READ(IUSRVL(3),*) MO
              READ(IUSRVL(4),*) THETA
              USRNOD(2,NODE1) = EFSTS
              USRNOD(2,NODE2) = EFSTS
              NODE1A = USRNOD(1,NODE1)
              NODE2A = USRNOD(1,NODE2)
              IF (NODE1A .LT. A0) THEN
                NODE1A = A0
              ENDIF
              IF (NODE2A .LT. A0) THEN
                 NODE2A = A0
              ENDIF
              A = 0.5*(NODE1A + NODE2A)
              WRITE(6,*) "Rel A = ", A
              VARIABLE = MA*A + MO*(1-A)
              WRITE(6,*) "M = ", VARIABLE
         ENDIF
```

```
      ENDIF

C     define heat flux value
      IF(IMODE.EQ.2) THEN
         IF(ITYPE.EQ.4) THEN

            HFLUX=1.0*CURTIM
            VARIABLE=HFLUX
         ENDIF
      ENDIF
      RETURN
      END
```

This user routine below, entitled USR_MSH, was utilized in parallel with USR_BCC in the calculation of the friction factor.

```
C**********************************************************
C
      SUBROUTINE USRMSH(RZ,DRZ,URZ,TEMP,DTMP,
     +     FRZA,FRZB,EFSTS,EFEPS,TEPS,
     +     RDTY,STS,EPS,DCRP,TSRS,DAMG,USRVE,USRVN,ATOM,HEATND,EPRE,
     +     VOLT,WEAR,
     +     HDNS,VF,DVF,VFN,TICF,GRAIN,
     +     CURTIM,DTMAXC,
     +     NBCD,NBCDT,NOD,MATR,NBDRY,KOBJ,NUMEL,NUMNP,
     +     NDSTART,NDEND,NEDGE,NUSRVE,NUSRND,NTMATR,
     +     ISTATUS,NROUTINE,NTRELN,NGRNVAL,KSTEP,AVGSRT,SRTLMT,AXMT,
     &     IELMNOD,EFEPS_NP,TEPS_NP,DAMG_NP,STS_NP)
C
C**********************************************************
C
C      All FIELD VARIABLES CAN BE CHANGED!
C
C      IMPROPER CHANGE MADE IN THIS ROUTINE WILL CAUSE PROBLEMS
```

```
C         IN THE ANALYSIS.
C
C         PLEASE USE THIS ROUTINE WITH CAUTION!!
C
C*******************************************************
C
C       This routine will be called at the beginning of the step and
C             at the end of the step
C
C       Object with FEM mesh will be passed to this Routine
C
      IMPLICIT REAL*8 (A-H,K,O-Z), INTEGER*4 (I,J, L-N)
c      IMPLICIT REAL*8 (A-H,O-Z), INTEGER*4 (I-N)

      COMMON /PLDSRK/ PDIE_SRK(2),PDIE_LD(2),PDIE_VEL(2)
C     PDIE_SRK(1:3): x- and y- Strokes of P_DIE
C     PDIE_LD(1:3): x- and y- Forces of P_DIE
C     PDIE_VEL(1:3): x- and y- velocity of P_DIE
      COMMON /IDIMEN/ NUMSTN,NUMSTS
C     NUMSTS : TOTAL NUMBER OF STRESS COMPONENTS PER ELEMENT
C      Torsional Element : NUMSTS=6, otherwise NUMSTS=4
C     NUMSTN : TOTAL NUMBER OF STRAIN COMPONENTS PER ELEMENT
C     Elastic,Plastic, and Thermal strains are selected for
C     strain output
C     NUMSTN = NUMSTS + NUMSTS + 1 = 9    =>  TSRS(9,*)
C
       COMMON /INDCTUSR/ RINHUSR(200),INHUSRFLAG
C     INHUSRFLAG : 0=coil input defined in DB, default
C                  1=current density, 2=power, 3=voltage drop
C     RINHUSR(KOBJ) : input value for induction heating
C
       DIMENSION RZ(2,*),DRZ(2,*),URZ(2,*),TEMP(*),DTMP(*)
```

```
      DIMENSION FRZA(2,*),FRZB(2,*)
      DIMENSION EFSTS(*),EFEPS(*),TEPS(*)
      DIMENSION STS(NUMSTS,*),TSRS(NUMSTN,*)
      DIMENSION EPS(NUMSTS,*),DCRP(NUMSTS,*)
      DIMENSION DAMG(*),ATOM(*),HDNS(2,*)
      DIMENSION NOD(4,*)
      DIMENSION RDTY(*),VOLT(*)
      DIMENSION USRVN(NUSRND,*)
      DIMENSION USRVE(NUSRVE,*)
      DIMENSION EPRE(*),HEATND(*)
      DIMENSION NBDRY(*),MATR(*)
      DIMENSION WEAR(5,*)
C
      DIMENSION NBCD(2,*),NBCDT(*)
C
      DIMENSION VF(NTMATR,*),VFN(NTMATR,*)
      DIMENSION DVF(NTRELN,*),TICF(NTRELN,*)
      DIMENSION AXMT(*),GRAIN(NGRNVAL,*)
      DIMENSION IELMNOD(*)
      DIMENSION EFEPS_NP(*),TEPS_NP(*),DAMG_NP(*),STS_NP(4,*)
      DIMENSION IN(4)
      DATA IN/1,3,4,2/
          DIMENSION NDINELEM(10,30000)
          DIMENSION NELPN(30000)
          DIMENSION UNSTRESS(30000),UNSTRATE(30000),PRZ(30000)
          DIMENSION VNORM1(2), VNORM2(2), VNORMN(2)

C     Create a flag called "first" and initialize it to 0 so we
C     can track the first time a subroutine is called.
          COMMON /FIRST/ IFIRST
          DATA IFIRST/0/
          CHARACTER*80 IUSRVL
```

```
      COMMON /IUSR/ IUSRVL(10)
C
C     TO READ DATA (10 RESERVED LINES)
C     READ(IUSRVL(LINE NUMBER),*) DATA1,DATA2,DATA3...
C
C     TO WRITE DATA (10 RESERVED LINES)
C     WRITE(IUSRVL(LINE NUMBER),*) NEWDATA1, NEWDATA2, NEWDATA3 ...
C
C     VARIABLES FOR NOTRE DAME TRIBOLOGY MODEL
C     A0 : Initial contact area fraction
C     MA : Asperity friction factor
C     MO : Oxide friction factor
C     Theta : Asperity slope
      REAL*8 MA, MO, NODE1A, NODE2A
      IF(KOBJ.GT.1) RETURN
        READ(IUSRVL(1),*) A0
        READ(IUSRVL(2),*) MA
        READ(IUSRVL(3),*) MO
        READ(IUSRVL(4),*) THETA
        WRITE(6,*) "A0 = ",A0," MA = ",MA," M0 = ",MO," THETA = ",THETA
C
       IF (ISTATUS.EQ.0) RETURN
C     IF (NROUTINE.EQ.0) RETURN
C     Identify all of the elements associated with a given node.
C     Keep a count of the elements with a given node in NELPN
C     IFIRST -- run this node per element search only once when the
C     program is started.  It is computationally expensive.
C     WRITE(6,*) "IN USR_MSH"
       IF (IFIRST .EQ. 0) THEN
          IFIRST = 1
      DO 110 NODE = NDSTART,NDEND
c        WRITE(6,*)"Loop 110, NODE = ",NODE
```

```
              NELPN(NODE) = 0
c             WRITE(6,*) "NELPN = ",NELPN(NODE)
              DO 120 IELEM = 1,NUMEL
c             WRITE(6,*) "Loop 120, IELEM = ",IELEM
                    DO 130 N = 1,4
c             WRITE(6,*) "NOD(", N,",", IELEM, ") = ", NOD(N,IELEM)
                      IF (NOD(N,IELEM) .EQ. NODE) THEN
                          NELPN(NODE) = NELPN(NODE)+1
c         WRITE(6,*) "NELPN = ",NELPN(NODE)
                          NDINELEM(NELPN(NODE),NODE) = IELEM
c             WRITE(6,*) "NDINELEM = ",NDINELEM(NELPN,NODE)
                        ENDIF
130                 CONTINUE
120           CONTINUE
110       CONTINUE
          ENDIF
C         End of the "run once at start of program" block

          WRITE(6,*) "BEGIN USR_MSH"
          DO 200 NODE = NDSTART,NDEND
               WRITE(6,*)"ASSIGNING NODE ",NODE
               UNSTRESS(NODE) = 0.0
                   UNSTRATE(NODE) = 0.0
               DO 205 IELEM = 1,NELPN(NODE)
                     UNSTRESS(NODE) = UNSTRESS(NODE) + EFSTS(IELEM)
                     UNSTRATE(NODE) = UNSTRATE(NODE) + EFEPS(IELEM)
 205          CONTINUE
               UNSTRESS(NODE) = UNSTRESS(NODE)/NELPN(NODE)
                   WRITE(6,*)"UNSTRESS",NODE," = ",UNSTRESS(NODE)
                   UNSTRATE(NODE) = UNSTRATE(NODE)/NELPN(NODE)
                   WRITE(6,*)"UNSTRATE",NODE," = ",UNSTRATE(NODE)
 200      CONTINUE
```

```
C        Notre Dame Relative Contact Area calculations
            DO 250 IEDGE = 2,NEDGE-1

C        calculate node area
                 NEDGND1 = NBDRY(IEDGE-1)
                 NEDGND2 = NBDRY(IEDGE)
                 X1 = RZ(1,NEDGND1)
                 Y1 = RZ(2,NEDGND1)
                 X2 = RZ(1,NEDGND2)
                 Y2 = RZ(2,NEDGND2)
                 DX = X2 - X1
                 DY = Y2 - Y1
                 AREA1 = SQRT(DX**2 + DY**2)

C        normal of face before node IEDGE

                 VNORM1(1) = -DY/AREA1
                 VNORM1(2) = DX/AREA1
                 NEDGND1 = NBDRY(IEDGE)
                 NEDGND2 = NBDRY(IEDGE+1)
                 X1 = RZ(1,NEDGND1)
                 Y1 = RZ(2,NEDGND1)
                 X2 = RZ(1,NEDGND2)
                 Y2 = RZ(2,NEDGND2)
                 DX = X2 - X1
                 DY = Y2 - Y1
                 AREA2 = SQRT(DX**2 + DY**2)

C        normal of face after IEDGE
                 VNORM2(1) = -DY/AREA2
                 VNORM2(2) = DX/AREA2
```

```
C       average of the two normals
          VNORMN(1) = VNORM1(1) + VNORM2(1)
                VNORMN(2) = VNORM1(2) + VNORM2(2)
                VLEN = SQRT(VNORMN(1)**2 + VNORMN(2)**2)
                VNORMN(1) = VNORMN(1)/VLEN
                VNORMN(2) = VNORMN(2)/VLEN

C       magnitude of force is dot product of "average" normal
C       and force vector. store temporarily in PRZ
          FRZN = VNORMN(1)*FRZB(1,NEDGND1) + VNORMN(2)*FRZB(2,NEDGND2)
          AREA = 0.5*(AREA1 + AREA2)
          PRZ(NEDGND1) = FRZN/AREA
                USRVN(2,NEDGND1) = PRZ(NEDGND1)
          WRITE(6,*)
 250    CONTINUE

C       Repeat calculation for the start/end boundary node
          IEDGE = NEDGE
                NEDGND1 = NBDRY(IEDGE-1)
                NEDGND2 = NBDRY(IEDGE)
                X1 = RZ(1,NEDGND1)
                Y1 = RZ(2,NEDGND1)
                X2 = RZ(1,NEDGND2)
                Y2 = RZ(2,NEDGND2)
                DX = X2 - X1
                DY = Y2 - Y1
                AREA1 = SQRT(DX**2 + DY**2)

C       unit normal of face before node IEDGE
                VNORM1(1) = -DY/AREA1
                VNORM1(2) = DX/AREA1
```

```
            NEDGND1 = NBDRY(1)
            NEDGND2 = NBDRY(2)
            X1 = RZ(1,NEDGND1)
            Y1 = RZ(2,NEDGND1)
            X2 = RZ(1,NEDGND2)
            Y2 = RZ(2,NEDGND2)
            DX = X2 - X1
            DY = Y2 - Y1
            AREA2 = SQRT(DX**2 + DY**2)

C     unit normal of face after IEDGE
            VNORM2(1) = -DY/AREA2
            VNORM2(2) = DX/AREA2

C     average of the two unit normals
        VNORMN(1) = VNORM1(1) + VNORM2(1)
            VNORMN(2) = VNORM1(2) + VNORM2(2)
            VLEN = SQRT(VNORMN(1)**2 + VNORMN(2)**2)
            VNORMN(1) = VNORMN(1)/VLEN
            VNORMN(2) = VNORMN(2)/VLEN

C     magnitude of force is dot product of "average" normal
C     and force vector, store temporarily in PRZ
        FRZN = VNORMN(1)*FRZB(1,NEDGND1) + VNORMN(2)*FRZB(2,NEDGND2)
        AREA = 0.5*(AREA1 + AREA2)
        PRZ(NEDGND1) = FRZN/AREA
          DO 300 NODE = NDSTART,NDEND
            A = USRVN(1,NODE)
            IF (A .LT. A0) A = A0
              k = 0.577*UNSTRESS(NODE)
            IF (k .EQ. 0) k= 0.577
            Prel = ABS(PRZ(NODE)/k)
```

```fortran
         dE = UNSTRATE(NODE)*DTMAXC
           USRVN(4,NODE) = dE
         F1 = 0.515 + 0.345*A - 0.86*A**2
         F2 = 1.0/(2.571 - A - A*LOG(1-A))
         dA = (1.0/THETA)*dE*(Prel*F1)/(2*A - Prel*F2)
         IF (dA .LT. 0.0) THEN
           dA = 0.0
         ENDIF
         IF (Prel .GT. 0.05) THEN
           WRITE(6,*) " k = ",k
           WRITE(6,*) " Prel = ",Prel
           WRITE(6,*)"A = ",A
           WRITE(6,*) "F2 = ",F2
         ENDIF
         USRVN(1,NODE) = A + dA
         USRVN(3,NODE) = .9*(A+dA)+.4*(1-(A+dA))
         WRITE(6,*)"Fractional Contact Area(",NODE,") = ",
         USRVN(1,NODE)
         WRITE(6,*)"Friction Factor(",NODE,") = ",USRVN(3,NODE)
300   CONTINUE
      RETURN
      END
```

REFERENCES

1. Induction heating work coils. URL https://www.ambrell.com/hubfs/Ambrell_PDFs/411-0168-10.pdf.

2. Scientific Forming Technologies Corporation deform-3d product brochure. http://www.deform.com/wp-content/uploads/2015/06/DEFORM-3D.pdf. Accessed: 2015-07-09.

3. S. Aithal and H. J. Ravindra. *Textbook of Engineering Physics*. Acme Learning Pvt. Limited, Jan 2017.

4. T. W. Anderson and D. A. Darling. *Journal of the American statistical association*, 49(268):765–769, 1954.

5. ANSI/AWS C6.1-89 (R2009). Recommended practices for friction welding. standard, American Welding Society, 550 N.W. LeJeune Road, Miami, FL 33126, 2009.

6. M. Aritoshi and K. Okita. *Welding international*, 17(4):271–275, 2003.

7. M. Avinash, G. Chaitanya, D. K. Giri, S. Upadhya, and B. Muralidhara. Microstructure and mechanical behaviuor of rotary friction welded titanium alloys. In *Proceedings of world academy of science, engineering and technology*, volume 26, pages 426–428, 2007.

8. I. Bhamji, M. Preuss, P. L. Threadgill, and A. Addison. *Materials Science and Technology*, 27(1):2–12, 2011.

9. G. E. Box and D. R. Cox. *Journal of the Royal Statistical Society. Series B (Methodological)*, pages 211–252, 1964.

10. G. Buffa, M. Cammalleri, D. Campanella, and L. Fratini. *Materials & Design*, 82:238–246, 2015.

11. J. Byerlee. *Pure and applied geophysics*, 116(4-5):615–626, 1978.

12. H. S. Carslaw and J. C. Jaeger. *Conduction of Heat in Solids*. Ocford University Press, 2 edition, 1959.

13. E. Ceretti, L. Fratini, C. Giardini, and D. La Spisa. *International Journal of Material Forming*, 3(1):1015–1018, 2010.

14. J. Davies. *Conduction and induction heating*. Number 11. IET, 1990.

15. L.-x. Du, Z.-p. Zhang, G.-f. She, X.-h. Liu, and G.-d. Wang. *Journal of Iron and Steel Research, International*, 13(3):31–50, 2006.

16. B. Eghbali, A. Abdollah-Zadeh, H. Beladi, and P. Hodgson. *Materials Science and Engineering: A*, 435:499–503, 2006.

17. L. Fratini and D. La Spisa. Numerical simulation of linear fiction welding (lfw) processes. In *The 14th International ESAFORM Conference on Material Forming: ESAFORM 2011*, volume 1353, pages 1284–1289. AIP Publishing, 2011.

18. L. Fratini, G. Buffa, D. Campanella, and D. La Spisa. *Materials & Design*, 40: 285–291, 2012.

19. L. Fu, L. Duan, and S. Du. *Welding Journal - New York*, 82(3):65–S, 2003.

20. A. Fuji, Y. Horiuchi, and K. Yamamoto. *Science and technology of welding and Joining*, 10(3):287–294, 2005.

21. S. Fukumoto, T. Inoue, S. Mizuno, K. Okita, T. Tomita, and A. Yamamoto. *Science and Technology of Welding and Joining*, 15(2):124–130, 2010.

22. J. Greenwood and J. Williamson. *The Royal Society*, 295(1442):300–319, 1966.

23. J. Greenwood and J. P. Williamson. *Proc. R. Soc. Lond. A*, 295(1442):300–319, 1966.

24. M. Grujicic, G. Arakere, B. Pandurangan, C.-F. Yen, and B. Cheeseman. *Journal of materials engineering and performance*, 21(10):2011–2023, 2012.

25. M. Grujicic, R. Yavari, J. Snipes, S. Ramaswami, C.-F. Yen, and B. Cheeseman. *Journal of Materials Engineering and Performance*, 23(6):2182–2198, 2014.

26. J. Isaacs. Induction heating–theory, design, application, January 1968. URL `http://search.proquest.com/docview/1647742023/`.

27. T. A. Jankowski, N. H. Pawley, L. M. Gonzales, C. A. Ross, and J. D. Jurney. *Applied Mathematical Modelling*, 40(4):2770 – 2782, 2016. ISSN 0307-904X. doi: https://doi.org/10.1016/j.apm.2015.10.006. URL `http://www.sciencedirect.com/science/article/pii/S0307904X15006393`.

28. S. Kalpakjian and S. R. Schmid. *Manufacturing Processes for Engineering Materials*. Pearson, 2008.

29. S. Kalpakjian and S. R. Schmid. *Manufacturing engineering and technology*. Pearson Upper Saddle River, NJ, USA, 2014.

30. S. Kiselyeva, A. Yamileva, M. Karavaeva, I. S. Nasibullayev, V. Bychkov, . Y. Medvedev, V. Supov, F. Musin, I. Alexandrov, and V. Latysh. *Journal of Engineering Science and Technology Review*, 5(3):44–47, 2012.

31. G. Krauss. *ASM International, 1990,*, page 497, 1990.

32. L. A. Lee, A. McAndrew, C. Buhr, K. Beamish, and P. A. Colegrove. 2015.

33. W. B. Lee, Y. Yeon, D. Kim, and S. Jung. *Materials science and technology*, 19 (6):773–778, 2003.

34. R. V. Lenth. *Technometrics*, 31(4):469–473, 1989.

35. W. Li, S. Shi, F. Wang, Z. Zhang, T. Ma, and J. Li. *Journal of Engineering Science and Technology Review*, 5(3):10–19, 2012.

36. W. Li, S. Shi, F. Wang, T. Ma, J. Li, D. Gao, and A. Vairis. *International Journal of Thermal Sciences*, 67:192–199, 2013.

37. W. Li, J. Suo, T. Ma, Y. Feng, and K. Kim. *Materials Science and Engineering: A*, 599:38–45, 2014.

38. W. Li, F. Wang, S. Shi, and T. Ma. *Journal of materials engineering and performance*, 23(2):384–390, 2014.

39. W. Li, F. Wang, S. Shi, T. Ma, J. Li, and A. Vairis. *Journal of Materials Engineering and Performance*, 23(11):4010–4018, 2014.

40. W.-Y. Li, T. Ma, and J. Li. *Materials & Design*, 31(3):1497–1507, 2010.

41. Z. M. Liu, Z. H. Guo, G. Y. Zhao, S. Zhang, and J. L. Pan. 3d numerical simulation of linear friction welding of 45# carbon steel. In *Advanced Materials Research*, volume 476, pages 701–704. Trans Tech Publ, 2012.

42. M. Maalekian. *Science and Technology of Welding and Joining*, 12(8):738–759, 2007.

43. M. Maalekian, E. Kozeschnik, H. Brantner, and H. Cerjak. *Acta Materialia*, 56 (12):2843–2855, 2008.

44. M. Mahoney, C. Rhodes, J. Flintoff, W. Bingel, and R. Spurling. *Metallurgical and materials transactions A*, 29(7):1955–1964, 1998.

45. A. R. McAndrew, P. A. Colegrove, A. C. Addison, B. C. Flipo, and M. J. Russell. *Metallurgical and Materials Transactions A*, 45(13):6118–6128, 2014.

46. A. R. McAndrew, P. A. Colegrove, A. C. Addison, B. C. Flipo, and M. J. Russell. *Materials & Design*, 66:183–195, 2015.

47. A. R. McAndrew, P. A. Colegrove, B. C. Flipo, and C. Bühr. *Science and Technology of Welding and Joining*, 22(6):496–504, 2017.

48. D. C. Montgomery. *Design and analysis of experiments*. John wiley & sons, 2017.

49. T. Nguyen and D. Weckman. *Metallurgical and Materials Transactions B*, 37(2): 275–292, 2006.

50. M. Nunn. Aero engine improvements through linear friction welding. In *Proceedings 1st Int. Conference on Innovation and Integration in Aerospace Sciences*, 2005.

51. N. Oiwa, R. Sakamoto, Y. Otake, M. Tsunori, K. Nakamura, and H. Kawashima. Friction joining method and joined structure, Feb. 10 2015. US Patent 8,950,651.

52. E. Orowan. *Proceedings of the Institution of Mechanical Engineers*, 150(1):140–167, 1943.

53. B. Persson, O. Albohr, U. Tartaglino, A. Volokitin, and E. Tosatti. *Journal of Physics: Condensed Matter*, 17(1):R1, 2005.

54. G. A. Pinheiro, C. W. Olea, J. F. dos Santos, and K. U. Kainer. *Advanced Engineering Materials*, 9(9):757–763, 2007.

55. M. G. Reddy, S. A. Rao, and T. Mohandas. *Science and technology of welding and joining*, 13(7):619–628, 2008.

56. W. Richter. *Patent no. DE477084*, 1929.

57. V. Rudnev and V. Demidovich. Advanced computation software for everyday use in modern induction heat treating. In *ASM Heat Treating: Proceedings of the 17th conference*, pages 551–555, 2010.

58. M. Russell, M. M. E. Nunn, M. N. Edge, and M. A. Shilton. 2009.

59. P. K. Saha, W. R. Wilson, and R. S. Timsit. *Wear*, 197(1-2):123–129, 1996.

60. P. Sathiya, S. Aravindan, and A. N. Haq. *The International Journal of Advanced Manufacturing Technology*, 31(11-12):1076–1082, 2007.

61. P. Sathiya, S. Aravindan, and A. N. Haq. *Materials & Design*, 29(6):1099–1109, 2008.

62. F. Schröder, R. Ward, A. Walpole, R. Turner, M. Attallah, J.-C. Gebelin, and R. Reed. *Materials Science and Technology*, 31(3):372–384, 2015.

63. F. Schroeder, R. Ward, R. Turner, M. Attallah, J. Gebelin, R. Reed, and A. Walpole. Linear friction welding of titanium alloys for aeroengine applications: modelling and validation. In *Proceedings of the 9th International Trends in Welding Research Conference*, 2012.

64. *DEFORM v11.2 Documentation*. Scientific Forming Technologies Corporation, Columbus, OH, 2017.

65. M. C. Shaw, A. Ber, and P. A. Mamin. *Journal of Basic Engineering*, 82(2): 342–345, 1960.

66. J. Smith, W. Xiong, W. Yan, S. Lin, P. Cheng, O. L. Kafka, G. J. Wagner, J. Cao, and W. K. Liu. *Computational Mechanics*, 57(4):583–610, Apr 2016. ISSN 1432-0924.

67. X. Song, M. Xie, F. Hofmann, T. Jun, T. Connolley, C. Reinhard, R. Atwood, L. Connor, M. Drakopoulos, S. Harding, et al. *Materials & Design*, 50:360–369, 2013.

68. J. Sorina-Müller, M. Rettenmayr, D. Schneefeld, O. Roder, and W. Fried. *Computational Materials Science*, 48(4):749–758, 2010.

69. J. Tao, T. C. Zhang, P. T. Liu, J. Li, and Y. Mang. Numerical computation of a linear friction welding process. In *Materials Science Forum*, volume 575, pages 811–815. Trans Tech Publ, 2008.

70. R. Turner, J.-C. Gebelin, R. Ward, and R. Reed. *Acta Materialia*, 59(10):3792–3803, 2011.

71. R. Turner, R. Ward, R. March, and R. Reed. *Metallurgical and Materials Transactions B*, 43(1):186–197, 2012.

72. R. Turner, F. Schroeder, R. Ward, and J. Brooks. *Advances in Materials Science and Engineering*, 2014:238–246, 2014.

73. A. Vairis and M. Frost. *Materials Science and Engineering: A*, 292(1):8–17, 2000.

74. M. Vaziri, S. Berg, D. Sandberg, and I. T. Gheinani. *Wood Material Science & Engineering*, 9(2):102–109, 2014.

75. T. Wanheim and N. Bay. *CIRP Annals-Manufacturing Technology*, 27:189–194, 1978.

76. P. Wanjara and M. Jahazi. *Metallurgical and Materials Transactions A*, 36(8): 2149–2164, 2005.

77. P. Wanjara and M. Jahazi. *Metallurgical and Materials Transactions A*, 36(8): 2149–2164, 2005.

78. W. Wilson and S. Sheu. *International journal of mechanical sciences*, 30(7): 475–489, 1988.

79. W. R. D. Wilson. *International Journal of Mechanical Sciences*, 19(2):103–112, 1977.

80. I. Woo, M. Aritoshi, and Y. Kikuchi. *ISIJ international*, 42(4):401–406, 2002.

81. X. Y. Wu. Finite element simulation of linear friction welding. In *Advanced Materials Research*, volume 411, pages 126–129. Trans Tech Publ, 2012.

82. Y.-C. Yang, W.-L. Chen, and H.-L. Lee. *Numerical Heat Transfer, Part A: Applications*, 59(2):130–149, 2011.

83. P. Zhao, L. Fu, and D. Zhong. *Computational Materials Science*, 92:325–333, 2014.

This document was prepared & typeset with pdfLaTeX*, and formatted with* NDdiss2$_\varepsilon$ *classfile (v3.2013[2013/04/16]) provided by Sameer Vijay and updated by Megan Patnott.*